academic.oup.com/jmicro

Volume 68 | Supplement 1 | November 2019

ISSN 2050-5698 (PRINT)
ISSN 2050-5701 (ONLINE)

Scan to view this journal on your mobile device

MICROSCOPY

Previously Journal of Electron Microscopy

Future of Microscopy Imaging Using AI
~The 62nd Symposium of the Japanese Society of Microscopy~

Guest Editors:
Yoshihiro Akimoto
Toshiaki Tachibana
Katsumi Hagita
Yasuko Kaneko
Osamu Katsumata
Kazuhiro Kumagai
Tadahiro Nagasawa
Nobuhiko Ohno
Shigeo Okabe
Ryusuke Sagawa
Ryuichiro Tamochi
Hiroyuki Yamada

THE JAPANESE SOCIETY OF MICROSCOPY

OXFORD UNIVERSITY PRESS

MICROSCOPY
Previously Journal of Electron Microscopy **volume 68 • 2019 • number S1**

Editor-in-Chief

Shigeo Okabe
The University of Tokyo

Co-Editors-in-Chief

Kenji Tsuda
Tohoku University (Physical Sciences)

Toyoshi Fujimoto
Nagoya University (Biological Sciences)

Editorial Board

Satoshi Hata
Kyushu University

Kazutaka Mitsuishi
National Institute for Materials Science

Teruyasu Mizoguchi
The University of Tokyo

Yoshifumi Oshima
Japan Advanced Institute of Science and Technology

Koh Saitoh
Nagoya University

Hidetaka Sawada
JEOL Limited

Yasuhiro Sugawara
Osaka University

Jun Yamasaki
Osaka University

Norio Amizuka
Hokkaido University

Ichirou Karahara
University of Toyama

Toshiyuki Matsuzaki
Gunma University

Makoto Miyata
Osaka City University

Atsuo Miyazawa
University of Hyogo

Takuo Yasunaga
Kyushu Institute of Technology

Takeshi Noda
Kyoto University

Sen Takeda
University of Yamanashi

Gianluigi Botton
McMaster University (Canada)

Rafal Dunin-Borkowski
Ernst Ruska-Centre for Microscopy and Spectroscopy with Electrons (Germany)

Joanne Etheridge
Monash University (Australia)

Young-Woon Kim
Seoul National University (Korea)

Lian-Mao Peng
Peking University (China)

Yimei Zhu
Brookhaven National Laboratory (USA)

Yifan Cheng
University of California San Francisco (USA)

Takashi Ishikawa
Paul Scherrer Institute (Switzerland)

Kea Joo Lee
Korea Brain Research Institute (Korea)

Ryuichi Shigemoto
Institute of Science and Technology Austria (Austria)

Fei Sun
Chinese Academy of Sciences (China)

Thomas Walz
The Rockefeller University (USA)

Executive Adviser

Yoshio Bando
National Institute of Materials Science

Editorial Office

Microscopy, c/o Oxford Journals, Oxford University Press Tokyo, 4-17-5-3F Shiba, Minato-ku, Tokyo 108-8386, Japan
e-mail: microscopy.editorialoffice@oup.com *phone:* +81 3 5444 5858 *fax:* +81 3 3454 2929
Supported in part by the National Foundation

© 2019 All rights reserved. The Japanese Society of Microscopy.

Subscriptions

A subscription to *Microscopy* comprises six issues, with an annual author and subject index. Subscriptions are entered on a calendar year basis only. Prices include postage by surface mail or, for subscribers in the USA and Canada, by air freight or in India, Japan, Australia and New Zealand by Air Speeded Post. Airmail rates are available on request.

Annual subscription rate (Volume 68, 2019)

Corporate
Print and Online £743.00/$1479.00/€1112.00
Online Only £525.00/$1050.00/€787.00
Print Only £685.00/$1369.00/€1029.00
Institutional
Print and Online £593.00/$1184.00/€889.00
Online Only £403.00/$805.00/€606.00
Print Only £547.00/$1093.00/€821.00
*Members**
Print Only £171.00/$333.00/€250.00 (This includes free online access) *Members of Australian Society for Electron Microscopy/ British Microscopy Society/ Electron Microscopy and Analysis Group/ Royal Microscopical Society/ Scandinavian Society for Electron Microscopy/ Swiss Society for Optics and Electron Microscopy.
Please note: US$ rate applies to US and Canada, Euros applies to Europe, UK£ applies to UK and Rest of World.

Please add sales tax to the prices quoted.

The current year and two previous years' issues are available from Oxford University Press. Previous volumes can be obtained from the Periodicals Service Company at http://www.periodicals.com/oxford.html or Periodicals Service Company, 11 Main Street, Germantown, NY 12526, USA. E-mail: psc@periodicals.com. Tel: (518) 537-4700. Fax: (518) 537-5899.

Methods of payment

(i) Cheque (payable to Oxford University Press, to Oxford University Press, Cashiers Office, Great Clarendon Street, Oxford OX2 6DP, UK) in GB£ Sterling (drawn on a UK bank), US$ Dollars (drawn on a US bank), or EU€ Euros. (ii) Bank transfer to Barclays Bank Plc, Oxford Group Office, Oxford (bank sort code 20-65-18) (UK), overseas only Swift code BARC GB 22 (GB£ Sterling to account no. 70299332, IBAN GB89BARC20651870299332; US$ Dollars to account no. 66014600, IBAN GB27BARC206518660 14600; EU€ Euros to account no. 78923655, IBAN GB16BARC2 0651878923655). (iii) Credit card (Mastercard, Visa, Switch or American Express).

Environmental and ethical policies

Oxford Journals, a division of Oxford University Press, is committed to working with the global community to bring the highest quality research to the widest possible audience. Oxford Journals will protect the environment by implementing environmentally friendly policies and practices wherever possible. Please see https://academic.oup.com/journals/pages/authors/ethics for further information on environmental and ethical policies.

Advertising

To advertise in *Microscopy* contact:

Japan: Global Academic Publishing, Oxford University Press, 4-17-5-3F Shiba Minato-ku, Tokyo 108-8386, Japan. Tel: 03 5444 5858; Fax: 03 3454 2929.

Rest of the world: Advertising, inserts and artwork enquiries should be addressed to Advertising and Special Sales, Oxford Journals, Oxford University Press, Great Clarendon Street, Oxford, OX2 6DP, UK. Tel: +44 (0) 1865354767; E-mail jnlsadvertising@oup.com.

© 2019 The Japanese Society of Microscopy

All rights reserved: no part of this publication may be reproduced, stored in a retrieval system, or transmitted in any form or by any means, electronic, mechanical, photocopying, recording or otherwise without either the prior permission of the publishers, or a license permitting restricted copying.

To photocopy any work from this publication, you or your organization must obtain permission from one of the following which have been delegated for copyright clearance by the copyright owner. USA: Copyright Clearance Center Inc., 222 Rosewood Drive, Danvers, MA 01923, USA, Tel: (508) 750-8400; Fax: (508) 750-4744. UK: Copyright Licensing Agency Ltd, 90 Tottenham Court Road, London W1P 9HE. Rest of the world: The Copyright Council fo the Academic Societies, 41-6 Akasaka 9-chome, Minato-ku, Tokyo 107, Japan; Tel/Fax: +81 3 3475 5618.

Microscopy (ISSN 2050-5698) is published bimonthly in February, April, June, August, October and December by Oxford University Press, Oxford, UK and distributed in the USA by Central Mailing Services c/o UKP Worldwide, 1637 Stelton Road B2, Piscataway, NJ 08854. Annual subscription price is US $1184.00. Airfreight and mailing in the USA by agent named Central Mailing Services c/o UKP Worldwide, 1637 Stelton Road B1-2, Piscataway, NJ 08854. Periodicals Postage Paid at Piscataway, NJ and additional mailing offices.

US POSTMASTER: send address changes to *Microscopy*, Oxford University Press, Central Mailing Services c/o UKPWorldwide, 1637 Stelton Road B1-2, Piscataway, NJ 08854.

For further information please contact: Journals Customer Service, Oxford University Press, 4-17-5-3F Shiba Minato-ku, Tokyo 108-8386, Japan; Tel: +81 3 5444 5858, Fax: +81 3 3454 2929; E-mail: custserv.jp@oup.com.

Typeset by SPi Global, Manila, Philippines.
Printed by Bell and Bain, Glasgow, UK on acid-free paper.

MICROSCOPY
Previously Journal of Electron Microscopy

volume 68 • 2019 • number S1

contents

Plenary Lectures

SPL-1	Yasukazu Murakami	Electron Holography and Information Science: toward high-precision electromagnetic measurements	i2
SPL-2	Masahiro Ueda	Automated Single-Molecule Imaging Analysis in Living Cells and Its Applications to Cell Signaling	i3

Invited Lectures

SM-1	Yuta Yamamoto	Identification of Z-contrast image of twinned catalytic gold nanoparticles processed by Hough transformation using convolutional neural network	i5
SM-2	Naoya Amino	Studies on degradation process of brass-rubber interface by 3D element-specific images obtained from FIB-SEM	i6
SM-3	Yusuke Asari	Noise Reduction Method Based on Machine Learnings for Electron Holography	i7
SM-4	Yuki Nomura	Noise Reduction of Electron Holograms via Sparse Coding	i8
SM-5	Katsumi Hagita	Computational Geometry Analysis of Aggregations of Nanoparticles Filled in Rubbers through FIB-SEM Observations	i9
SM-6	Yoshitaka Adachi	Thorough quantification of micrograph by AI and advanced mathematics	i10
SC-1	Itsuro Kamimura	Introduction to practical AI image processing and analysis without programming	i11
SC-2	Kohki Konishi	Segmentation Method of Three Dimensional SEM Images of Biological Tissue	i12
SB-1	Masatsugu Toyota	Long-distance Ca^{2+} signaling via glutamate receptor channels in plants	i13
SB-2	Yoshiyuki Kubota	Acquisition of Large Volume EM Data Set and 3D Reconstruction with Automated Segmentation Application	i14
SB-3	Katsuyuki Shiroguchi	Combining live imaging and single-cell whole gene expression analysis by developing an automated cell picking system	i15
SB-4	Takumi Higaki	Semi-automatic organelle detection and recognition on electron microscopic images	i16
SB-5	Shumpei Ishikawa	Abstraction of Pathological Information and Integration of Cancer Genome Information	i17

Special Sessions

K-1	Kurio Fukushima	Road to Electron Microscope Development	i19
K-2	Masahiko Watanabe	Molecular-anatomical basis of synaptic circuit development in the cerebellum	i20
K-3	Tatsuo Ushiki	Scanning electron microscopy and scanning probe microscopy for visualizing the three-dimensional structure of cells and tissues	i21
K-4	Koji Kimoto	Current Status of Crystal Structure Analysis using Scanning Transmission Electron Microscopy	i22
SS1-1	Yutaka Yawata	Single-Cell Innate Fluorescence Analysis by Confocal Microspectroscopy	i23
SS1-2	Hayato Yamashita	High Resolution Dynamic Imaging of Living Bacterial Cell Membrane Molecules by High Speed AFM	i24
SS1-3	Yuya Sasajima	Internal Ribbon Structure Driving Helicity-Switching Swimming of *Spiroplasma*	i25
SS1-4	Katsuyuki Uematsu	3D reconstruction of intracytoplasmic membrane structure of methane-oxidizing bacteria by electron microscopy imaging	i26
SS2-1	Tatsuo Ushiki	Scanning probe microscopy and its biomedical application – from the historical viewpoint	i27
SS2-2	Hirofumi Yamada	Frontiers of AFM imaging method –high-resolution AFM in liquids and subsurface imaging–	i28
SS2-3	Katsuya Iwaya	Frontier of Low-Temperature Scanning Tunnelling Microscopy and Future Perspective	i29

SS2-4	Hiroshi Itoh	High resolution infrared imaging of composite materials	i30
KA-1	Osamu Ichii	Application of modified SEM techniques to evaluate renal pathology	i31
KA-2	Shunsuke Kobayashi	Structural Analysis Based on Measurements of Slight Cation Displacements from High Resolution STEM Images	i32
LS-1	Mitsutaka Haruta	Local electronic structure analysis and its mapping by STEM-EELS	i33

Poster Sessions

PM-01	Hirofumi Tsukasaki	Exothermic behavior and microstructures of the $LiNi_{1/3}Mn_{1/3}Co_{1/3}O_2$ positive electrode layer for all-solid-state lithium batteries	i35
PM-02	Hiromochi Tanaka	Analysis of Lithium Ion Battery Materials Using Statistical Machine Learning and Image Processing of Electron Microscopy Data	i35
PM-03	Yoshiki O. Murakami	New Magnetic Structure Imaging Techniques in Polycrystalline Materials by DPC STEM	i36
PM-04	Kagekatsu Kondo	Characterization of Sb_2Te_3 / GeTe Composite Thin Films Fabricated by RF-Magnetron Sputtering	i36
PM-05	Takeshi Ito	Anisotropic Electronic Structure of Metal Borides Studied by Soft X-ray Emission Spectroscopy	i37
PM-06	K.Matsuura	Electronic Structure of Nitrogen-Doped Graphite Films Studied by Soft X-ray Emission Spectroscopy	i37
PM-07	Yoshiki Hirayama	Structure Characterization of Bi-Doped SnSe Thin Films Fabricated by Pluse Laser Deposition	i38
PM-08	Shoichi Toh	Precipitation of Pigeonite and Enstatite in Augite of Ultrahigh Temperature Metamorphic Rock from Antarctica	i38
PM-09	Takato Yokoo	Evaluation of crystal structure and surface-to-molecule interaction in hydrothermally grown titanium oxide nanowires	i39
PM-10	Kinh-Luan Ngo-Huynh	Effect of microstructure on creep property of W-added heat resistant cast steel	i39
PM-11	Tomokazu Yamamoto	Atom Location Analysis on Atomic-resolution STEM Images of Metal Nanoparticles by Convolutional Neural Network Approach	i40
PM-12	Ryota Yamamoto	3D-structural distributions of silica aggregates in styrene-butadiene rubber obtained by FIB-SEM	i40
PM-13	Kazumi Takahashi	Three-dimensional analysis of porous material by FIB/SEM and correlation with physical property measurement	i41
PM-14	Fumiya Uehara	Three Dimensional Observations and Quantitative Analysis of Functional Polymer Materials	i41
PM-15	Tetsuya Okuyama	ZnO nanoparticles with fluorescent properties suitable for modification on protein surfaces	i42
PM-16	Eisaku Oho	Fast Scanning Method Applicable as a Standard Acquisition Mode for SEM	i42
PM-17	Kazuhiko Suzuki	Noise removal for SEM images using a convolutional neural network	i43
PM-18	Sadao Yamazaki	Technology for fundamentally improving an extremely low-quality video signal used for fine focusing and astigmatism correction in scanning electron microscopy	i43
PM-19	Keiichi Ueda	Deep learning analysis of Si(111)-7x7 surface in atomic force microscopy	i44
PM-20	Gen Maeda	Development of Software to Assist Contour Extraction of Objects from Electron Microscope Images Using Image Classification with Machine Learning	i44
PM-21	Sosuke Hattori	Optimization of hyperparameters in dictionary learning algorithm for peak detection of atom-resolved scanning transmission electron microscope images	i45
PM-22	Keita Kobayashi	Surveillance study on the SI-traceable nanometrology by transmission electron microscopy (TEM) and trial fabrication of reference materials for TEM	i45
PB-01	Hiroyuki Yamada	Comparison of the fundamental cell morphological properties examined with whole-mount ice-embedded cryo-TEM between 5 genera in family *Mycobacteriacea*	i46
PB-02	Tomoki Nishida	Observation of influenza virus particles by ultra-high resolution scanning electron microscope	i46
PB-03	Ilika Ghosh	Visualization of Compacted DNA of *Synechococcus elongatus* PCC7942 by DRAQ5 Labelling with DAB Photooxidation	i47
PB-04	Hazuki Minami	Electron micrographic analyses of the fine structure and properties of biodegradable plastics granules produced by microbes	i47
PB-05	Hiroshi Takase	Recycling of Uranyl acetate solution	i48
PB-06	Teruaki Konishi	Advanced microbeam irradiation system for single cell analysis of defensive cellular response against radiation	i48
PB-07	Kei Kato	Organelle detection from electron microscopic images by deep learning	i49
PB-08	Tsukika Tanaka	SEM analysis of long-term coenzyme Q10 deficient cell model	i49
PB-09	Naoko Kajimura	Visualization of F-Actin with Fascin in Filopodia by Cryo-Electron Tomography	i50
PB-10	Masashi Yamaguchi	High-pressure freezing method can be replaced by sandwich freezing method !?: electron microscopy of human tissues and cultured cells	i50
PB-11	Tomofumi Kurogane	3D-Modeling of Arabidopsis Root System Architecture by X-ray Micro-CT at SPring-8: Observation at Different Experimental Hutches	i51

PB-12	Yoshinobu Mineyuki	*In Vivo* Time-lapse Imaging of Changes in Air Space Distribution during Seed Imbibition in *Lotus miyakojimae* using X-ray Micro-CT	i51
PB-13	Masahiro Hosonuma	Three-dimensional ultrastructural analysis of bone-resorbing osteoclasts by Correlative Light Electron Microscopy (CLEM) and Focused Ion Beam Scanning Electron Microscope (FIB-SEM) suggested novel functions of osteoclasts	i52
PB-14	Toshiaki Tachibana	Effect of smoking inflammatory response to smoking cessation on human gingival fibroblast and periodontal ligaments cells	i52
PB-15	Shizuko Ichinose	Morphological Analysis of Reticular Dermis of Human Keloid Tissue	i53
PB-16	Tsubasa Sakamoto	Detection of Diatoms from the Viscera for the Diagnosis of Drowning by Using SEM	i53

Plenary Lectures

(SPL)

SPL-1 **doi: 10.1093/jmicro/dfz060**

Electron Holography and Information Science: toward high-precision electromagnetic measurements

Yasukazu Murakami[1,2]

[1] Department of Applied Quantum Physics and Nuclear Engineering, Kyushu University, Fukuoka, Japan, [2] The Ultramicroscopy Research Center, Kyushu University, Fukuoka, Japan

Electron holography (EH) allows for determination of an electromagnetic field from a nanometre-scaled area. Because of this function, EH has been applied to essential problems of physics and materials science: these include verification of the Aharonov-Bohm effect [1], mapping of electrostatic potential from semiconductors and Li-ion batteries [2,3], magnetic flux density measurements from narrow interface regions [4,5], and many other applications. It is expected that a high-voltage electron holography microscope with Cs correction [6] achieves an atomic resolution in the electromagnetic field observations (Cs represents the effect of spherical aberration). An issue of EH, which remains challenging, is the improvement of sensitivity to the electromagnetic field in thin foils and nanoparticles. Presumably, an effective approach to this problem is using techniques of information science—this provided us a motivation to carry out this research project.

As indicated by Lichte and Lehman [7], detection limit of the phase shift is affected by image quality of electron holograms: *i.e.,* image contrast of holograms, number of electrons *per* CCD pixels, and others. However, a long-time exposure of electrons (*i.e.,* a conventional way to improve the image quality) induces undesired radiation damage and/or contaminations in specimens. Thus, for many occasions, we have to use electron holograms with insufficient image quality.

In order to solve this technical problem, two methods of information science have been employed. One of the methods is averaging many holography observations (*i.e.,* reconstructed phase images). The concept appears to be similar to that of the single-particle analysis for protein crystals [8] although our holography study aims at catalysis particles (and other inorganic nanoparticles) showing significant dispersions in both size and shape. To analyze those catalyst particles showing a large dispersion, the holography observations were identified and/or classified with the aid of machine learning [9]. The other method is of noise reduction from individual holograms. We applied a hidden Markov model to the noise reduction using wavelet transformations [10]. An advantage of this method is that it can provide a criterion to separate weak signal from noise during the image analysis. We shall discuss about the efficiency of this method.

The author thanks collaborators for their contributions to this electron holography study: Drs. Y. Asari, H. Shinada, T. Tanigaki, Y. Takahashi, T. Akashi, S. Terada (Hitachi Ltd.), Professors Y. Midoh, K. Miura, K. Nakamae (Osaka Univ.), Drs. H. Nakajima and Y. Cho, and Ms. A. Sato (Kyushu Univ.). This study was supported by JST, CREST (JPMJCR1664).

1. A. Tonomura in “Electron Holography”, Springer-Verlag, Berlin (1999) 50.
2. Y. Nomura et al, Microscopy 67 (2018) 178-186.
3. K. Yamamoto et al, Microscopy 66 (2017) 50-61.
4. Y. Murakami et al, Acta Mater. 71 (2014) 370-379.
5. T. Tanigaki et al, Sci. Rep. 7 (2017) 16598.
6. T. Akashi et al, Microscopy 67 (2018) 286-290.
7. H. Lichte and M. Lehmann, Rep. Prog. Phys. 71 (2018) 016102.
8. J. Frank, Microscopy 65 (2016) 3-8.
9. Y. Asari et al, Proc. 74th Annual Meeting of The Japanese Society of Microscopy, Kurume (2018) 94.
10. Y. Midoh and K. Nakamae, Proc. 37th NANO Testing Symposium (NANOTS 2017), Osaka (2017) 123.

SPL-2

doi: 10.1093/jmicro/dfz061

Automated Single-Molecule Imaging Analysis in Living Cells and Its Applications to Cell Signaling

Masahiro Ueda[1,2]

[1]Graduate School of Frontier Biosciences, Osaka University and [2]RIKEN, Center for Biosystems Dynamics Research (BDR).

The method of imaging the behaviors of single molecules in living cells can be a powerful analytical method for basic biology as well as medical science and applied fields such as drug discovery. The efficiency of the imaging measurement and data analysis using the optical microscope, which was a concern, was greatly improved by automation using robot technology and machine learning (Figure 1). A high-throughput system capable of comprehensive analysis of signaling molecules in living cells was realized. In my talk, the background to the development of the automated single-molecule imaging system will be introduced, and applications to cell signaling will be also introduced.

Single-molecule imaging of biomolecules can not only observe molecules but also measure the dynamics and kinetic of molecular reactions, and its application range is very wide. From the practical use of single-molecule imaging in vivo in the 1990s to single-molecule imaging in living cells, Japanese researchers has been at the forefront of technological development [1-4]. Recently, we succeeded in fully automated single molecule imaging analysis [5]. For single molecule imaging, we used an objective total internal reflection fluorescence microscope (TIRFM) [6]. This system was constructed in an incubator that can control temperature, humidity, and CO2 concentration. Functions such as automatic focusing, automatic cell recognition, automatic oil supply for objective lens, automatic cell sample transport, and automatic solution addition are available. Thus, this system can recognizes cells, focuses on the cells, and records single-molecule images automatically. Microscope operation and cell recognition often require skilled experimental researchers' craftsmanship, but the realization of this automation using machine learning and robotics can contribute to accrelation of imaging analysis. Automatic measurement of 1,600 cells per day, about 1,000,000 molecules is possible. In fact, we succeeded in the automatic measurement and analysis of EGF receptors important for cell growth, and we were able to quantify their diffusion movement and multimer formation [5]. This is about 100 times more efficient than human experiments, and more than 10 times more efficient than skilled researchers. Further development of this system will enable a new screening method for drugs and genes based on behaviors of single molecules [7-8]. Furthermore, the automation of life science using AI and robotics may open up new life sciences.

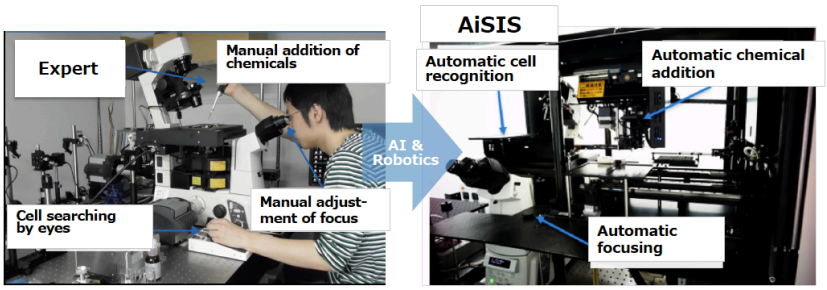

Fig. 1. Artificial intelligence aids automatic monitoring of single molecules in cells. Single-molecule imaging was fully automated in a manner that overcomes the need for technical expertise, such as precisely adjusting the focus and searching for analyzable cells, by an artificial intelligence-aided system.

The development of an automated single-molecule imaging system was realized through collaborative research with M. Yasui, M. Hiroshima, J. Kozuka and Y. Sako. I would like to express my gratitude here. This study was supported by the JST-SENTAN program since October 2013 and by AMED-SENTAN since April 2015. This study was also partially supported by AMED-CREST JP17gm0910001.

1. T Funatsu et al, Nature 1374 (1995) 555-559.
2. Y Sako et al, Nature Cell Biology 2 (2000) 168-172.
3. M Ueda et al, Science 294 (2001) 864-867.
4. R Iino et al, Biophys J. 80 (2001) 2667-2677.
5. M Yasui, M Hiroshima et al, Nature Communications 9 (2018) 3061.
6. M. Tokunaga et al, Biochem Biophys Res Commun. 235 (1997) 47-53.
7. M Hiroshima et al, J. Mol. Biol. 430 (2018) 1381-1396.
8. M Yanagawa et al, Science Signaling 11 (2018) eaao1917.

Invited Lectures

Materials and Instruments (SM)

Common Fields (SC)

Medical and Biological Sciences (SB)

SM-1

doi: 10.1093/jmicro/dfz054

Identification of Z-contrast image of twinned catalytic gold nanoparticles processed by Hough transformation using convolutional neural network

Yuta Yamamoto[1], Junya Ohyama[2], Atsushi Satsuma[3], Nobuo Tanaka[1] and Shunsuke Muto[1]

[1]Institute of Materials and Systems for Sustainability, Nagoya University, Furo-cho, Nagoya, Japan, [2]Faculty of Advanced Science and Technology, Kumamoto University, Kurokami, Chuo-ku, Kumamoto, Japan, and [3]Department of Materials Chemistry, Graduate School of Engineering, Nagoya University, Furo-cho, Nagoya, Japan

Deep learning (DL), where artificial intelligence (AI) builds connection weights between neural network multi-layers for recognition, prediction, and other functions by itself on the basis of iterative learning, has attracted significant attention as an alternative image authentication method [1]. Convolutional neural networks (CNN), one of the DL algorithms developed in the 1980s [2], are a pioneer of the latest DL progress in image identification applications, replacing several layers of neural networks that are fine-adjusted by the professional human effort [3].

Supported Au nanoparticles (AuNPs) with diameters of less than 5 nm showing high catalytic activity towards CO oxidation can exhibit high catalytic activity if they contain more twinned rather than single-crystal AuNPs [4,5]. As an automatic identification method for twin AuNPs in its crystal structure was desired, the our research group demonstrated the successful identification of twinned/untwinned catalytic AuNP using a self-prepared CNN trained using Hough transformed (HTed) atomic resolution Z-contrast images of supported AuNPs [6]. In this study, the primary success factors for this identification are investigated.

The figure shows the successful CNN network architecture on the left side and visualized graphics of the strongest CNN activations in the input layer and each convolution layer by typical Z-contrast images of single/twinned AuNP and its HTed patterns on the right side. In the third convolution layer, as each HTed single AuNP shows a vertical streak pattern originating from localized signature spots arranged in tandem, which is not indicated in the HTed twinned AuNP, the CNN is proposed in order to recognize them. In contrast, the CNN cannot discriminate single AuNP Z-contrast images from twinned ones because these develop similar patterns without the feature of the lattice fringes direction; these were originally different in Z-contrast images through the network.

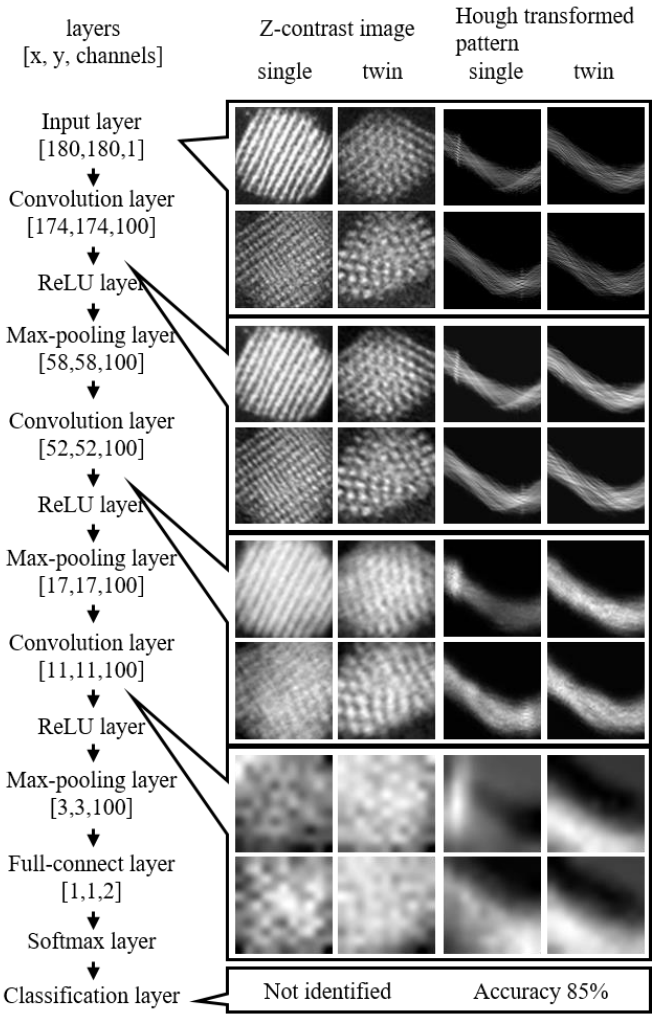

Fig. CNN network architecture (left side) and visualized graphics of the strongest CNN activations in the input layer and each convolution layer by typical Z-contrast images of single/twinned Au nanoparticles and their Hough transformed patterns (right side).

1. Y LeCun et al., Nature 521 (2015) 436-444.
2. K Fukushima, Biol. Cybernetics 36 (1980) 193-202.
3. A Krizhevsky et al., NIPS'12 Proceedings (2012) 1097-1105.
4. A D Pandey et al., J. Phys. Chem. C 114 (2010) 19386-19394.
5. J Ohyama et al., Chem. Commun. 51 (2015) 15823-15826.
6. Y Yamamoto et al., Microscopy 67 (2018) 321-330.

SM-2 doi: 10.1093/jmicro/dfz055

Studies on degradation process of brass-rubber interface by 3D element-specific images obtained from FIB-SEM

Naoya Amino[1].

[1]Research and Advanced Development Division, The Yokohama Rubber Co., Ltd., Tokyo, Japan.

Introduction

Automobile tires are composed of several kinds of rubber compounds and reinforcement materials which are steel and textile cords. Generally, the steel cords are embedded under a tire tread part and enhance driving performances of the tire. Since the steel cords under the tire tread is usually plated by brass, strong adhesion between brass plating and rubber is formed in tires. However, it is known that the adhesive layer between brass and rubber is degraded by exceeding heat and humidity [1]. Insufficient adhesion between the steel cords and rubber causes failure of tires. These tire failures might induce tire tread separation and serious automobile accidents. Therefore, sufficient and stable adhesion between brass plating and rubber is required for automobile safety. In this study, I discussed that degradation process of brass-rubber adhesive interfaces by using FIB-SEM to observe 3D morphological changes.

Experimental

A single steel cord (diameter: 345 μm) with brass plating (thickness: 0.3 μm) was used in this study. The cord was coated with the rubber and vulcanized at 170◦C for 10 min. The vulcanized specimen was treated at 70◦C under 96% humidity for 14 days. An FIB-SEM (NX9000, Hitachi High-Technologies Corporation, Japan) was used for 3D structural observations. The FIB and SEM were operated at 30 and 2 kV, respectively. As illustrated in Fig. 1(a), the interfaces between the steel code with brass plating and rubber were observed by repeated process of FIB sectioning and SEM observation using backscattered electron (BSE) imaging. The sectioning pitch was 20 nm. This repeated process can obtain a series of SEM images at different depths in the materials, which are then stacked together to generate a 3D reconstruction [2]. During the FIB-SEM observation, elemental analysis with EDX (X-Max 100TLE; Horiba, Japan) at accelerating voltage of 200kV was carried out every 2 μm depth. By comparing the EDX images with BSE images, the interfacial structures were segmented into each chemical component.

Results and discussion

The 3D structure of the adhesive interface before aging is shown in Fig. 1(b). ZnO and Cu_xS layers were observed between brass and rubber layers. Whisker-like structure was observed at Cu_xS layer. The thickness of ZnO layer was 10-40 nm, and that of Cu_xS layer was 50-100 nm. 14 days heat/humidity treatment enlarged ZnO and Cu_xS layers as shown in Fig.1(c). The thickness of Cu_xS layer was 150-400 nm. Moreover, the whisker-like structure disappeared after aging, and Cu_xS layer included rubber and ZnO particles. These results suggest that Cu atoms diffused from brass layer to the rubber compound during the aging treatment, then the Cu atoms reacted with sulfur in rubber compound and foamed into Cu_xS.

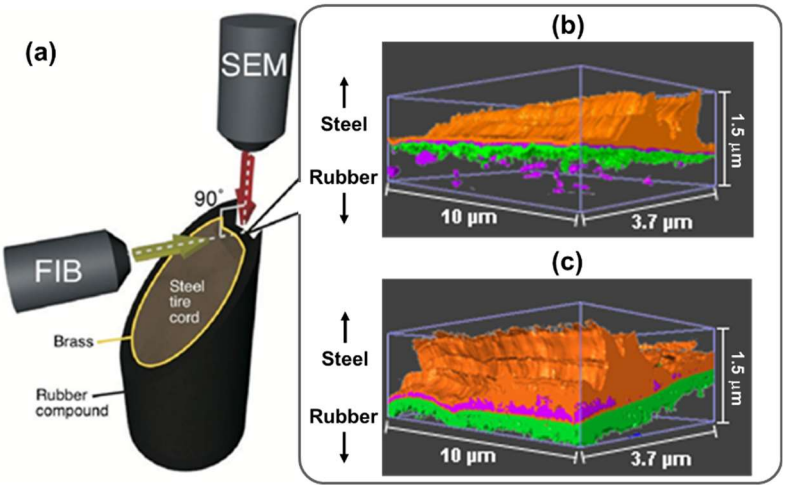

Fig. 1. (a): Schematic illustration of FIB-SEM analysis of adhesive interface between steel cord plated with brass and rubber, (b) and (c): 3D elemental mapping images [brass (orange), Cu_xS (green) and ZnO (purple)] at the adhesive interface. (b) shows the image of the interface before aging and (c) is that of after aging.

Conclusion

It is thought that thick and heterogeneous structure of adhesive interface after aging weaken the adhesive force.

References

1. K. Shimizu, T. Kakubo, N. Amino and K. Ozawa, J. Soc. Rubber Sci. and Technol., Japan, 88 (2015) 291-296.
2. M. Kato, T. Ito, Y. Aoyama, K. Sawa, T. Kaneko, N. Kawase and H. Jinnai, J. Polym. Sci. Part B, 45 (2007) 677-683.

SM-3

doi: 10.1093/jmicro/dfz056

Noise Reduction Method Based on Machine Learnings for Electron Holography

Yusuke Asari

Research and development group, Hitachi, Ltd.

In the study of reaction mechanisms for chemical catalytic systems, it is important to understand the microscopic structures and chemical properties of the reaction center. Because it can be considered that the catalytic activities are greatly affected by the atomic-scaled surface structure, the chemical composition, the local charge transfers, and the chemical stabilities, so far the catalytic activities has been improved mainly by modifications of the surface[1]. The surface modifications may affect on the electric and magnetic fields around the reaction center.

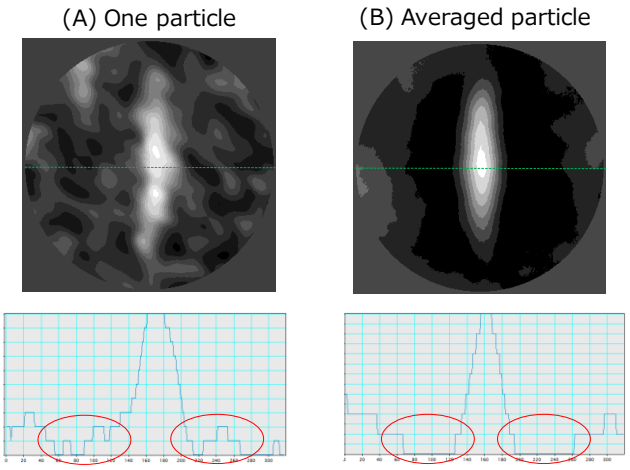

Fig. 1. Image of one particle (A) and averaged particle (B). The averaged image is generated from 63 images of iron oxide particle. The corresponding line profiles are shown below the particle images.

The electron holography technique [2] is a powerful tool to investigate the electric and magnetic fields of materials. By using the holography techniques, the magnetic fields of the phase boundaries [3] and the charge transfer in particles [4] have been successfully observed. However, it is considered that the sensitivity for detecting the phase difference is not enough high to obtain the information of catalytic activities. To improve the sensitivity, one of the effective method is noise reduction. The noise is generated in both the measurement and the image processing. Former is an interference process of divided electron waves using biprism, and the latter is an operation of Fourier transformation in the image treatment. Many studies have made great efforts to suppress the noise, for example, by using aberration-correctors [5], multiple acquisition [6] and phase-shift methods [7].

Our idea is an application of deep-convolutional-neural-network (DCNN) [8] to the improvement of the signal-to-noise ratio. Due to recent progresses of the information technology, the image recognition ability by the DCNN shows the same level as human. Even if the electron hologram with huge number of particles is acquired, DCNN is able to classify these images into preset groups. By calculating average of the huge number of classified images, the signal-to-noise ratio will be improved.

In this work, we applied the DCNN to reduce the noise in the electron holography. As the first experiment, monodispersed spindle-like particles of iron oxides were used for the target material. The 61 hologram images were obtained by using Hitachi HF-3300X with an accelerating voltage of 300 kV. The holograms of the 493 particles were classified into 10 classes we defined in advance. The particle image of a class was denoised by averaging 63 images. Our result shows that the signal-to-noise ratio of electron hologram can be improved by averaging method combined with DCNN based classification technique if sufficient number of images is acquired.

Acknowledgement
This work is partially supported by JST CREST Grant Number JPMJCR1664, Japan.

1, H. Zhang, T. Watanabe, M. Okumura, M. Haruta, and N. Toshima, Nature Mater. 11, 49 (2011).
2, D. Gabor, Nature 161, 777 (1948).
3, Y. Murakami, K. Niitsu, T. Tanigaki, H.S. Park, R. Kainuma, and D. Shindo, Nature Commun., 5, 4133 (2014).
4, T. Tanigaki, K. Sato, Z. Akase, S. Aizawa, H.S. Park, T. Matsuda, Y. Murakami, D. Shindo, and H. Kawase, Appl. Phys. Lett. 104, 131601 (2014).
5, D. Geiger, H. Lichte, M. Linck, and M. Lehmann, Microsc. Microanal. 14, 68 (2008).
6, E. Völkl, and D. Tang, Ultramicroscopy 110, 447 (2010).
7, Q. Ru, J. Endo, and T. Tanji, Appl. Phys. Lett. 59, 2372 (1991).
8, A. Krizhevsky, I. Sutskever, and G.E. Hinton, NIPS Proceedings 1106 (2012).

SM-4 **doi: 10.1093/jmicro/dfz057**

Noise Reduction of Electron Holograms via Sparse Coding.

Yuki Nomura[1], Satoshi Anada[2], Tsukasa Hirayama[2], Emiko Igaki[1] and Kazuo Yamamoto[2]

[1]Panasonic Corporation, Technology Innovation Division, Osaka, Japan, [2]Japan Fine Ceramics Center, Nanostructures Research Laboratory, Nagoya, Japan.

Electron holography is one of the techniques of transmission electron microscopy (TEM) to visualize electromagnetic fields at the nanometer scale. Electron interference patterns (holograms) are formed by overlapping the object wave and the reference wave using an electron biprism. The phase in the object wave is modulated by the electromagnetic fields and is recorded as a bending of the interference fringes. To precisely visualize the electromagnetic fields, it is important to acquire the holograms with high signal to noise (S/N) ratio because random noises (shot noise, quantum noise etc.) in holograms limits the precision and accuracy of the phase detection. Long acquisition time reduces the noises, but it causes the spatial drifts of the sample and biprisms during the acquisition. This effect possibly degrades the spatial resolution and the fringe visibility of the interference patterns.

Here we propose an image processing technique with sparse coding to reduce the noises in the holograms taken by high speed acquisition [1]. Recently, it has been shown that the sparse coding algorithms improve the image quality of scanning electron microscopy (SEM) [2], electron tomography [3], and scanning transmission electron microscopy [4–6] by inpainting and denoising. In this study, we applied two step strategies of sparse coding to reduce the noises. In the first step, we extract hidden features from training holograms recorded with long acquisition time. Subsequently, using the extracted features, we sparsely represented the test holograms recorded with short acquisition times, resulting in the noise reduction.

We used GaAs p-n junction as a model sample. Figures 1(a)–(d) show the two sets of training holograms to extract hidden features of holograms and to determine the appropriate parameters of sparse coding algorithms. Figures 1(e)–(j) show original holograms and denoised holograms via sparse coding. The algorithms effectively reduce the noises and improve the quality of the holograms. In the presentation, quantitative comparison of reconstructed phases and precision of the phase detection will be discussed.

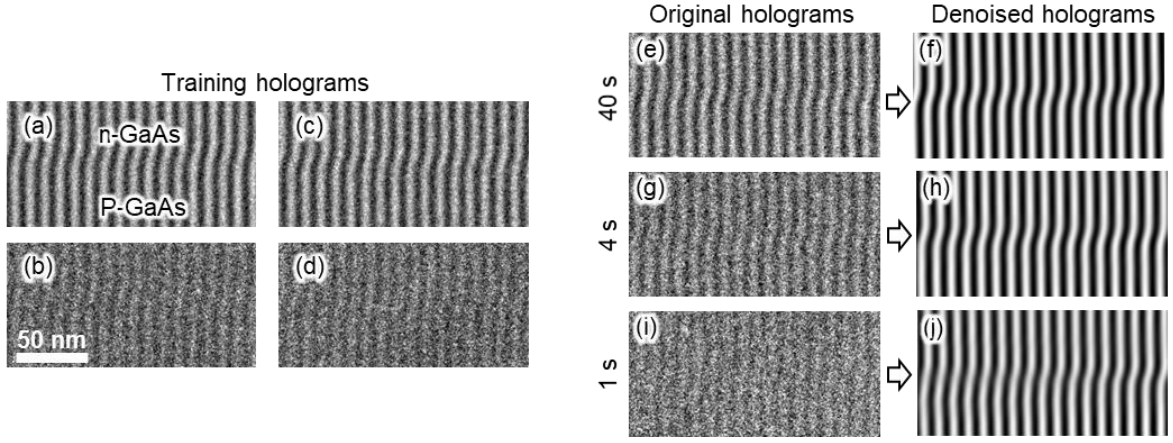

Fig. 1. Denoising of electron holograms by sparse cording. (a)–(d) Two sets of training holograms of GaAs p-n junction. (e)–(j) Original and denoised holograms with 40, 4, 1 sec acquisitions, respectively. Reprinted with permission from Ref. [1]. Copyright 2019 Elsevier V.B.

1. S. Anada et al., Ultramicroscopy 206 (2019) 112818.
2. H.S. Anderson et al., IS&T/SPIE Electr. Imaging 8657 (2013) 1–12.
3. Z. Saghi et al., Ultramicroscopy 160 (2016) 230–238.
4. A Stevens et al., Microscopy 63 (2014) 41–51.
5. A Stevens et al., Appl. Phys. Lett. 112 (2018) 043104.
6. A Stevens et al., Appl. Phys. Lett. 113 (2018) 033104.

SM-5 doi: 10.1093/jmicro/dfz058

Computational Geometry Analysis of Aggregations of Nanoparticles Filled in Rubbers through FIB-SEM Observations

Katsumi Hagita[1]

[1]Department of Applied Physics, National Defense Academy, Yokosuka, Japan.

Filler-filled rubber is of great interest as a system in which the 3D structure of fillers in a volume from nanometer to micrometer dimensions greatly influences the structure-property relationships. For the cases of tire rubbers, fillers' nanostructure (morphology), whose order is 100nm, is important on their mechanical functions such as fuel efficiency. When the fillers were more dispersed, rolling resistance became smaller. To realize high-fuel-efficient tire, silica nanoparticles (NPs) were used as fillers in order to disperse fillers' aggregations with coupling agents. Note that carbon black NPs have been used for the conventional tire rubbers. Recently, in order to further improve the dispersity, a polymer modified so that the polymer-ends adsorb to fillers was used. Figure 1 (a,b) shows TEM observations for the modified and non-modified SBR (styrene-butadiene rubber) [1]. Difference of dispersity was clearly found. Here, the primary shape of the silica NPs can be regarded as a sphere whose diameter is a few ten nanometers. NP-morphologies in a volume of micro-meter dimension is important. To investigate characteristic structures in the scale of 1 μm dimension, ultra small angle x-ray scattering (USAXS) experiments were extensively performed. In our previous work [1], we estimated 3D structure models of NPs from USAXS-data by using reverse Monte Carlo (RMC) searches. Here, we achieve 3D modeling of NPs configurations under the periodic boundary box with the cubic-dimension of 9 μm. The snapshots of the estimated 3D structures were very similar to those of TEM. According to our evaluation of the reproducibility of the RMC method [2], the reproducibility of the statistical properties of the geometric quantities was examined using the coarse-grained molecular dynamics simulations of the gel filled with NP as reference data. We found that the reproducibility of the neighboring structures of NPs was not good, but the reproducibility of the middle-range structure between the NP aggregates was good. Thus, to perform computational geometry analysis based on mathematics, we need a method that can evaluate the structures of neighboring NPs with high reliability. That is 3D microscopy such as 3D-TEM and FIB-SEM.

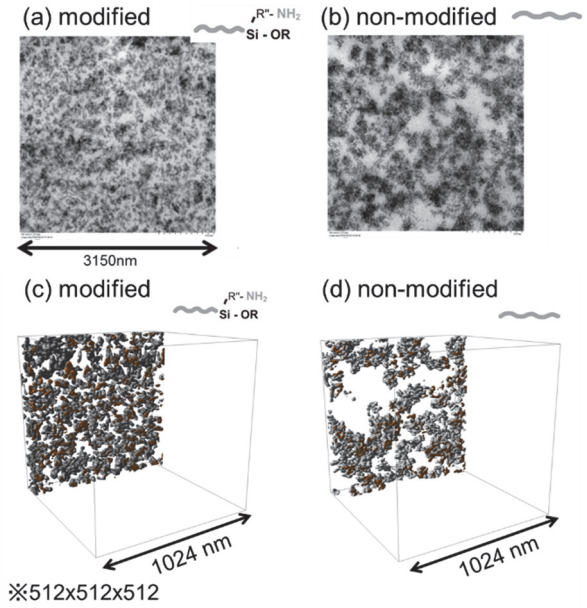

Fig. 1. (a,b) Snapshots of TEM observations and (c,d) FIB-SEM observations.

Recently, we have performed FIB-SEM observations to grasping the morphologies of NPs in large volume [3]. As shown in Figure 1 (c,d), clear difference of NPs' aggregations between the modified and non-modified SBR can been seen. The volume fraction of NP in this system is 16%, and the aggregates of NPs can be regarded as isolated clusters. Here, since the larger clusters were larger than the observation range (1 μm), appropriate statistics are not easy for larger clusters. Taking advantage of the features of FIB-SEM observations, we investigated the statistical properties of dispersed medium-sized clusters in detail. Note that by using 3D watershed segmentations [4], we confirmed that the number segmented into individual NPs roughly agreed with the value estimated from the average NP-diameter of 18.8 nm. Here, we should remind that the degree of dispersion of the diameters was not small (0.2). We can conclude that FIB-SEM observations can capture individual NPs in rubber.

From viewpoints of computational geometry analysis, we investigated characteristic behaviors of the observed isolated clusters of NPs. Detail results and discussions are given in this presentation.

1. K. Hagita, T. Tominaga, T. Sone, Polymer 135 (2018) 218-229.
2. K. Hagita, Soft Matter (2019) in press.
3. K. Hagita, T. Higuchi, H. Jinnai, Sci. Rep. 8 (2018) 5877.
4. R. Yamamoto, et al, a poster presentation in this symposium (2019).

SM-6 doi: 10.1093/jmicro/dfz059

Thorough quantification of micrograph by AI and advanced mathematics.

Yoshitaka Adachi[1], Toshio Ogawa[1], Zhi-Lei Wang[1], Kohei Enya[1], Fumito Ajioka[1]

[1]Department of Material Design Innovation Engineering, Nagoya University, Nagoya, Japan.

1.Introduction

Topological optimization of microstructures is a potential method to improve material properties. However less efforts have been performed to modify morphology of microstructures drastically, because characteristic morphology of microstructures is unlikely produced reproducibly. To realize topological optimization of microstructures, it is required to quantify microstructures as much as possible. For this purpose, metallurgically as well as mathematically important features of microstructure should be extracted intensively from 2D/3D images. As the first step of intensive microstructure analysis, computer vision also seems to be useful. This presentation will focus on the recent "Computer eye" to quantify microstructures.

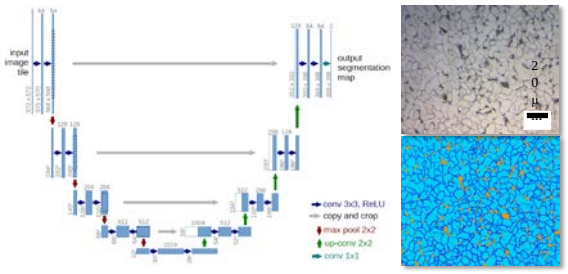

Fig.1 Microstructure detection by U-net.

2. Computer vision

A conventional image processing using well-known filters followed by thresholding sometimes does not work well and is time-consuming. Instead of conventional image processing, AI-assisted image processing is currently received much attention in medical field to detect cancer cells in radiographs. U-net (Fig.1) as a latest computer vision algorithm is applied to object detection in materials science filed, and it is confirmed that it can detect not only big objects but also fine or thin objects in microstructures. Another recent attention paid in computer vision is XAI, where heat map is shown to understand how computer recognizes an object.

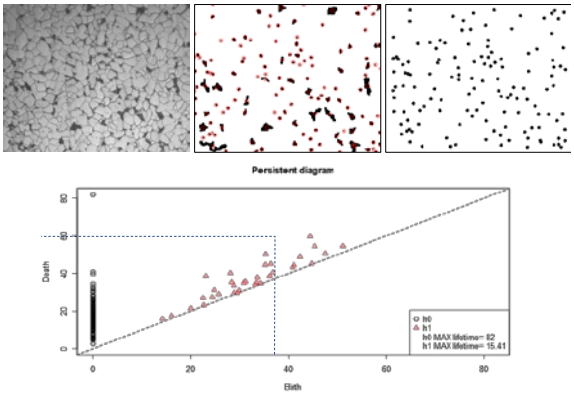

Fig.2 PH diagram of DP microstructure.

3. Intensed quantification

In addition to metallurgically important features of microstructures, mathematically important features are also useful to quantify microstructures intensively. For example, compared with conventional topology using Euler number or genus, persistent homology (PH) evaluates incomplete connectively of microstructures. Two-point correlation function which is used to analyze star distribution in galaxy universe characterize second phase distribution in microstructure as a function of distance between particles.

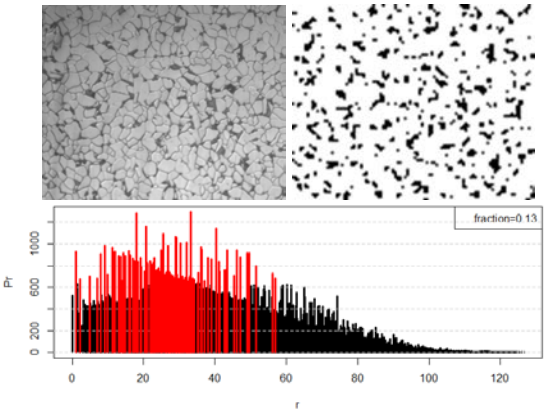

SC-1 **doi: 10.1093/jmicro/dfz052**

Introduction to practical AI image processing and analysis without programming

Itsuro Kamimura[1], Mike Marsh[2], Takanobu Ishimura[1], Shigeru Yoneyama[1]

[1] Maxnet Co., Ltd. Tokyo, Japan, [2] Object Research Systems, Montreal, Canada

I will introduce specific examples of easy-to-use AI image processing without programming. It can be realized by using package software called Dragonfly (Object Research Systems, Montreal, Canada). Its deep learning solution is powered by Google's TensorFlow and Keras. It provides deep learning models can be trained for image segmentation, denoising, and super-resolution.

Image Segmentation is the single most universal bottleneck to quantitative analysis. Deep Learning solution offers a straightforward, easy to use workflow that allows users of all levels to perform advanced segmentation tasks rapidly. This level of automated image segmentation is transformative for high-throughput quantitative image analysis. I will explain the workflow of the deep learning and how the segmentation was done without programming.

Super Resolution is upscaling and improving image detail by applying super-resolution with Deep Learning solution.

Denoising is suppressing noise and restoring the original image, denoising with Deep Learning solution plays a crucial role in preparing data for downstream analysis.

Keywords: Machine Learning; Deep Learning; CNN; Image Segmentation; Super Resolution

Fig. 1. Automated segmentation of a denim fabric sample with Deep Learning's U-Net model. Dataset courtesy of Rigaku

SC-2

doi: 10.1093/jmicro/dfz053

Segmentation Method of Three Dimensional SEM Images of Biological Tissue

Kohki Konishi[1], Masafumi Mimura[1], Takao Nonaka[1], Ichiro Sase[1], Keisuke Ohta[2], Hideo Nishioka[3] and Mitsuo Suga[3].

[1]Nikon Corporation, Yokohama, Kanagawa, Japan, [2]Kurume University, Kurume, Fukuoka, Japan and [3]JEOL Ltd., Akishima, Tokyo, Japan

Segmentation process of objects of interest from three-dimensional (3D) images is essential to understand the 3D structure and spatial relationship between them and their neighbourhood structures. Manual segmentation is widely accepted, but time-consuming and laborious especially for large dataset. Deep convolutional neural network (CNN)-assisted segmentation also works well; however, they require a large training dataset, which is a major impediment [1]. We present a practical 3D segmentation method with reduced training dataset compared to conventional works [2] and application examples to SEM array tomography images [3].

Our segmentation method consists of five processes: preparation for training dataset, model training, inference, proofreading, and 3D reconstruction. Training dataset consists of raw images themselves and their corresponding ground truths. Ground truths are manually or semi-automatically created depending on their shapes. Our model uses a fully convolutional network called U-Net [4] with smaller depth and fewer filter numbers. Inference is performed to all the images not contained in the training dataset. Proofreading is the process of correcting mistakes by comparing raw images with binarized inference results. 3D reconstruction is the process constructing 3D images from segmentation results in different Z images. We developed an all-in-one tool executable for Windows OS.

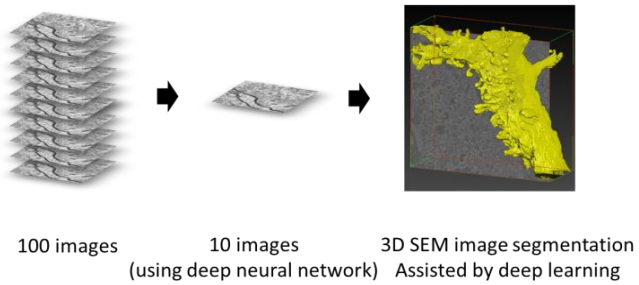

Fig 1. Training dataset size and segmentation result. Conventional methods [1] require 100 images for training neurite segmentation (left), while ours requires 10 images (middle). We combine CNN with classical image processing algorithms to produce segmentation result (right).

We created two 3D image datasets of mouse cerebellum cortex captured using SEM array tomography [3]. One is to extract cell membrane [2], and the other is to extract cell nuclei [5]. We used the former dataset to segment a dendrite of a Purkinje cell. We compared manual labour time of segmentation methods. We selected 10 images from the dataset and created their ground truths for training while conventional method [1] uses 100 of them (Fig 1). The total time was 9 hours for our method while that for the conventional method was estimated to be 28 hours. Most of the time for the conventional method was used for preparing training dataset. From comparison, we conclude that we can reduce the manual labour time by reducing training dataset size.

We then used the latter dataset to segment a dozen of whole cell nuclei. Fig 2 left shows an example. Due to fewer training dataset size, some of nuclei was segmented incompletely, showing bright and dark regions inside nuclei (Fig 2 middle). We applied an active contour algorithm [6] for proofreading, improving segmentation result (Fig 2 right). This indicates that combination of CNN with active contour algorithm improves segmentation accuracy. We conclude that we can extract cell nuclei with small training dataset by combining CNN with other algorithms.

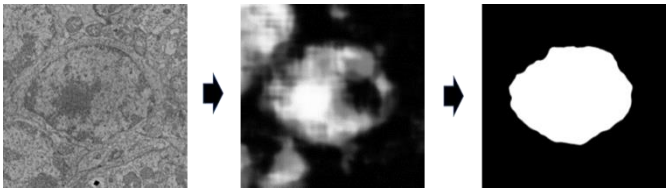

Fig 2. An image example (left), incomplete segmentation result (middle), and proofread result (right)

1. Arganda-Carreras et al., Front. Neuroanat., 9 (2005), page 1-13
2. Konishi et al., Microscopy, 68 (2019), page 338-341
3. Micheva and Smith, Neuron, 55 (2007), page 25-36
4. Ronneberger et al., MICCAI, (2015)
5. Suga et al., Microscopy and Microanalysis, 24 (2018), page 1248-1249
6. Chan and Vese, Transactions on Image Processing, 10 (2001), page 266-277

SB-1

doi: 10.1093/jmicro/dfz047

Long-distance Ca^{2+} signaling via glutamate receptor channels in plants.

Masatsugu Toyota[1]

[1]Department of Biochemistry and Molecular Biology, Saitama University, Saitama, Japan.

Unlike animals, the sessile organism plants do not have the central nervous system, but they can rapidly sense local environmental stresses, such as salt, drought, light and mechanical stresses (pest/pathogen attack, touch and gravity), transmit this information throughout the plant body and activate systemic responses (Fig.1). However, the molecular nature underlying such rapid sensory and plant-wide signal transduction remains largely unknown.

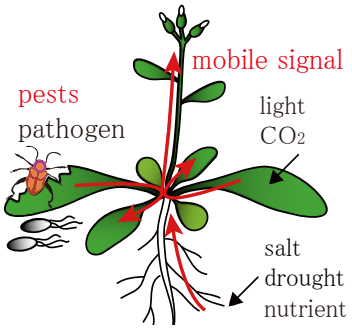

Fig. 1. Long-distance signaling in plants.

We have produced wide-field fluorescent imaging system and the model plant *Arabidopsis thaliana* expressing genetically-encoded highly-sensitive Ca^{2+} indicators such as GCaMPs [1] in order to visualize plant-wide cytosolic Ca^{2+} dynamics ($[Ca^{2+}]_c$) in real time and uncover a possible role of $[Ca^{2+}]_c$ in the systemic, rapid signaling network [2-3]. Here, we show that glutamate is a wound signal in plants that leaks to the extracellular region (apoplast) from damaged cells/tissues. The *GLUTAMATE RECEPTOR LIKE* (*GLR*) family of ion channels acts as sensors that convert this damage-associated signal into an increase in $[Ca^{2+}]_c$ that propagates to distal leaves where defence responses are triggered [4].

Mechanical wounding of rosette leaves and herbivory by the cabbage white butterfly caterpillars (*Pieris rapae*) triggered an immediate $[Ca^{2+}]_c$ increase at the damaged site that was transmitted through the vasculature (at ~1000 μm/s), reaching within 1-2 minutes to specific distal target leaves. Phloem-specific GCaMPs driven by pSUC2 clarified that this Ca^{2+} signal propagates through the sieve tube and/or companion cells, suggesting that the phloem has important roles not only in transporting nutrients throughout the plant body but also in long-distance rapid signal transduction upon wounding. In the target leaf, the plant stress hormone jasmonate (JA) and jasmonoyl-isoleucine (JA-Ile) was rapidly accumulated and JA-dependent defense marker genes were highly upregulated after the Ca^{2+} transmission. Furthermore, a mutant with reduced plasmodesmatal connection due to callose accumulation showed an abnormal Ca^{2+} transmission pattern moving through target leaves and weak JA-dependent defense marker gene induction. These data support our model where Ca^{2+} acts as a systemic wound signal triggering JA-related defense responses transmitted over long-ranges through the phloem and then generating local responses through cell-to-cell communication via plasmodesmata.

To reveal the molecular nature used to sense the initial signal of wounding and the mechanisms of the intracellular Ca^{2+} signaling network, GCaMPs were expressed in mutants of *GLR* channels. *glr3.3glr3.6* double knockout mutants showed no Ca^{2+} wave upon mechanical wounding. When glutamate (Glu) was applied to a leaf, almost identical long-distance Ca^{2+} transmission and defense gene induction were triggered in wild type but not *glr3.3glr3.6* mutants. Such results are consistent with a model where damage to the cells at the wound site causes symplastic Glu to leak to the apoplast where it triggers systemic response. We therefore targeted the genetically-encoded GFP-based Glu sensor iGluSnFR [5] to the cell wall of leaves using the chitinase signal sequence in order to visualize the apoplastic Glu level. Upon wounding, there was a local wave of increase in iGluSnFR signal at the cut region of the leaf that rapidly attenuated from the wound site. This spatial temporal Glu level in the apoplast is consistent with that of $[Ca^{2+}]_c$ at the cut region. In vivo calibration suggests that the apoplastic Glu reached 10-50 mM at the site of damage, a concentration that fits well with the estimates of symplastic Glu in the phloem. Taken together, when symplastic Glu is leaked from the damaged cells/tissues such as the phloem upon wounding, the GLR immediately triggers a Ca^{2+} signal propagating throughout the entire plant, activating systemic resistance responses in distal organs.

1. Nakai et al, Nature Biotechnology 19 (2001) 137-141.
2. DeFalco et al, Plant Cell Physiology 58 (2017)1173-1184.
3. Vincent et al, Plant Cell 29 (2017) 1460-1479.
4. Toyota et al, Science 361(2018) 1112-1115.
5. Marvin et al. Nature Methods 10 (2013) 162-170.

SB-2

doi: 10.1093/jmicro/dfz048

Acquisition of Large Volume EM Data Set and 3D Reconstruction with Automated Segmentation Application

Yoshiyuki Kubota[1,2]

[1] Division of Cerebral Circuitry, National Institute for Physiological Sciences, Okazaki, Japan,
[2]Department of Physiological Sciences, The Graduate University for Advanced Studies (SOKENDAI), Okazaki, Japan

An electron microscopy (EM)-based reconstruction of neuronal circuits from serial ultrathin sections method was introduced about 30 years ago[1]. It had been achieved all the steps manually: cutting the serial ultrathin sections using ultramicrotome, image capturing with transmission electron microscope (TEM), reconstruction using cardboard of the selected profiles of neural structures to provide impression of depth. Harris started using a computer software for the reconstruction to make it more efficient [2]. This technology had not been popular because of a high skill demand in electron microscopy, however, the reconstruction analysis method offered significantly valuable results. Therefore, it was introduced only in a limited number of laboratories where a good skill in serial ultrathin section method had been established. Then, we started to adapt new EM technologies such as focused ion beam-scanning electron microscopy (FIB-SEM), serial block-face electron microscopy (SBEM), automated tape-collecting ultramicrotomy (ATUM) with SEM, transmission electron microscope camera array (TEMCA) for the neural network analysis using the reconstruction method in early 2000. It has been modified and improved them vigorously[3] and a lot of noteworthy results were published in this decade[4-8]. EM volume data sets were getting larger year by year, and the volume size could be huge in size especially obtained with high-throughput EM system of either Multi-beam SEM or parallel processing with multiple single beam SEM systems.

The success of large volume EM acquisition using these new EM systems has created an issue, i.e., how to process large image data sets thus obtained. Soon it became obvious that it was difficult to handle large EM volume data sets using conventional 3D reconstruction image processing computer applications. To achieve segmentation easily and efficiently, automated segmentation computer applications have been developed[9] and used. Segmentation performance has increasingly been improved and reached to account for ~90% of the volume.

I would like to introduce our recent improvement for the segmentation of the large volume EM data set acquired with ATUM-SEM using the automated segmentation applications 'Flood Filling Network' [9] (Fig. 1). We found it works better for the EM data set with 30 nm thick sections than the one with 50 nm thick sections.

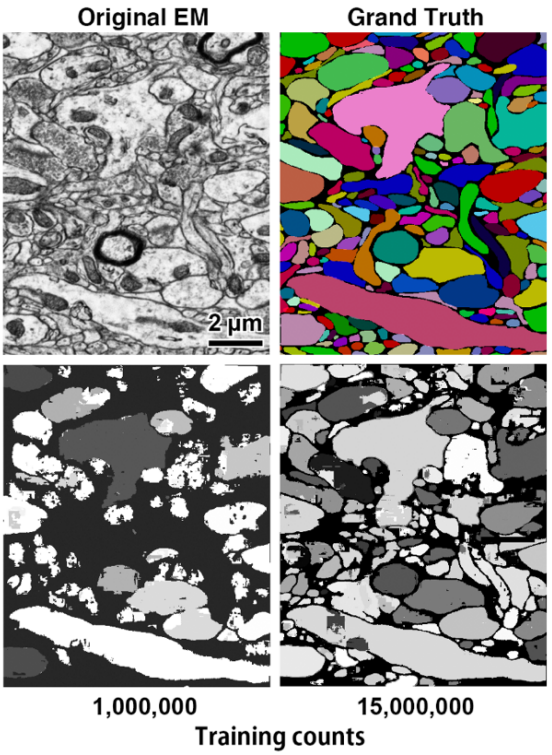

Fig. 1. Automated segmentation trials
An example trial of automated segmentation using machine learning computer application, flood filling networks.

1. White, E.L. and A. Keller, *J Comp Neurol*, **262**(1987):13-26.
2. Harris, K.M., et al., *J Neurosci*, **12**(1992):2685-705.
3. Kubota, Y., et al., *Front Neural Circuits*, **12**(2018): p. 98.
4. Bae, J.A., et al., *Cell*, **173**(2018): p. 1293-1306 e19.
5. Kasthuri, N., et al., *Cell*, **162**(2015): p. 648-61.
6. Lee, W.C., et al., *Nature*, **532**(2016): p. 370-4.
7. Schmidt, H., et al., *Nature*, **549**(2017): p. 469-475.
8. Takemura, S.Y., et al., *Elife*, 2017. **6**.
9. Januszewski, M., et al., *Nat Methods*, **15**(2018): p. 605-610.

SB-3 **doi: 10.1093/jmicro/dfz049**

Combining live imaging and single-cell whole gene expression analysis by developing an automated cell picking system

Katsuyuki Shiroguchi[1,2]

[1]RIKEN Center for Biosystems Dynamics Research (BDR), [2]RIKEN Center for Integrative Medical Sciences (IMS)

I had been working on single molecule observation for studying motor protein dynamics by setting up a modified optical microscope [1, 2]. I also developed a novel technology for whole gene expression analysis using a next generation sequencer [3, 4]. Based on these experiences for dynamics and genomics studies, we have been developing a single-cell picking system which enables additional analysis for observed cells under an optical microscope. Indeed, we performed single-cell RNA sequencing for observed cells, which links the dynamics behaviour and whole gene expression for individual cells. Now this system, including the cell picking and the library preparation for RNA sequencing, is automated, so that one may obtain the data in a high throughput manner. I will discuss our research direction, e.g., further integration with machine learning based on our automated system and our current biological targets.

1. Shiroguchi K., Kinosita Jr. K. Science 316 (2007) 1208-1212.
2. Shiroguchi K. et al, PLoS Biol. 9 (2011) e1001031.
3. Shiroguchi K. et al, PNAS 109 (2012) 1347-1352.
4. Ogawa T., et al, Sci. Rep. 7 (2017) 13576.

SB-4 **doi: 10.1093/jmicro/dfz050**

Semi-automatic organelle detection and recognition on electron microscopic images

Takumi Higaki[1]

[1]International Research Organization for Science and Technology, Kumamoto University, Kumamoto, Japan

Transmission electron microscopy (TEM) is a crucial technique to survey the nanolandscapes of intracellular structures. For successful TEM analyses, researchers must have advanced knowledge about various aspects of specimen preparation including sample fixation, resin embedding, ultrathin sectioning, and electron staining. Because these technical procedures affect the quality of the final images, TEM operators must be knowledgeable and experienced to acquire high quality images, and to interpret such images. For beginners, therefore, it can be difficult to analyse TEM images, for example, to label biological structures inside cells. Recent progress in TEM equipment and image processing techniques has enabled the acquisition of large-scale TEM image datasets. Analyses of images in such datasets can provide information about cellular changes on the tissue- and ultrastructural-levels. Large-scale TEM images are expected to be shared using a database system. Like other commonly used web mapping services, a searchable database of zoomable TEM images may allow researchers to explore the inside of cells in the near future. When establishing such a large-scale TEM image database, labelling or annotation of the intracellular structures is an essential step. Of course, TEM experts are able to complete this step, but it would be very laborious, and manual curation may not be sufficient to annotate all of the features in large image databases. Computer-assisted labelling would substantially lighten the load of TEM experts. In this context, we proposed that our biomedical image evaluation framework known as CARTA (Clustering-Aided Rapid Training Agent) [1, 2] might prove helpful for the semi-automatic detection of intracellular structures in large-scale TEM images [3]. CARTA, which comprises an active learning algorithm combined with a self-organizing map, was developed for bioimage classification. This framework is useful for combining and optimizing image feature selection techniques to classify biological features or structures in an image. In addition, it has been used to archive various types of biomedical images such as bright field and fluorescence microscopy images and magnetic resonance images, demonstrating its versatility.

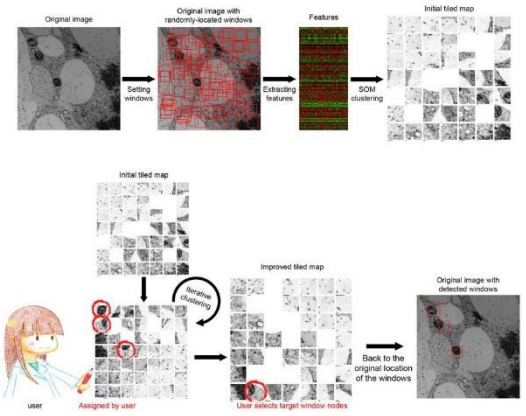

Fig. 1. Workflow for the proposed method

Here, we analysed TEM images of plant tissues, but similar biomedical images can be efficiently collected by the user-interactive system of CARTA. Organelles could be detected semi-automatically by analysing a collection of similar subdivided regions of TEM images. First, many square regions of interest, designated as 'windows' in this study, were placed at random locations covering the entire TEM image. The following procedures to collect similar windows are basically those laid out in the CARTA framework. An original set of 296 image features (KBI features) [1]. Then, cluster analyses of the windows in the self-organizing map (SOM) were performed based on the randomly selected features. The SOM serves as the interface for users to manually search for target organelles. The SOM summarizes the distribution of windows based on the features, and shows representative windows at the lattice node. Users can easily find the representative windows containing the targets without laborious visual inspection of the whole image. If there is insufficient representation of the target in the windows in the SOM, the user can improve the map by manually assigning targets. 'Feature combination' is automatically and optimally selected to improve the clustering results through iterative clustering. This process is repeated until the user is satisfied with the map. After interactive assignment and iterative clustering, the user can select the target window nodes in the map, thereby detecting targets (Fig. 1). Our proposed method accurately detected mitochondria, amyloplasts, chloroplasts, etioplasts, and Golgi stacks, indicating its broad utility to detect biological structures in TEM images. This method is ready for immediate use to reduce the amount of expert labour required for manual assignment of organelles and for quantitative evaluation of the changes in organelle distribution in large-scale TEM imaging studies.

1. N Kutsuna and T Higaki et al, (2012) Nature Communications 3: 1032.
2. T Higaki et al, (2014) Bioimages 22: 1-7.
3. T Higaki et al, (2015) Scientific Reports 5: 7794.

SB-5 **doi: 10.1093/jmicro/dfz051**

Abstraction of Pathological Information and Integration of Cancer Genome Information

Shumpei Ishikawa[1]

[1]Department of Preventive Medicine, Graduate School of Medicine, The University of Tokyo, Tokyo, Japan

Pathologists observed histology images using microscopes not only to diagnose the disease but also to find clues to understand the pathophysiology of the disease. However, since there was no way to objectively and quantitatively represent histological characteristics, there is no appropriate way to communicate it to others within the research / clinical community and to compare it quantitatively with other cases. Unlike these, genomic information can directly compare cases and accumulate and obtain new findings from thousands of cases such as Genome-wide Association Studies (GWAS), which has a strong impact on current biology and clinical sciences.

Recently, deep learning techniques, particularly convolutional neural networks (CNN), have been successfully applied to classification, detection, and segmentation of histopathology images. CNN outperforms human pathologists in terms of accuracy and diagnosis time for some applications[1-2]. While this approach is powerful, each task requires a task-specific feature extraction process. Therefore, building a trained network to cover all subjects in the histopathology field requires enormous computational power and hinders the widespread application of artificial intelligence among the pathology community. Therefore, an unsupervised feature extractor suitable for histopathology is required to express the morphology objectively and quantitatively. We have discovered that Deep Texture Representations (DTR) well-expresses cancer morphological information in unsupervised way and functions as a general-purpose encoder for cancer histology. DTR was applied to a large number of H & E stained histopathology images for content-based image retrieval (CBIR), that is, "search tool for histopathologically similar image from large datasets" [3]. Currently, manual browsing of histology atlas books is the primary method for most pathologists encountering unknown cases, so CBIR significantly reduces the time to correct diagnosis. Furthermore, through comprehensive quantitative comparison between cancer histopathology images and their driver gene mutations, we discovered many morphological features that correlate with cancer genome mutations, and predict mutation states with high accuracy using only H.E. images.

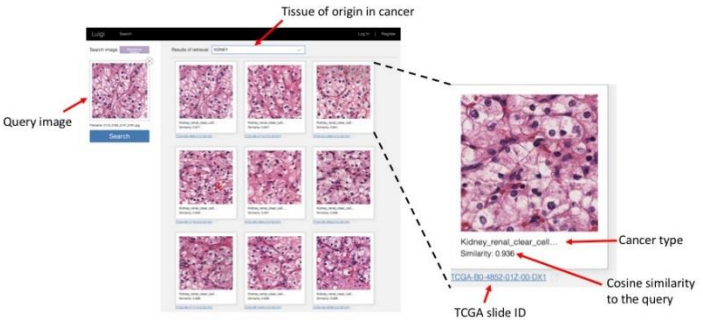

Fig. 1. Interface of content-based image retrieval (CBIR) systems for extracting "histopathologically similar" images using Deep Texture Representations (DTR) [3]

The deep texture representation (DTR) used in this study has several additional practical advantages: 1) applicable to relatively small datasets such as rare disease categories, 2) low computational cost will enable the quick decisions presented in this study. By obtaining a universal encoder of routinely used histology image, it becomes possible to directly collect, store, analyse, and query cases such as genomic information, which has a major impact on biomedical fields and global health.

1. Bejnordi, B. E. et al. JAMA 318(2017), 2199–2210 (2017)..
2. Nagpal, K. et al. npj Digital Medicine 2(2019), 48.
3.URL: https://luigi-pathology.com/

Special Sessions

Session of Kanto Regional Branch (K)

Sessions by JSM Academic Divisions (SS1, SS2)

Session of the Kazato Research Encouragement Prize (KA)

Luncheon Seminar (LS)

K-1 **doi: 10.1093/jmicro/dfz039**

Road to Electron Microscope Development.

Kurio Fukushima

STEM Corporation, Machida, Tokyo, Japan

In the 21st century, the performance of electron microscopes has improved, providing pico-scale-world imaging at the atomic and /or molecular level. However, it took an enormous amount of time that the microscopic device get such high performance.

The discovery of glass has led to the opening of a door of microscopic world. Glass manufacturing techniques have been developed around the Mesopotamia around 2000 BC, and various glass products have been made. At the beginning of the 9th century, Iraqi scientist Ibn al-Haitham worked on the research of the physical properties of light, and also studied the action of lenses. At the end of 12th century, British philosopher Roger Bacon published his research on the magnification of the lens in "Opus Majus". However, it took a little more time to be recognized the lens as a microscopic tool. In the 1590s, Dutch glasses craftsman Hans Janssen and his son, Zacharias Janssen, invented a first compound microscope which is combined objective lens and eyepiece. However, the magnification of this microscope was about 3 to 10 times, so the performance was not sufficient as a microscopic device. Half a century later, in 1662, British natural philosopher Robert Hooke developed a higher-performance compound microscope with a magnification of 50-60 times. Using this device, he observed microscopic structures of animals and plants in detail. "Micrographia", in which the results of his observation were summarized, was published in 1665. At the same era, Antony van Leeuwenhoek in Netherlands devoted himself to making a more powerful microscope. He was called a lens polish genius. His single-lens microscope with only one small glass ball lens, which were polished by hand carefully, having very short focal length, attained a higher magnification (200 to 300 times) than a double-lens microscope. Later, in the 19th century, achromatic lenses and plan lenses were developed. Using these lenses, the performance of the microscope was dramatically improved. At the end of the 19th century, a microscope that can observe fine structures at a magnification of 1000 times has been developed. Finally, the door to enter the micro-scale-world opened.

In the 1870s, British physicist Lord Rayleigh (John William Strutt, third Baron Rayleigh) and German physicist Ernst Karl Abbe respectively pointed out that the resolution of the optical microscope was limited to about half of the wavelength of the light used. Therefore, as long as visible light is used, the resolution is limited to about 200nm. To overcome this limitation, it was necessary to search another source with shorter wavelength, instead of visible light. At that time, various important inventions and discoveries related to the birth of electron microscope were made one after another.

1869; German physicist Johann Wilhelm Hittorf discovered cathode ray.
1897: British physicist JJ Thomson discovered the electron which is a component particle of cathode ray.
1897; German physicist Karl Ferdinand Braun developed Magnetic field deflection type cathode ray tube.
1903; German physicist Arthur Rudolph Berthold Wehnelt invented an internal deflection type cathode ray tube.
1924; French theoretical physicist Louis-Victor-Pierre-Raymond (7e duc de Broglie) advocated that electrons have both particle and wave properties.
1926; German physicist Hans Busch showed the possibility of making an electron lens through his research of electron trajectory in an axial electromagnetic field.
1927; British physicist Gábor Dénes invented a magnetic field lens consisted of an electromagnetic coil covered by iron.
1927-1928: It was found that electron has a very much shorter wavelength than visible light, and also its wavelength is inversely proportional to the acceleration voltage.

Under such historical background, Max Knol and Ernst August Friedrich Ruska, who aimed to improve the cathode-ray oscillograph under the professor Adolf Matthias of the Berlin Technical University, invented the electron microscope in 1931. The first electron micrograph taken by this device was a 16x metal mesh image. Its performance was much inferior to the performance of the optical microscope regrettably. Immediately after that the performance of the magnetic lens was improved, so that the performance of electron microscope increased dramatically. Observations at magnifications exceeding 10,000 times were achieved in 1933. And in 1939, together with Bodo von Borries and Ernst Ruska (Siemens and Halske GmbH) developed first commercial transmission electron microscope with a thermal electron gun. This microscope showed resolution of 7 nm. At last, the environment to step into the world of nano-scale has been prepared.

K-2

doi: 10.1093/jmicro/dfz040

Molecular-anatomical basis of synaptic circuit development in the cerebellum.

Masahiko Watanabe

Department of Anatomy, Faculty of Medicine, Hokkaido University, Sapporo, Japan

Excitatory synaptic circuits in cerebellar Purkinje cells (PCs) have two distinguished features, mono-innervation by climbing fiber (CF) and segregated CF/ parallel fiber (PF) territories. These features develop by three distinct mechanisms promoting input-selective synaptic adhesion, activity-dependent synapse refinement, and activity-dependent circuit plasticity [1]. The glutamate receptor GluD2-Cbln1 system promotes PF synapse formation and maintenance through Cbln1-mediated connection between GluD2-expressing PC spines and neurexin-expressing PF terminals [2-4].

The mGluR1 and P/Q-type Ca^{2+} channel, which mediate activity-dependent $[Ca^{2+}]_i$ rise upon PF and CF activation, respectively, play essential roles in synapse refinement by strengthening the innervation by single winner CFs and eliminating the innervation by surplus CFs on the PC soma and PF synapses on proximal dendrites [5-7]. Without either of the $[Ca^{2+}]_i$ rising mechanisms, immature PC circuitry in neonates, multiple CF innervation and unsegregated CF/PF territory, remains to the adulthood.

However, these $[Ca^{2+}]_i$ rise mechanisms are not sufficient to complete synapse refinement, and need the support by GLAST on Bergmann glia, a glutamate transporter preventing glutamate spillover and keeping the $[Glu]_e$ low. Such glutamate transporter function also promotes active circuits to expand and less active or inactive circuits to be suppressed [8]. Without GLAST, dendritic innervation by the ascending branch, a main synapse-forming CF branch, becomes regressive, whereas the transverse branch, a non-synapse forming silent branch, transforms into synapse-forming branches that innervate neighboring PCs.

Importantly, similar molecular mechanisms also control synaptic circuit development in the somatosensory cortex. mGluR5 and NMDA-type glutamate receptor function as $[Ca^{2+}]_i$ rising mechanisms for barrel formation through activity-dependent strengthening and elimination of thalamocortical inputs. GLT1, a glutamate transporter in cortical astrocytes, regulates lesion-induced critical period plasticity, and promotes shrinkage of lesioned barrels and expansion of intact barrels in the neighbor. Therefore, these glutamatergic signalling systems work in concert to refine synaptic circuitry in both the cerebellum and cerebrum.

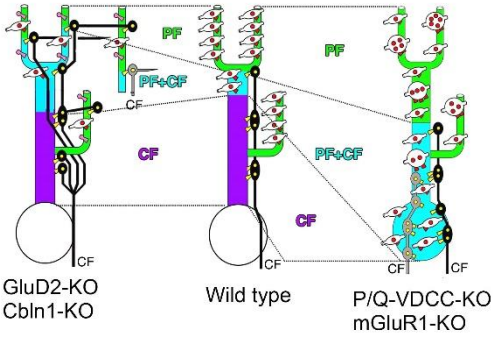

Fig. 1. Contrasting circuit phenotype between mutant mice lacking synapse adhesion molecules (GluD2 and Cbln1) and mutant mice lacking Ca^{2+} rising mechanisms (P/Q-VDCC and mGluR1).

1. M Watanabe and M Kano, Eur J Neurosci, 34 (2011) 1697-1710.
2. H Kurihara et al., J Neurosci 17 (1997) 9613-9623.
3. R Ichikawa et al., J Neurosci 22 (2002) 8487-8503.
4. K Matsuda et al., Science 328 (2010) 363-368..
5. T Miyazaki et al., J Neurosci 24 (2004) 1734-1743.
6. T Miyazaki et al., J Neurosci 32 (2012) 1311-1328.
7. R Ichikawa et al., . Proc Natl Acad Sci, U.S.A. 113 (2016) 2282-2287.
8. T Miyazaki et al., Proc Natl Acad Sci, U.S.A. 114 (2017) 7438-7443.

K-3 **doi: 10.1093/jmicro/dfz041**

Scanning electron microscopy and scanning probe microscopy for visualizing the three-dimensional structure of cells and tissues.

Tatsuo Ushiki

Division of Microscopic Anatomy, Niigata University Graduate School of Medical and Dental Sciences, Niigata, Japan.

Our laboratory specializes in analyzing the three-dimensional structure of cells and tissues in relation to their function. In this context, we have been interested in application of scanning electron microscopy (SEM) and scanning probe microscopy (SPM) to biological studies. In this paper, I briefly introduce these two techniques and show our data obtained by them.

1. Scanning electron microscopy (SEM)
This microscope scans a focused electron beam over a sample surface to create images by collecting signals (e.g., secondary electron, SE) generated by electron-sample interactions. Because it is necessary to keep the inside of the conventional SEM in a vacuum, samples to be observed are generally dried by a special method (i.e., critical point drying or freeze drying), and coated with metal. The development of various sample preparation techniques including a KOH-collagenase treatment enabled the direct visualization of complex tissue structures three-dimensionally by SEM [1].

Recent advances in microscopy also provided us the specialized SEM that allows sample observation at atmospheric pressure, resulting in the observation of live tissues in a wet state [2].

On the other hand, it has become possible to observe a section of a plastic-embedded tissue specimen by SEM, in the same manner as by conventional transmission electron microscopy [3]. Collection of serial section images by SEM followed by their 3D reconstruction on a computer is expected to be used for analyzing the three-dimensional structure of various cells and tissues [4].

2. Scanning probe microscopy (SPM)
Since the invention of scanning tunneling microscopy (STM), a variety of microscopes have been developed that can image the sample surface topography by scanning a probing tip close to the sample surface. These are collectively called scanning probe microscopes (SPMs). Among them, the atomic force microscope (AFM) has been widely used in biological fields [5]. Recently, we have been interested in application of the scanning ion conductance microscope (SICM) to the biological field [6]. In this microscope, a micro-glass-pipette with an electrode is used as a probe for obtaining an ion current generated between a pipette electrode and bath electrode. Our studies revealed that SICM can image the three-dimensional structure of cells and tissues in a liquid. We also showed that the quality of these images are comparable to that of SEM images [7].

1. T Ushiki and C Ide, Arch Histol Cytol 51 (1988) 223-232.
2. Y Ominami et al, Microscopy 64 (2015) 97-104
3. D Koga et al, Microscopy 64 (2015) 387-394
4. D Koga et al, Microscopy 65 (2016) 145-157
5. T Ushiki and K Kawabata in “Applied Scanning Probe Methods X. Biomimetics and industria applications”, ed. B Bhushan et al, Springer, Heidelberg (2008) 285-308.
6. T Ushiki et al, Micron 43 (2012) 1390-1398
7. M Nakajima et al., Semin Cell Dev Biol 73 (2018) 125-131.

K-4 **doi: 10.1093/jmicro/dfz042**

Current Status of Crystal Structure Analysis using Scanning Transmission Electron Microscopy

Koji Kimoto[1], Jun Kikkawa[1], Ovidiu Cretu[1] Keiichi Yanagisawa[1] and Kazuo Ishizuka[2]

[1]National Institute for Materials Science (NIMS), Tsukuba, Japan. [2]HREM Research Inc. Higashimatsuyama, Japan.

Annular dark-field (ADF) imaging [1] allows us to analyse crystal structures using incoherent imaging approximation. Quantitative ADF imaging has been reported [2], in which the ADF intensity is normalized by the incident probe intensity. We found the nonlinear response of conventional ADF imaging system becomes critical [3] in high sensitivity measurements, and we demonstrated a quantitative ADF imaging, in which the number of electrons at each pixel was evaluated. We also estimated effective source distribution using a high-resolution ADF image of a monolayer graphene (Fig. 1) [4]. Because the number of electrons was measured, the quantum noise of the ADF images was estimated, which became a guideline to assess the difference between experiment and simulation.

The precision of the ADF imaging suffers a low ADF signal. The ADF signal from a monolayer graphene is only several electrons per pixel under a typical experimental condition; e.g., probe current of 30 pA, ADF inner angle of 50 mrad, and 0.04 ms of dwell time. We observed multiple ADF images with short dwell time to minimize an image distortion due to image drifts [5]. We prepared DigitalMicrograph script to track the specimen drift during multiple image acquisitions, resulting in a high precision of several picometers in atomic position analysis [6]. Dynamical scattering or crystal tilt are problematic even in the case of ADF imaging [6], which suggests the limit of the incoherent imaging approximation.

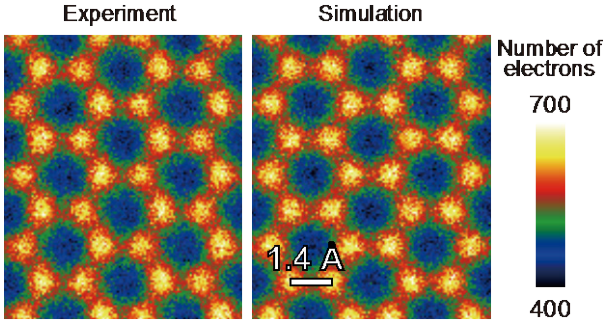

Fig. 1 Quantitative ADF imaging of monolayer graphene observed at 80 kV. Simulation includes residual aberrations, defocus spread and an effective source distribution, and the quantum noise is added on the basis of the Poisson distribution.

The reproducibility of ADF imaging depends on various experimental parameters, including aberrations of the objective lens. The ADF image of a monolayer graphene shows small systematic deviation from the simulation, and we recognized the time-dependent low-order aberrations are a barrier for further quantitative analyses. We proposed a method to measure low-order aberrations using two Ronchigrams of unknown crystalline specimen [7]. Fourier transforms of two Ronchigrams observed under different foci were used to measure the aberration, such as defocus, two-fold astigmatism, coma and three-fold astigmatism. Figure 2 shows an example of aberration measurement, in which the high stability of defocus C_1 and two-fold astigmatism A_1 of less than 1 nm per minute is demonstrated.

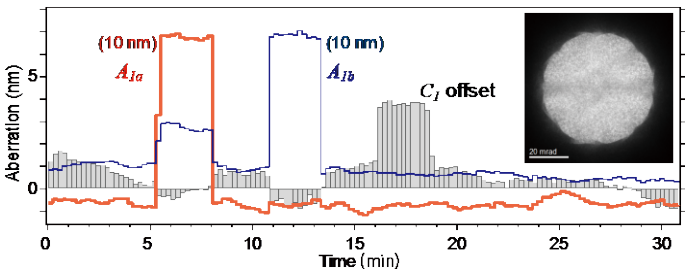

Fig 2. Time dependence of defocus C_1 and two-fold astigmatism A_1 as measured using our method [7]. A specimen was a $SrTiO_3$ (001) film and the inset shows an experimental Ronchigram.

The recent progress in the instrumentation of 4D-STEM allows us to apply it for crystal structure analyses, which was a time-consuming approach in the conventional instrument [8]. The crystal structure analysis using ADF imaging becomes more practical using fast 4D-STEM instrumentation.

1. S.J. Pennycook and D.E. Jesson, Ultramicroscopy 37 (1991) 14-38.
2. J.M. LeBeau, et al., Physical Review B 80 (2009)
3. S. Yamashita, et al., Microscopy 64 (2015) 143-150.
4. S. Yamashita, et al., Microscopy 64 (2015) 409-418.
5. K. Kimoto, et al., in: Proceedings of IMC16, Sapporo, 2006, p. 609.
6. K. Kimoto, et al., Ultramicroscopy 110 (2010) 778-782.
7. K. Kimoto and K. Ishizuka, Ultramicroscopy 180 (2017) 59-65.
8. K. Kimoto and K. Ishizuka, Ultramicroscopy 111 (2011) 1111-1116.

SS1-1 **doi: 10.1093/jmicro/dfz062**

Single-Cell Innate Fluorescence Analysis by Confocal Microspectroscopy.

Yutaka Yawata[1,2]、Kyosuke Takabe[1]、Nobuhiko Nomura[1,2]

[1]Faculty of Life and Environmental Sciences, University of Tsukuba, Tsukuba, Japan
[2]Microbiology Research Center for Sustainability, University of Tsukuba, Tsukuba, Japan

The advent of new microscale technologies such as microfluidics and most recently microfluidic robotics offers unprecedented opportunities to manipulate environmental conditions over length scales relevant to bacterial transport and on time scales short enough to resolve bacterial responses to rapid shift in a surrounding condition. These approaches are enabling controlled ecological studies of environmental bacteria that account for fundamental characteristics of natural microbial habitats, and are shedding light on the ecological principals underpinning the dynamic microbial consortiums that are the fundamental driver of global element cycles. On the other hand, emerging non-invasive technologies are revolutionizing our notion of cell analysis, by allowing a microbiologist to interrogate live and intact cell about its physiological status and taxonomy without affecting cellular physiology and integrity.

In this lecture, I argue the potential of a novel single-cell innate fluorescence signature analysis technology to expand the scope of controlled ecological studies of live and intact environmental microbes, to bring about new insights into the complex microbial life in the nature. A cell's innate fluorescence signature is an assemblage of fluorescence signals emitted by diverse bio-molecules within a cell. It is known that the innate fluoresce signature reflects various cellular properties and physiological statuses, thus they can serve as a rich source of information in cell characterization as well as cell identification. However, conventional techniques focus on the analysis of the innate fluorescence signatures at the population-level, but not at the single-cell level, and thus necessitates a clonal culture.

We have recently developed a minimally invasive method (confocal reflection microscopy-assisted single-cell innate fluorescence analysis: CRIF)[1] to optically extract and catalogue the innate cellular fluorescence signature from each individual live microbial cell in a three-dimensional space. Using a range of model organisms, we demonstrate that machine learning models can be trained with a single-cell innate fluorescence signature dataset to classify cells according to their type and physiological status, for example distinguishing a wild type Aspergillus nidulans cells from its nitrogen metabolism mutant counterpart, and log phase Pseudomonas putida cells from stationary phase cells. Since the fluorescence signature is an innate property of a cell, our technique allows the use of a "virtual" label that signifies the type or physiological status of intact and tag-free cells, within a cell population distributed in a three-dimensional space. We suggest that the single-cell autofluoresce signature analysis is a promising tool to directly assess the taxonomical or physiological heterogeneity within a microbial population.

1. Yawata Y, Kiyokawa T, Kawamura Y, Hirayama T, Takabe K and Nomura N. 2019. Intra- and interspecies variability of single-cell innate fluorescence signature of microbial cell. Appl Environ Microbiol 85:e00608-19

SS1-2 **doi: 10.1093/jmicro/dfz063**

High Resolution Dynamic Imaging of Living Bacterial Cell Membrane Molecules by High Speed AFM

Hayato Yamashita[1],

[1]Center for Science and Technology under Extreme Conditions, Graduate school of engineering science, Osaka University, Osaka, Japan

Progresses in microscopic techniques have ever contributed to many discoveries in cell biology. Electron microscopic techniques have revealed that cell membrane structures are organized into functional domains, whereas optical microscopic techniques such as fluorescence imaging have revealed the dynamics of specific molecules in live cell membrane. However, neither technique can directly and simultaneously visualize the structure and dynamics of living cell surface at high spatiotemporal resolution.

Atomic force microscopy (AFM) is a unique technique that has been used to visualize label-free biological samples at sub-nanometer resolution under physiological conditions. Recent advances in AFM provide new opportunities to investigate single cells and single molecules in microbiology [1]. Especially, visualization of a living cell architecture is a novel powerful approach to reveal the molecular organization in vivo. On the other hand, the time resolution of conventional AFM is not sufficient to capture the dynamic biological processes. Therefore, visualization of the molecular dynamics in living cells using AFM has not been achieved.

High speed atomic force microscopy (HS-AFM) was developed to visualize the dynamic molecular process at high resolution in physiological condition [2]. This microscopy has been succeeded in capturing the single molecular functioning processes for many kinds of biological molecules [3]. However, most of them were observation results for proteins purified from cell, and the molecular imaging for living cell were only a few [4][5]. We have ever investigated the surface structure of living bacterial cell using HS-AFM. HS-AFM images of the live cell surface showed that the outer membrane of gram-negative bacteria is covered by a net-like structure, and the movies captured by HS-AFM revealed dynamic movements of outer membrane proteins (Fig. 1). Recently, we developed HS-AFM scanner for molecular imaging at higher spatiotemporal resolution on live cell surface. We applied this technique for observing some kinds of gram-negative bacterial cell. High resolution HS-AFM images revealed molecular arrangement of outer membrane protein porin trimers and the dynamic processes on bacterial cell outer membrane. Furthermore, we observed the reaction processes on cell surface for antimicrobial agent. These investigations using new technique will lead to elucidate the molecular organization in bacterial cell membrane.

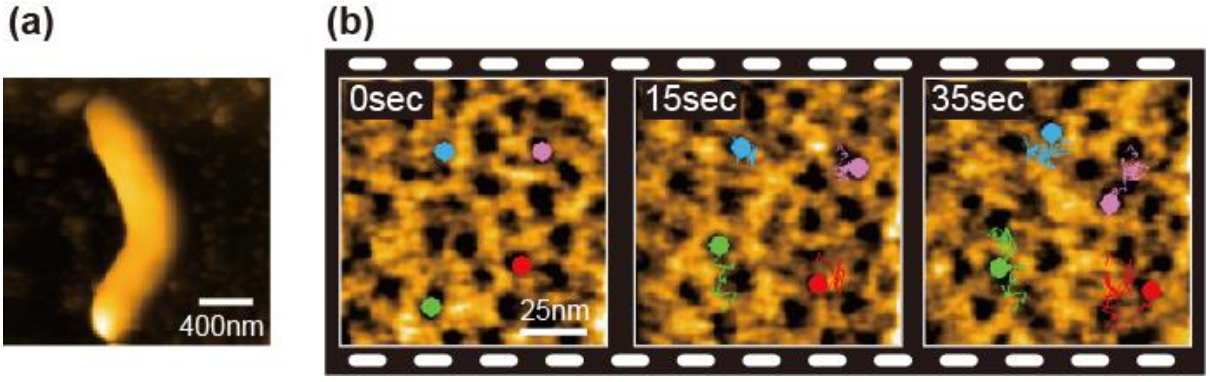

Fig. 1. High speed AFM observation of bacterial cell (a) High speed AFM image of single bacterial cell (b) High speed AFM images of dynamic process in cell surface structure at nanometer-scale. These figures show snapshots of high speed AFM images captured at 0.5sec/frame. In these images, four trajectories were drawn by tracing the movement of diffusing hole structure.

1. Y. F. Dufrêne, Nat. Rev. Microbiol. 6 (2008) 674–680.
2. T. Ando et al, Proc. Natl. Acad. Sci. USA 98 (2001) 12468−12472.
3. T Ando et al, Chem. Rev. 114 (2014) 3120−3188.
4. H.Yamashita et al, J. Mol. Biol. 422 (2012) 300-309.
5. Z. Oestreicher et al, Micron 72 (2015) 8-14.

SS1-3 **doi: 10.1093/jmicro/dfz064**

Internal Ribbon Structure Driving Helicity-Switching Swimming of *Spiroplasma*

Yuya Sasajima[1], Takayuki Kato[2], Tomoko Miyata[2], Keiichi Namba[2,3] and Makoto Miyata[1,4]

[1]Grad. Sch. Sci., Osaka City Univ., Japan, [2]Grad. Sch. Frontier Biosci., Osaka Univ., Japan, [3]RIKEN BDR & SPring-8 Center, Japan and [4]OCARINA, Osaka City Univ., Japan

Spiroplasma eriocheiris, a crustacean pathogen, is a helical-shaped swimming bacterium without a peptidoglycan layer. It swims in a high viscosity solution by switching the cell helicity from front to back. This swimming motility is driven by a unique intracellular structure, unlike the well-known bacterial flagellar motility [1, 2, 3]. In this study, we analyzed the internal helical ribbon structure by electron microscopy to elucidate the mechanism of helicity switching.

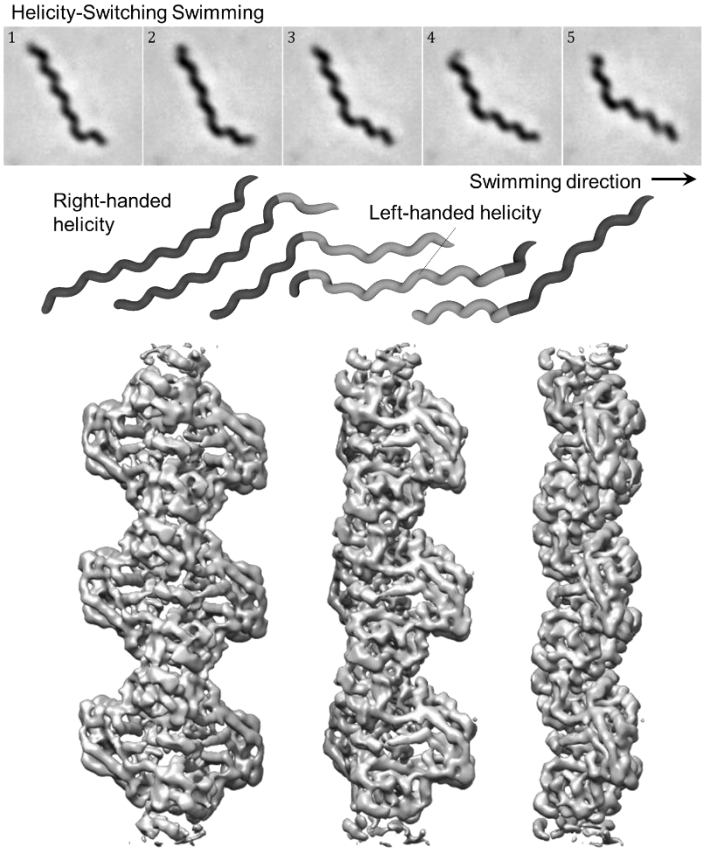

Fig. 1. Helicity-switching swimming of Spiroplasma and Fibril filament

Optical microscopy of swimming cells revealed that the cells form a helical shape with a half pitch of about 350 nm. We isolated the internal helical ribbon structure by density gradient centrifugation and analyzed it by mass spectrometry. The ribbon was composed by bacterial actin MreB and *Spiroplasma* specific fibril protein. Negative staining and quick freeze, deep etch replica electron microscopy visualized that the ribbon structure has a 350-nm half pitch. The protofilament obtained by disassembling the isolated ribbon structure was a double helix consisting of paired fibril filament. The half pitch of the protofilament corresponded to those of the cell helicity and the internal ribbon structure. The structure of the fibril filament was revealed at 4Å resolution by electron cryomicroscopy and single particle analysis. The single-stranded fibril filament is formed by repeat of fibril dimers. The fibril filament has a left-handed long-pitch helicity, which is consistent with the 350-nm half pitch of the protofilament. These results show that the conformational change of fibril protein switches the helicity from the cell front to the rear end. When swimming cells were treated with MreB polymerization inhibitor A22, the cells stopped the helicity switching and the intracellular ribbon structure was disassembled into protofilaments, suggesting that the physical interaction between MreB and fibril protein is essential for swimming. Based on these results, we propose a model for the helicity switching in *Spiroplasma* swimming.

1. Miyata M and Hamaguchi T (2016) Integrated information and prospects for gliding mechanism of the pathogenic bacterium *Mycoplasma pneumoniae*. Frontiers in Microbiology 7, 960.
2. Liu P, Zheng H, Meng Q, Terahara N, Gu W, Wang S, Zhao G, Nakane D, Wang W and Miyata M (2017) Chemotaxis without conventional two-component system, based on cell polarity and aerobic conditions in helicity-switching swimming of *Spiroplasma eriocheiris*. Frontiers in Microbiology. 8, 58.
3. Terahara N, Tulum I and Miyata M (2017) Transformation of crustacean pathogenic bacterium *Spiroplasma eriocheiris* and expression of yellow fluorescent protein. Biochemical and Biophysical Research Communication. 487, 488-93.

SS1-4 **doi: 10.1093/jmicro/dfz065**

3D reconstruction of intracytoplasmic membrane structure of methane-oxidizing bacteria by electron microscopy imaging

Katsuyuki Uematsu[1], Chong Chen[2] and Hisako Hirayama[2]

[1]Marine Works Japan LTD, Yokosuka, Japan, [2]X-STAR, Japan Agency for Marine-Earth Science and Technology (JAMSTEC), Yokosuka, Japan

Methane is a greenhouse gas with major contributions to the ongoing climate change. It is produced all over the world anthropogenically (e.g., livestock, fossil fuel), and the management of methane emission is an important task for mankind in the coming decades. Methane-oxidizing bacteria grow using methane as the energy and carbon source, and is thus expected to play a major role in controlling methane emissions.

Morphological analyses of methane-oxidizing bacteria have been conducted using TEM, showing that most of them have an intracytoplasmic membrane (ICM) structure embedded with methane monooxygenase catalyzing oxidation of methane to methanol. Most of known methane-oxidizing bacteria phylogenetically belong to either of two classes, *Gammaproteobacteria* or *Alphaproteobacteria*. Gammaproteobacterial species typically exhibit bundles of ICMs distributed throughout the cell, while alphaproteobacterial species show ICMs arranged along the cell periphery. However, traditional TEM analysis was unable to clarify the 3D structure and distribution of the ICMs, or how it connects with the cell membrane.

Methane oxidizing bacteria in the genus *Methylobacter* of the *Gammaproteobacteria* are known to occur across terrestrial and marine habitats. *Methylobacter marinus* MR1, isolated from subsurface sediment cores drilled from 0.4-106 meter below the seafloor 80 km offshore Shimokita Peninsula, Japan, grows well at room temperature with a high cell yield. This is ideal for carrying out various studies in order to reveal the physiological properties of methane oxidizing bacteria, and therefore it was selected as the target of our study.

In order to elucidate the 3D structure of the ICMs within the cell, cultured MR1 cells were subjected to high pressure freezing and freeze substitution technique during sample preparation which greatly reduce structural changes. Serial cross-sectional images were acquired by FIB / SEM (Helios G4 UX) through slice-and-view. Furthermore, a thick section was taken from the same block to obtain tilting images by STEM tomography (Tecnai 20) to shed light on the ultra-structure of the ICMs. For both image stacks, the specialist software Amira was used to reconstruct the ICMs in 3D.

In this presentation, we will display and discuss the 3D reconstructions of the ICMs, showing the distributions of the ICM structures in the cell, as well as a 3D model of its microstructure. Our results show that the ICMs were found in a large number of bundles, corresponding to ribosome-free regions, distributed predominantly at the cell periphery. Multiple ICM structures were seen in each bubdle and the directionality of these were constant within each bundle but not among bundles. In addition, our 3D reconstructions indicate that the multiple ICM structures seen in each bundle are not different cross-sections of a single folded membrane layer, but instead each structure represents independent, closed, flattened pocket with thickness of 20 to 30 nm and stacked at similar intervals. Our results suggest that the ICM is probably not continuous with the so-called cell membrane.

SS2-1 **doi: 10.1093/jmicro/dfz066**

Scanning probe microscopy and its biomedical application – from the historical viewpoint.

Tatsuo Ushiki

Division of Microscopic Anatomy, Niigata University Graduate School of Medical and Dental Sciences, Niigata, Japan.

Our laboratory specializes in analyzing the three-dimensional structure of cells and tissues in relation to their function. In this context, we have been interested in application of scanning electron microscopy (SEM) and scanning probe microscopy (SPM) to biological studies. In this paper, I briefly introduce these two techniques and show our data obtained by them.

Various kinds of microscope using a probing tip have been introduced since the scanning tunneling microscope (STM) was invented by Binnig and Roher in 1981 [1]. These microscopes have no lens but scan a sharp probing tip over a solid sample while monitoring the physical properties between the tip and sample surface. Thus, they are generally referred to as scanning probe microscopes (SPM). Among them, the STM is the first to be applied to the biological fields. However, the biological applications of the STM have been limited to the observations of biomolecules such as deoxyribonucleic acid (DNA), because the samples for STM are needed to be electrically conductive. In contrast with the STM, the atomic force microscope (AFM) invented in 1986 [2] has been widely applied to the studies on the surface morphology in biological fields, because this microscope can create topographic images of both conductive and non-conductive samples at high resolution from the micrometer scale to the atomic scale [3]. Furthermore, high-speed atomic force microscopy (HS-AFM) can directly visualize protein molecules during their functional activity at high spatiotemporal resolution, without a marker being attached to the molecules [4].

On the other hand, other investigators have been interested in the AFM application to the study of the physical properties of biological samples, because this microscope can measure the interaction forces between the tip and sample. In this context, AFM has been used not only for measuring the elasticity of single surface molecules in relation with function, but also for measuring the physical properties of the sample surface including surface changes, adhesion and elasticity of cells [5, 6].

Scanning ion conductance microscopy (SICM), introduced in 1989 [7], has been also applied to imaging of biological samples in liquid conditions [8]. This technique uses a glass micropipette as a sensitive probe, which contains electrode and is filled with an electrolyte solution. Because the pipette-sample distance is controlled by detecting the ion current that flows between the electrode in the micropipette and a bath electrode, this technique allows force-free topographic imaging of soft samples under liquid conditions. Introduction of hopping mode SICM has further expanded the applicable range of imaging of biological samples [9]. Thus, SICM has been especially applied to studies of biological samples, such as collagen fibrils, chromosomes, cultivated cells and tissue blocks [10, 11]. Although AFM provides better resolution than SICM in some samples, only the latter can obtain contact-free images of soft samples with complicated shapes. Although its time resolution is still limited, this technique is also expected to be useful in the field of cell and tissue research.

1. G Binnig and H Rohrer, Helv Phys Acta 55 (1982) 726-735.
2. G Binnig et al, Phys Rev Lett. 56 (1986) 930-933.
3. AD Ozkan et al, Semin Cell Dev Biol 73 (2018) 153-164.
4. T Ando, Curr Opin Chem Biol 51 (2019) 105-112.
5. T Ushiki and K Kawabata in “Applied Scanning Probe Methods X. Biomimetics and industria applications”, ed. B Bhushan et al, Springer, Heidelberg (2008) 285-308.
6. F Braet and DJ Taatjes, Semin Cell Dev Biol 73 (2018) 1-3.
7. PK Hansma et al, Science 243 (1989) 641-643.
8. YE Korchev et al, Biophys J 73 (1997) 653-658.
9. P Novak et al, Nat Methods 6 (2009) 279-281.
10. T Ushiki et al, Micron 43 (2012) 1390-1398
11. M Nakajima et al., Semin Cell Dev Biol 73 (2018) 125-131.

SS2-2 **doi: 10.1093/jmicro/dfz067**

Frontiers of AFM imaging method –high-resolution AFM in liquids and subsurface imaging–

Hirofumi Yamada[1], Kei Kobayashi[1]

[1]Department of Electronic Sci. & Eng., Kyoto University, Kyoto, 615-8510, Japan

Atomic force microscopy (AFM) has been widely applied to the broad areas in surface science as a nondestructive, high-resolution imaging method. In particular, significant progress has been made in frequency modulation AFM (FM-AFM) in liquids over the past decade [1, 2]. The technique is widely used for the direct investigation of solid-liquid interfaces as well as "in vivo" molecular scale biological processes. Force mapping method based on FM-AFM has also been developed as a powerful technique for high-resolution studies of interaction forces on a specific molecule. Here we show the present status of high-resolution imaging of a wide variety of biomolecules and molecular-scale investigations of interaction forces at solid-liquid interfaces, related to hydration structures and electric double layers (EDLs). Furthermore, we present the visualization of subsurface nanostructures based on the AFM nanomechanical measurement, expected to be novel nanometer-scale tomography.

Biomolecules working as nanoscale complex systems such as various proteins play essential roles in a wide variety of biofunctions. Investigations of molecular-scale structures and interactions of the biomolecules are significantly crucial for understanding the complex biofunctions. FM-AFM is a powerful technique, which is capable of atomic-scale imaging of a wide variety of material surfaces even in liquid environments. In addition, since three-dimensional (3D) force mapping method based on FM-AFM has been developed to analyze the 3D nanoscopic space over a sample surface, the method allows us to visualize the hydration structures and the electric double layers at the solid-liquid interface [3, 4]. In this study our recent, successful results on high-resolution FM-AFM imaging of biomolecules in physiological environments are presented, as shown in Fig. 1. The molecular-scale surface charge density distribution of DNA and specific interaction forces between ligand-protein molecules investigated by 3D force mapping method are also described [5]. In fact the obatined force map of a DNA molecule deposited on a poly-L-lysine (PLL) film clearly showed the attractive force on the PLL film and the repulsive force on DNA, reflecting the charges of the PLL film and DNA, each having positive amino groups and negative phosphate groups, respectively.

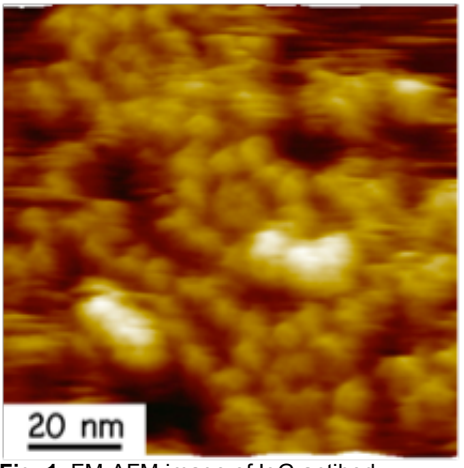

Fig. 1. FM-AFM image of IgG antibody hexamer binding to its antigenic molecules appeared as bright spots.

Non-invasive imaging of subsurface nanostructures based on atomic force microscopy has recently gained much attention for its wide variety of potential applications in many scientific and engineering fields. We have revealed that there existed a strong correlation between subsurface nano structures and surface stiffness in the previous studies [6, 7]. Furthermore, we developed a novel, powerful method allowing us to visualize subsurface nanostructures with a nanometer-scale spatial resolution [8]. The technique is referred to as scanning thermal noise microscopy (STNM). However, whether or not subsurface signal obtained by STNM includes quantitative information on depth has not been clarified yet. In this study new test samples for quantitative e subsurface imaging have been fabricated. The sample is a photopolymer film having polystyrene(PS) nanoparticles inside located a designed distance from the polymer surface.

1. S. Ido, K. Kimura et al., ACS Nano 7 (2013) 1817-1822.
2. S. Ido, H. Kimiya, H. Yamada et al., Nature Materials, 13 (2013) 264-270.
3. K. Umeda, K. Kobayashi et al., Nanotechnology, 26 (2015) 285103(1-9).
4. K. Umeda, L. Zivanovic et al., Nature Communications 8 (2017) 2111(1-9).
5. H. Kominami, K. Kobayashi, H. Yamada, Scientific Reports 9, (2019) 6851(1-7).
6. K. Kimura, K. Kobayashi et al., Ultramicroscopy 133 (2013) 41-49.
7. K. Kimura, K. Kobayashi et al. Nanotechnology 27 (2016) 415707(1-9).
8. A. Yao, K. Kobayashi et al., Scientific Reports 7 (2017) 42718(1-8).

SS2-3 **doi: 10.1093/jmicro/dfz068**

Frontier of Low-Temperature Scanning Tunnelling Microscopy and Future Perspective

Katsuya Iwaya

UNISOKU Co., Ltd., Osaka, Japan

Since the invention of scanning tunnelling microscope (STM) in 1982, this experimental technique has been increasingly applied to a wide range of research fields. In particular, STM is recognized as a powerful tool to study various physical phenomena occurring at low temperatures due to unique capabilities of combining topographic imaging with atomic-scale spatial resolution and spectroscopic imaging with high energy resolution. In this talk, recent research topics studied using low temperature STMs are briefly reviewed as selected below and lastly future prospects for this technique foreseen from the recent trend will be discussed.

Identifying Majorana fermions in topological superconductors is one of key issues in the low temperature STM research field. Since Majorana fermions are expected to exist at edge states and vortex cores, low temperature STM can play a decisive role for this purpose. Many claims have been constantly reported but distinguishing between Majorana and ordinary quasiparticle bound states in a vortex core remained unclear because the measurement temperature was not sufficiently low. Machida et al. recently developed a dilution-refrigerator based STM working below 90 mK and successfully identified the difference between Majorana and ordinary quasiparticle bound states in a vortex core [1]. This study will initiate researchers to pursue STM measurements at ultra-low temperature.

Twisted bilayer graphene is a new stimulating topic because the electronic correlation can be tuned by the rotational angle between two stacking graphene sheets and at a specific angle ($\theta \sim 1.1^\circ$) where the electronic correlation is greatly enhanced, a similar phase diagram as high temperature superconductors is discovered by tuning the chemical potential using a gate voltage [2]. Although the sample preparation was challenging for STM measurements, several groups successfully revealed direct evidences of unusual strong electron-electron interactions as a function of carrier density [3,4,5]. STM measurements at lower temperatures below a superconducting transition temperature ($T_c \sim 1$ K) are expected to be conducted in the near future.

Combining STM with optical techniques is another active field and enables us to resolve various optical phenomena with nanometer-scale spatial precision. For instance, tip-enhanced Raman spectroscopy with sub-molecular spatial resolution has been recently used to detect molecular vibrations as a finger-print for chemical identification [6]. Scanning tunnelling luminescence spectroscopy can visualize fundamental optical properties including emission and absorption spectra of a single molecule and the energy transfer between two molecules [7]. Time-resolved STM realized by the combination of STM and the optical pump-probe technique makes it possible to explore ultrafast transient carrier and spin dynamics of various functional materials [8].

Considering the recent trend including the topics described above, it is reasonable to expect that ultra-low temperature STM combined with superconducting (vector) magnets applicable for thin film samples with gating will play an important role in the condensed matter physics. The combination of STM and the optical techniques will be further advanced and recently developed systems such as THz-STM and time-resolved scanning multiprobe systems will be available for low temperature measurements in the near future. Another future direction of the instrumental development demanded from the market is a cryogen-free system because of the recent world-wide shortage of helium. Such cryogen-free systems are commercially available but the base temperatures of those systems are relatively high and the vibration noise level needs to be further suppressed. Thus, a highly stable cryogen-free STM working at a lower temperature is expected to be available and might become a standard system in the future, if successfully developed.

1. T Machida et al., Nat. Mater. 18 (2019) 811-816.
2. Y Cao et al. Nature 556 (2019) 43-50.
3. Y Xie et al. Nature 572 (2019) 101-105.
4. A Kerelsky et al. Nature 572 (2019) 95-100.
5. Y Jiang et al. Nature 572 (2019) 215-219.
6. R Zhang et al. Nature 498 (2013) 82-86.
7. H Imada et al. Nature 538 (2016) 364-367.
8. Y Terada et al. Nat. Photon. 4 (2010) 869-879.

SS2-4 doi: 10.1093/jmicro/dfz069

High resolution infrared imaging of composite materials

Hiroshi Itoh[1], Hiroko Hiramoto[1], Akinori Honda[1], Koji Ishida[1], Noriko Yamazaki[2], Koichi Hasegawa[3] and Kiyoka Takagi[3]

[1] National Institute of Advanced Industrial Science and Technology, Research Institute for Measurement and Analytical Instrumentation, Tokyo, Japan, [2] Mitsubishi Heavy Industries, ltd., Kanagawa, Japan and [3] Mitsubishi Heavy Industries, ltd., Aichi, Japan

There are many efforts to identify chemical states with scanning probe microscope (SPM), such as force spectroscopy, inelastic tunnelling current spectroscopy, and optical spectroscopy. Fourier transform infrared (IR) spectroscopy (FTIR) with SPM is one of the possible optical technique to separate chemical information on the surface. Nano FTIR method is the technique to measure the infrared spectrum, which is synchronized with tapping frequency of the SPM cantilever. As a result, high resolution local spectrum, which is equivalent to probe radius of tip apex, can be obtained. This technique was used to analyse chemical information of composite material interface. Cross-section of adhesive resin was prepared by polishing with alumina powder. Fig. 1 is the local spectrum along the interface between two resins (DGEBA + 4'4'DDS and TGDDM + 4'4'DDS). Peak A in Fig. 1 is the common peak of both material, peak B is only appeared in DGEBA + 4'4'DDS resin. IR absorption peak around 1040 /cm (C-O-C) is another candidate to identify two materials, and includes chemical bonding information at the interface.

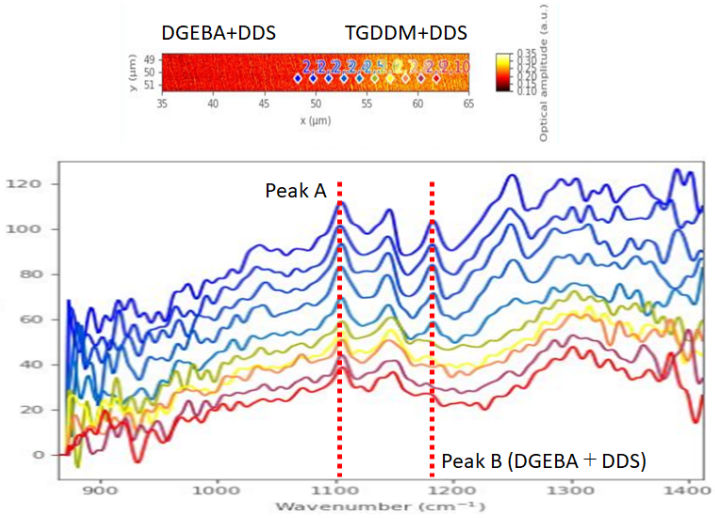

Fig. 1. High resolution FTIR Spectra of resin interface (1 micon step).

SPM system used in the experiment includes optical detector for nearfield imaging and FTIR interferometer as shown in right illustration in Fig. 2. Resolution of these technique were systematically investigated with well-defined grating made of Si and SiO_2. The grating, which was designed for testing nano-FTIR resolution and mapping resolution with near field optical microscope. The mapping resolution of infrared absorption was systematically investigated as shown in Fig. 2. Fig. 2 is the nearfield scanning optical microscope (NSOM) image of Si/SiO_2 nano-grating. Fifteen nano-meter line is resolved, when wavelength of laser is set to be absorption peak of SiO_2. Results of NSOM mapping using infrared absorption spectrum for the adhesion interface of resin will also be reported.

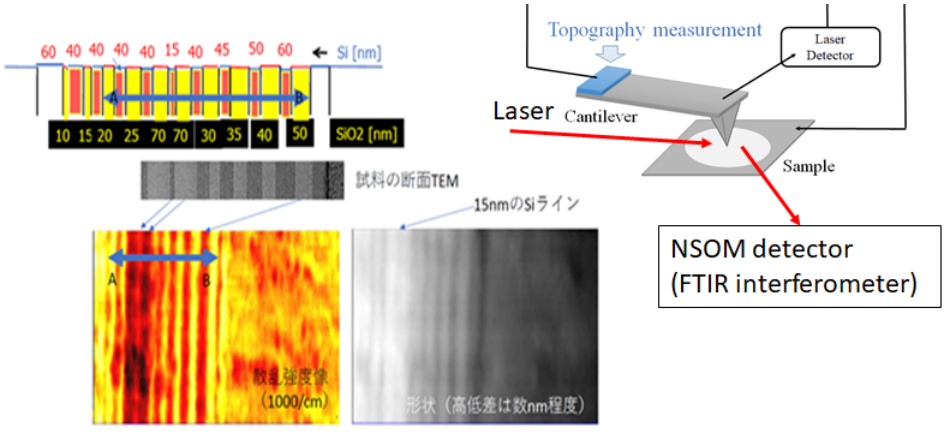

Fig. 2. High resolution NSOM image of Si/SiO_2 test sample (left) and imaging system (right)

KA-1 **doi: 10.1093/jmicro/dfz043**

Application of modified SEM techniques to evaluate renal pathology

Osamu Ichii[1], Md. Abdul Masum[1,2], Yaser Hosny Ali Elewa[1,3] and Yasuhiro Kon[1]

[1]Laboratory of Anatomy, Department of Basic Veterinary Sciences, Faculty of Veterinary Medicine, Hokkaido University, Sapporo, Japan

[2]Department of Anatomy, Histology and Physiology, Faculty of Animal Science and Veterinary Medicine, Sher-e-Bangla Agricultural University, Dhaka, Bangladesh

[3]Department of Histology, Faculty of Veterinary Medicine, Zagazig University, Zagazig, Egypt

In recent years, owing to aging of individuals, the increasing number of humans as well as animals such as companion animals (dogs and cats) suffering from chronic kidney disease (CKD) has become a global concern [1]. Further, CKD is associated with the development of end-stage renal disease and cardiovascular complications. For the diagnosis of renal disease, particularly glomerular disease, histopathological examinations such as light microscopy and transmission electron microscopy (TEM) are crucial. Since the main cause of proteinuria is a disruption of the blood-urine barrier (BUB) in the glomerulus, the morphological evaluation of the BUB is essential for early diagnosis and determination of therapeutic strategies.

TEM observation is useful in examining the morphological changes in the glomerular BUB components, such as the endothelial cells, glomerular basement membrane (GBM), and podocytes. However, the TEM observation area was limited although we obtained a tiny amount of renal tissues from the kidney of patients through biopsy. Recently, scanning electron microscopy (SEM) has been applied to obtain TEM-like images, as serial block face-SEM has been developed. Interestingly, Koga *et al*. performed SEM using a semi-thin section and reported that this method could aid in visualizing large areas of sections and obtaining TEM-like images [2]. Therefore, in this study, we modified these SEM methods to develop the so-called "mSEM" and we applied this method in the analysis of ultrastructural renal pathology.

First, we compared the standard TEM and mSEM for the renal histopathological analysis. A BXSB/MpJ-Yaa mouse was used as a CKD mouse model due to the presence of autoimmune glomerulonephritis. BXSB/MpJ-Yaa mice have a genetic mutation on the Y chromosome called "Y-linked autoimmune acceleration" (*Yaa*), and the male mice develop more severe glomerulonephritis than the female mice due to the *Yaa* mutation. Similar to TEM, mSEM revealed pathological changes in glomerular BUB components of BXSB/MpJ-Yaa mice, such as foot process effacement of podocytes and the deposition of high electron-dense materials in the GBM, indicating immune-complex depositions. Further, due to the larger observation area of mSEM compared to standard TEM, the histoplanimetric analysis of BUB ultrastructural changes was more efficient in the former. Briefly, the quantitative values of podocyte foot process and the endothelial fenestration by mSEM revealed a significant decrease in BXSB/MpJ-Yaa mice compared to its wild-type, BXSB/MpJ mice. Further, these values were significantly correlated with the indices of endothelial cell injury (decreased CD34 expression) or podocyte injury (decreased nephrin, podocin, and synaptopodin expression).
We also applied mSEM analysis to evaluate the histopathological feature of the tubulointerstitium. In mSEM analysis, BXSB/MpJ mice showed normal peritubular capillaries while BXSB/MpJ-Yaa mice clearly showed injuries in the peritubular capillaries, characterized by thickening of endothelial cells, loss of endothelial fenestration, and irregular capillary lumina. Further, histoplanimetrical indices of peritubular capillary damage significantly correlated with inflammatory cytokine expression in the renal tubules (Interleukin-36 alpha) and the expression of disease-aggravating factor (Toll-like receptor 9 expression) in the peritubular capillaries.

Thus, we demonstrated and reported that the mSEM method was useful in analyzing the changes in ultrastructure of the glomerular and tubulointerstitial lesions using a mouse model [3-5]. In particular, mSEM-based renal histopathological analysis would be advantageous owing to the larger observation area to analyze an adequate number of glomeruli or renal tubules for the diagnosis and histoplanimetrical analysis in clinical as well as basic science research.

1. Marino CL et al, *J Feline Med Surg* 16 (2014) 465-472.
2. Koga D et al, *Microscopy (Oxf)* 64 (2015) 387–394.
3. Masum MA et al, *Sci Rep* 8 (2018) 10276.
4. Masum MA et al, *Autoimmunity* 51 (2018) 386-398.
5. Masum MA et al, *Lupus* 28(2019) 324-333.

KA-2 doi: 10.1093/jmicro/dfz044

Structural Analysis Based on Measurements of Slight Cation Displacements from High Resolution STEM Images

Shunsuke Kobayashi[1]

[1]Nanostructures Research Laboratory, Japan Fine Ceramics Center, Nagoya, Japan.

Materials properties of crystalline solids are strongly related to the local lattice distortion in their component crystals. Scanning transmission electron microscopy (STEM) is a useful method for analyzing materials at the atomic level. Today's STEM techniques can successfully detect cation displacements smaller than 10 picometers [1,2]. Analyzing changes in atomic positions near interfaces with picometer-level precision is crucial to understand the relationships between structures and properties. In this study, we apply STEM techniques for picometer-level structural analysis to ferroelectric material $BaTiO_3$ and Li-ion battery cathode material $LiFePO_4$.

Figure 1a shows a HAADF STEM image obtained from a $BaTiO_3$ film on a (110) orthorhombic $GdScO_3$ substrate, which induces anisotropic strain in the film because of the different in-plane lattice parameters. We analyzed the displacements of cations at the picometer level, producing images of the nanodomain structure as shown in Fig. 1b [3,4]. It is possible that these nanodomains are formed as a result of the anisotropic misfit strain at the interface extending into the film bulk.

Figure 2a shows an atomic-resolution HAADF STEM image of the interface formed between Li-rich and Li-poor phases of $LiFePO_4$. The lower half of the image contains the (metastable) intermediate phase found only in the boundary region, and the upper half the thermodynamically stable Li-poor phase. Li concentrations in these two phases were estimated from electron energy loss spectroscopy to be around 0.6 and 0, respectively [5,6]. To determine Li concentration distributions with atomic resolution, cation displacement measurements were made using the image in Fig. 2a. Plotting the local lattice differentials produces the concentration map in Fig. 2b. This result shows that the boundary between the Li-poor phase and intermediate phase ($Li_{0.6}FePO_4$) is sharp at the atomic level.

The wealth of information provided by these visualization techniques should enable valuable insights to be made into the mechanisms behind many different properties for a wide range of technically important materials.

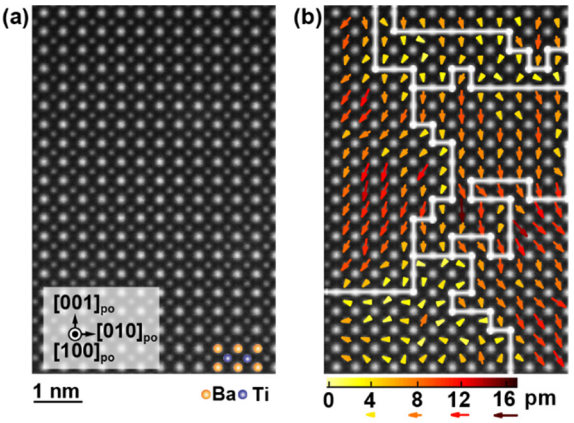

Fig. 1. (a) HAADF STEM image of $BaTiO_3$ film. (b) Ti ion displacement vector map.

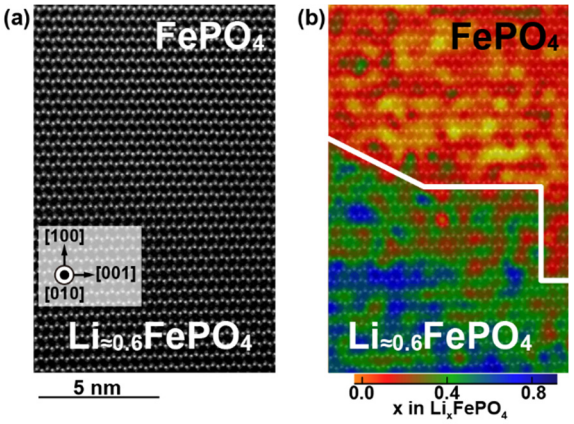

Fig. 2. (a) HAADF STEM image of the interface between intermediate phase $Li_{\approx 0.6}FePO_4$ and $FePO_4$. (b) Li concentration distribution map.

References

1. K. Kimoto et al., Ultramicroscopy 110, (2010) 778-782.
2. S. Kobayashi et al., Appl. Phys. Lett. 100, (2012)193112.
3. S. Kobayashi et al., J. Appl. Phys. 123, (2018) 064102.
4. S. Kobayashi et al., KENBIKYO 54, (2019) 19-23.
5. S. Kobayashi et al., Microscopy 66, (2017) 254-260.
6. S. Kobayashi et al., Nat. Commun. 9, (2018) 2863.

Acknowledgements

The author thanks K. Inoue, C. A. J. Fisher, A. Kuwabara, T. Kato, Y. Ukyo, T. Yamamoto and Y. Ikuhara for useful discussions. This work was supported by the Kazato Research Foundation of Japan and JSPS KAKENHI Grant Numbers 17K14119 and 19H02606. Part of this work was supported by the Research & Development Initiative for Scientific Innovation of New Generation Batteries 2 (RISING 2) project from the New Energy and Industrial Technology Development Organization (NEDO), Japan.

LS-1 **doi: 10.1093/jmicro/dfz045**

Local electronic structure analysis and its mapping by STEM-EELS

Mitsutaka Haruta[1].

[1]Institute for Chemical Research, Kyoto University, Kyoto, Japan,

Since transition metal (TM) oxides exhibit a variety of physical properties which are sensitively related to their complex crystal structures and constituent elements, many experimental and theoretical studies have been conducted for not only bulk but also thin film. In particular, the relationship between localized TM *d*-band and oxygen 2*p* band is one of the key factors to control of the property. For further understanding, it is important to examine individual electronic structure with atomic resolution. This is because it has often some nonequivalent atomic sites in a unit cell even a single crystal, and they have different electronic structure for the same element. In addition, the non-periodic region such as defect, interface and surface is also important for material property and its analysis is being vigorously advanced.

In the field of high spatial resolution analysis, scanning transmission electron microscopy (STEM) combined with electron energy-loss spectroscopy (EELS) is the powerful tool to know both elemental and electronic structure with atomic scale. Since the fine structure of O *K*-edge reflects the unoccupied 2*p* state which hybridized with cation electronic orbital due to its covalent bonding character, it includes much information about chemical bond. And TM $L_{2,3}$-edge reflects crystal field splitting of *d*-state, oxidation state, magnetic moment etc. However, while this technique can offer elemental and electronic state with atomic resolution, it is, in principle, difficult to experimentally extract the information with truly atomic resolution due to the physically limited spatial resolution caused by the delocalization of inelastic scattering [1]. Therefore, careful attention of the mixing of signals from neighboring atomic-columns is required. In addition, it is not easy to experimentally obtain high signal-to-noise ratio spectra with high spatial resolution without sample damage due to the limitations of practical experimental conditions. In conventional acquisition method, the electron dose required to obtain a high signal-to-noise ratio spectrum from one atomic columns is higher than the critical dose for many materials. Therefore, a more efficient detection system is required.

In my previous researches, I focused on O *K*-edge and TM $L_{2,3}$-edge with high spatial resolution for transition metal oxide which has layered structure. For example, anisotropic chemical bond between Cu 3*d* state and O 2*p* state due to *Jahn-Teller* distortion [2] and difference of covalent bonding character between octahedral FeO_6 and tetrahedral FeO_4 were investigated [3]. And electronic structure mapping with atomic resolution, such as hybridization state mapping between oxygen and cation [4] and doped hole mapping of cuprate super conductor [5] were demonstrated. In addition, since the layered crystal structure can be viewed as the material including periodic interface, we have been tracking research about the practical spatial component of EELS signal obtained with atomic scale [2-4, 6-7]. Recently, extremely low count detection for EELS spectrum imaging is demonstrated by reducing CCD noise [8]. This method combined with multiple spectrum imaging technique would realize atomic resolution spectroscopy for measuring low signal spectrum such as nomonchromated spectra and for radiation sensitive materials.

1.R. F. Egerton, “Electron Energy-Loss Spectroscopy in the Electron Microscope”, 3rd ed. Plenum Press, New York, (2011)
2. M Haruta et al., Phys. Rev. B. 80 (2009) 165123.
3. M Haruta et al., J. Appl. Phys. 110 (2011) 033708.
4. M Haruta et al., Appl. Phys. Lett. 100 (2012) 163107.
5. M Haruta et al., Phys. Rev. B. 97 (2019) 205139.
6. M Haruta et al., ACS Nano. 10 (2016) 6680-6684.
7. M Haruta et al., Appl. Phys. Lett. 113 (2018) 083110.
8. M Haruta et al., Ultramicroscopy 207 (2019) 112827.

Poster Sessions

Materials and Instruments (PM)

Medical and Biological Sciences (PB)

PM-01 **doi: 10.1093/jmicro/dfz101**

Exothermic behavior and microstructures of the $LiNi_{1/3}Mn_{1/3}Co_{1/3}O_2$ positive electrode layer for all-solid-state lithium batteries.

Hirofumi Tsukasaki[1], Tomoki Uchiyama[3], Kentaro Yamamoto[3], Misae Otoyama[2], Hiroe Kowada[2], Atsuki Atarashi[1], Shigeo Mori[1], Yoshiharu Uchimoto[3], Akitoshi Hayashi[2] and Masahiro Tatsumisago[2]

[1]Dept. of Materials Science, Osaka Pref. Univ., Sakai, Osaka 599-8531, Japan., [2] Dept. of Applied Chemistry, Osaka Pref. Univ., Sakai, Osaka 599-8531, Japan and [3]Graduate School of Human and Environmental Studies, Kyoto University, Nihonmatsu-cho, Yoshida, Sakyo-ku, Kyoto, 606-8501, Japan.

A positive electrode composite comprising $LiNi_{1/3}Mn_{1/3}Co_{1/3}O_2$ (NMC) and Li_3PS_4 (LPS) glass electrolytes exhibits excellent charge–discharge cycle characteristics [1]. To clarify the origin of exothermal reactions during heating, structural changes of the NMC–LPS composites were investigated by *ex-situ* TEM observations as well as *in-situ* synchrotron X-ray diffraction measurements. Figure 1 shows the hollow-cone dark filed (HCDF) image for the initially charged NMC–LPS composites after heating at 500 °C. Based on the analysis of the corresponding ED pattern, main crystalline phases precipitated were identified as Li_3PO_4, $CoNi_2S_4$ and MnS. The HCDF image shows these crystalline phases were present as a nanocrystellite, as indicated by the arrows. These results suggest that LPS and NMC thermally react each other, which leads to the exothermal reactions [2].

1. H. Tsukasai et al, Scientific Reports, 8 (2018) 6214.
2. H. Tsukasai et al, J. Power. Sources, 434 (2019) 226714.

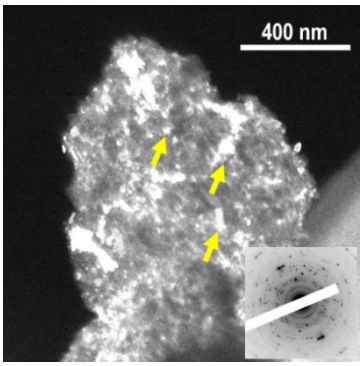

Fig. 1. The ED pattern of the initially charged NMC–LPS composites after heating at 500°C.

PM-02 **doi: 10.1093/jmicro/dfz099**

Analysis of Lithium Ion Battery Materials Using Statistical Machine Learning and Image Processing of Electron Microscopy Data

Hiromochi Tanaka[1], Tetsushi Watari[1], Takahiro Tsubouchi[1], Hisao Yamashige[1], Takashi Kato[2] and Motoki Shiga[3]

[1]Material Engineering Div. No. 2, Toyota Motor Corporation, Aichi, Japan, [2]Advanced Material Product Div., OHARA INC., Kanagawa, Japan and [3]Faculty of Engineering, Gifu University, Gifu, Japan

Machine learning and image processing become important for the efficiency of TEM analysis. We applied statistical machine learning to STEM-EELS spectrum images (SI) for identification of material phase in lithium ion battery materials. Figure 1 shows the result of statistical machine learning of STEM-EELS-SI acquired from fully charged silicon-based anode. Characteristic spectra and distributions of Si and Li-Si alloy were extracted automatically by vertex component analysis (VCA) [1] included in the Python package [2]. We also developed an effective image thresholding process using multiple image filters for quantitative analysis of crystal grains distribution in a solid oxide electrolyte (LICGC™ [3, 4]).

1. J. M. P. Nascimento and J. M. Bioucas, IEEE Trans. on Geoscience and Remote Sensing 43(4) (2005) 898-910
2. MALSpy. Available from: https://github.com/MotokiShiga
3. J. Fu, Solid State Ionics 96 (1997) 1950200
4. T. Katoh et al., J. Ceram. Soc. Japan 118 (2010) 1159-1162

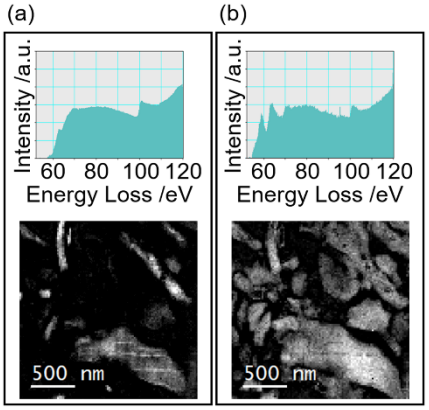

Fig. 1. Spectra and distributions of (a) Si and (b) Li-Si alloy.

PM-03 **doi: 10.1093/jmicro/dfz093**

New Magnetic Structure Imaging Techniques in Polycrystalline Materials by DPC STEM

Yoshiki O. Murakami[1], Takehito Seki[1], Akihito Kinoshita[2], Tetsuya Shoji[2], Yuichi Ikuhara[1,3] and Naoya Shibata[1,3].

[1]Institute of Engineering Innovation, The University of Tokyo, Bunkyo-ku, Tokyo, Japan, [2]Advanced Material Engineering Division, Toyota Motor Corporation, Susono, Shizuoka, Japan and [3]Nano Structures Research Laboratory, Japan Fine Ceramics Center, Atsuta-ku, Nagoya, Japan

High coercivity permanent magnets play a vital role in electric motors. Microstructures such as grain boundaries are considered to strongly influence coercivity of the materials [1]. However, the fundamental interaction processes between structural grain boundaries and magnetic domain structures is still elusive. Differential phase contrast (DPC) is a high-resolution imaging technique to visualize electromagnetic fields inside samples in scanning transmission electron microscopy (STEM) [2]. Although DPC is capable of the simultaneous observation of microstructures and magnetic structures in permanent magnets, the diffraction contrast in experimental DPC image make it difficult to image a magnetic structure when DPC is applied to polycrystalline sample. In this study, we assumed that the diffraction contrast is randomly changed when tilting samples. Then we developed a technique to supress the diffraction contrast by averaging experimental DPC image series acquired on slightly different sample-tilt conditions (Fig. 1). This technique enables robust visualization of a magnetic structure in polycrystalline materials.

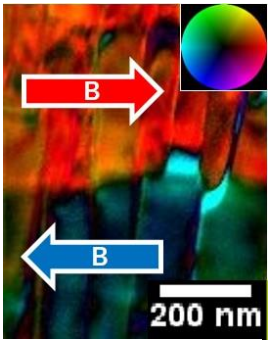

Fig. 1. Averaged DPC image of 64 tilt conditions of Nd-Fe-B sample. Magnetic domain wall is clearly visualized.

[1] T. T. Sasaki et al, Acta Mater 115 (2016) 269-277.
[2] N. Shibata et al, Acc. Chem. Res. 50 (2017) 1502-1512.

PM-04 **doi: 10.1093/jmicro/dfz090**

Characterization of Sb_2Te_3 / GeTe Composite Thin Films Fabricated by RF-Magnetron Sputtering

Kagekatsu Kondo[1], Kazuhisa Sato[1,2], Hidehiro Yasuda[1,2]

[1]Division of Materials and Manufacturing Science, Graduate School of Engineering, Osaka University, Osaka, Japan [2]Research Center for Ultra-High Voltage Electron Microscopy Osaka University, Osaka, Japan

Ge-Sb-Te (GST) thin films are widely used as phase-change memory materials and their structural dynamics has been intensively investigated so far [1]. Recently giant magnetoresitance (GMR) of over 2000% was found in Sb_2Te_3 / GeTe multilayered films, while Sb_2Te_3 and GeTe are both non-magnetic materials [2]. The occurrence of the GMR is considered to be due to interfacial atomic structures of the stacked layers [3]. In this study, unlike previous studies using molecular beam epitaxy for film growth, we attempted to control the Sb_2Te_3/GeTe interface structure using rf-magnetron sputtering. Thin films of GeTe/Sb_2Te_3/GeTe stacked layers were prepared by alternate deposition of GeTe and Sb_2Te_3 by rf-magnetron sputtering onto a cleaved NaCl(001) substrate kept at 570 K. Structure and morphology of the prepared specimens were examined using transmission electron microscopy (TEM) and electron diffraction. Plan-view observation revealed that prepared specimens were discontinuous films including small pores, which can be attributed to island growth of GeTe and Sb_2Te_3. A crystallographic orientation relationship exists between Sb_2Te_3 and GeTe as follows: $(1\bar{2}10)Sb_2Te_3$ // (220)GeTe, $[50\bar{5}1]Sb_2Te_3$ //[001] GeTe. Based on this orientation relationship, we proposed a model structure of stacked Sb_2Te_3 and GeTe, which was confirmed by cross-sectional TEM observation.

1. E. Matsubara et al, Phys. Rev. Lett. 117, (2016) 135501.
2. J. Tominaga et al, Appl. Phys. Lett. 99, (2011) 152105.
3. T. Nguyen et al, Scientific Reports 6, (2017) 27716.

PM-05 **doi: 10.1093/jmicro/dfz088**

Anisotropic Electronic Structure of Metal Borides Studied by Soft X-ray Emission Spectroscopy

Takeshi Ito[1], Yohei Sato[1] and Masami Terauchi[1]

[1]Institute of Multidisciplinary Research for Advanced Materials, Tohoku University, Sendai, Japan.

Some kinds of metal borides have anisotropic crystal structures. AlB_2 and MgB_2 have 2D structure of honeycomb sheets consisting of B atoms. FeB and Fe_2B have 1D chains of B atoms in those crystal structures. To investigate electronic structures characteristic to the anisotropic bonding between B atoms, it is effective to conduct angle-resolved soft X-ray emission spectroscopy (AR-SXES). In this study, the anisotropic electronic structure of metal borides were investigated by AR-SXES based on transmission electron microscopy.

Figure 1 shows B K-emission spectra of AlB_2 detected at (A) [001] direction and (B) perpendicular to it. Those intensity profiles reflect the energy distribution of B-2p components, due to dipole selection rule, in valence bands (partial density of states: *p*-DOS). The spectrum-A shows a peak at 183 eV, which is lower energy of that of B, 184 eV. This suggests that the energy of dominant component of bonding orbitals perpendicular to [001] (correspond to A) is lower than that of ∥ [001] (correspond to B). Comparisons between experimental spectra and calculated *p*-DOS will be conducted to reveal the anisotropic electronic structures.

AR-SXES experimental results and theoretical calculations on MgB_2 and Fe_2B will be also reported.

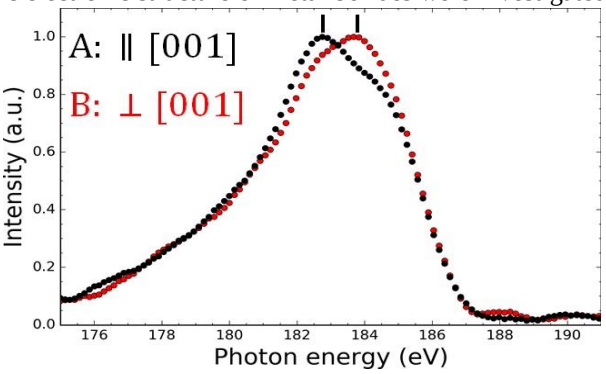

Fig. 1. B K-emission spectra of AlB_2 obtained at different crystal orientations.

PM-06 **doi: 10.1093/jmicro/dfz092**

Electronic Structure of Nitrogen-Doped Graphite Films Studied by Soft X-ray Emission Spectroscopy

K.Matsuura[1], Y.Sato[1], M.Terauchi[1], M.Aono[2], S.Hashimoto[1], S.Ogawa[1] and Y.Takakuwa[1]

[1]IMRAM, Tohoku University, Sendai, Japan. [2]Kagoshima University, Kagoshima, Japan.

Nitrogen-doped carbon materials are remarked as a catalysis having the superior electrocatalytic activity for the oxygen reduction reaction (ORR) [1]. Thus, the material is expected to substitute for platinum as a catalysis of the fuel cell. The origin of the ORR is believed to be pyridinic nitrogen, which is the nitrogen atom bonded to two atoms on the edge of graphite. Thus, in order to produce the material of large capacity and of low cost, nitrogen-doped graphite (NDG) films were prepared by PA-PECVD method [2]. The electronic structure of this material has not been revealed. In this study, soft X-ray emission spectroscopy based on electron microscopy was applied to this material to clarify the characteristic electronic structure of the NDG film.

Figure1 shows second order C K-emission spectra obtained from the NDG film and graphite. The maximum intensity of NDG at 138.5eV, which is the half energy of the first order, is almost the same energy with that of graphite. The maximum intensity corresponds to C-sp^2 bonding state of graphite. On the other hand, slight differences of intensity distribution are observed as indicated by arrows. Those differences of NDG might come from bonding states of carbon atom with nitrogen atoms. To interpret this bonding states, theoretical calculation will be conducted and compared with the experimental results.

[1] L. Qu et al, ACS Nano, vol.4, no.3(2010), pp. 1321-1326. [2] T. Takami et al, e-Journal Surf. Sci. Nanotechnology., vol.7, no.December(2009), pp. 882-890.

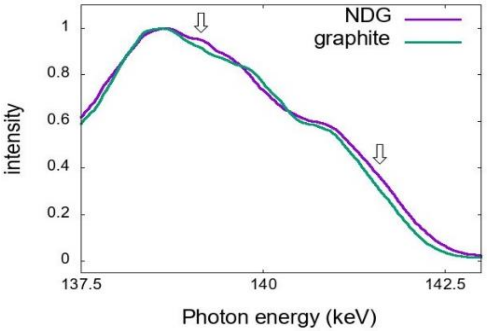

Fig. 1. Second order C K-emission spectra of NDG and graphite

PM-07 **doi: 10.1093/jmicro/dfz087**

Structure Characterization of Bi-Doped SnSe Thin Films Fabricated by Pluse Laser Deposition

Yoshiki Hirayama, Manabu Ishimaru, Tomoya Horide and Kaname Matsumoto

Department of Materials Science and Engineering, Kyushu Institute of Technology, Kitakyushu, Fukuoka, Japan.

Tin selenide (SnSe) has an orthorhombic structure with a = 1.149, b = 0.444, and c = 0.414 nm, and shows an excellent thermoelectric performance in the b- and c-axes directions. The crystallographic orientation can be controlled by thin films epitaxially grown on a substrate, but the structures of SnSe thin films have not been elucidated yet. In the present study, we performed structural characterization of SnSe thin films using TEM and STEM. SnSe thin films were deposited on a $SrTiO_3$ substrate at 300 ^oC by pulse laser deposition using a target consisting of 50% Se, 44% Sn, and 6% Bi. Fig. 1 shows a cross-sectional bright-field TEM image of Bi-doped SnSe thin film. Columnar contrasts consisting bright and dark regions are observed from the substrate to the surface in the thin film [1]. Electron diffraction experiments revealed that the thin film consists of (001) and (010) domains with the a-axis parallel to the growth direction: the lattice is rotated by 90° around the a-axis. The SnSe thin film has almost the same structure as the single crystal, but numerous stacking faults perpendicular to the growth direction were included. Element mapping and high-angle annular dark-field images revealed that two types of Bi precipitates exist: large precipitates with the size of 100 nm and small ones with 10 nm. The former exists on the domain boundary, while the latter is formed inside the domain. We will discuss the relationships between structures and thermoelectric properties of SnSe thin films in the poster session.

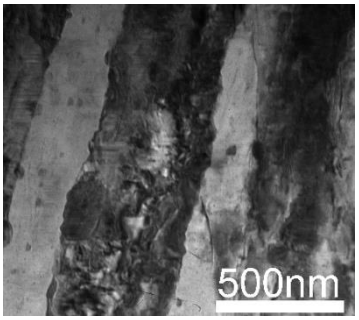

Fig. 1. Cross-sectional bright-field TEM image of Bi-doped sample.

1. T Horide et al., ACS Appl. Mater. Interfaces 11 (2019) 27057-27063.

PM-08 **doi: 10.1093/jmicro/dfz100**

Precipitation of Pigeonite and Enstatite in Augite of Ultrahigh Temperature Metamorphic Rock from Antarctica

Shoichi Toh[1], Tomoharu Miyamoto[2]

[1] Fukuoka University, Faculty of Science, Fukuoka, Japan, [2] Kyushu University, Faculty of Science, Fukuoka, Japan.

Since the rocks and minerals that compose earth and planetary materials may have traces of temperature, pressure, and stress, their formation history, occasionally, can be obtained by analysing them. In Antarctica, ultrahigh-temperarture (UHT) metamorphic rocks were found as the major component of old continental crust. The UHT metamorphic rocks are recognized from paragenesis and texture of constituent minerals, and thought to have been formed at the 1000°C or higher temperature condition [1]. Considering about their origin are important for understanding behaviour and history of such rocks and continental crust.

In the present study, we found a characteristic precipitation structure in pyroxene in ultrahigh temperature metamorphic rocks collected in Skallevikshalsen, Dronning Maud Land, East Antarctica. Based on the principles that have been clarified from research on pyroxene dissolution phenomena, a working hypothesis about the tissue formation process was established. The purpose of this study is to elucidate the temperature history that led to the formation of a characteristic structure by examining the hypothesis and reconstructing it as necessary. Careful observation and analysis were performed using a polarizing microscope, SEM and EPMA. Furthermore, the orientation of the interface boundary and morphology of the precipitated phases were examined using an analytical electron microscope (AEM). Microscopic observations using a polarizing microscope and EPMA analysis suggest that only Ca and Fe may be substituted between the matrix and the precipitates. And morphology change phenomena [2] was observed in pigeonite precipitates using AEM. Estimation of temperature history based on chemical composition and crystallographic data will be presented.

1. Yoshimura et al., Geodynamic evolution of East Antarctica, Geological Society, Spec. Pub., SP308, (2008), 377-390.
2. Kitamura et al., Proc. Japan Acad., 57, Ser. B, (1981) 183-187.

PM-09 **doi: 10.1093/jmicro/dfz107**

Evaluation of crystal structure and surface-to-molecule interaction in hydrothermally grown titanium oxide nanowires

Takato Yokoo[1], Kazuki Nagashima[2], Takeshi Yanagida[2], Yuki Obukuro[3] and Tetsuya Okuyama[3]

[1]Advanced Engineering School, National Institute of Technology, Kurume College, Fukuoka, Japan, [2] Institute for Materials Chemistry and Engineering, Kyusyu University, Fukuoka, Japan, [3]Department of Materials System Engineering, National Institute of Technology, Kurume College, Fukuoka, Japan

Titanium oxide nanowires have attracted increasing attention in photo-catalysis, chemical sensor, solar cell due to not only the huge surface but also their fascinating electrical and optical properties and excellent chemical stability. A hydrothermal growth is a mass-productive and a low energy consumption nanowire growth technique, which is widely used for fabricating metal oxide nanowires e.g. TiO_2 nanowires, ZnO nanowires, WO_3 nanowires. Especially for TiO_2 nanowires, NaOH aqueous solution was mainly utilized for both controlling pH value and sidewall capping agent. The capping event may influence the nanowire formation process and the surface property, which depends on the type of alkaline solvent although they have been scarcely investigated.

In this study, we fabricate the titanium oxide nanowires by using NaOH and KOH solution. The hydrothermal growth process was performed at 200 ºC for 24 hrs. The fabricated samples were then annealed at 700 ºC in air prior to the characterization. As a result of XRD analysis, anatase TiO_2 nanowires were obtained for the sample fabricated by KOH while Na-Ti-O composite structure was observed for the sample by NaOH. Next we characterized the adsorption property of nonanal (C9 aldehyde, lung cancer marker in exhaled human breath) on these nanowires by FT-IR. For both samples, the peaks of C-H stretching vibration, which is corresponding to the alkyl chain of nonanal, were observed around 2850-2950 cm^{-1}, but the relative intensity of the peak was found to be higher for the sample by KOH. Thus these results indicate that the alkaline solvent strongly affects both the nanowire formation and the surface property of hydrothermally grown metal oxide nanowires.

PM-10 **doi: 10.1093/jmicro/dfz094**

Effect of microstructure on creep property of W-added heat resistant cast steel

Kinh-Luan Ngo-Huynh[1], Tetsuya Okuyama[2], Koreaki Koizumi[1] and Masaki Kudo[3]

[1]Itoh Kikoh Co. Ltd., Aichi, Japan
[2]Department of Materials System Engineering, National Institute of Technology, Kurume College, Fukuoka, Japan
[3]The Ultramicroscopy Research Center, Kyushu University, Fukuoka, Japan

Recently, for producing in-furnace parts of centrifugal cast tubes and heat treatment jigs, two representative kinds of developed Ni-Cr austenitic heat resistant cast steel have been chosen instead of conventional cast steels, because increment of the loading capacity of heat-treated products on the jigs as well as improvement of the lifespan are requested by customers. Among these cast steels, unlike strong carbide-forming elements such as Nb and Ti, little was known about the effect of microstructure of austenitic cast steel added with substitution solute elements (W or Mo) on creep property during high temperature exposure.

In this study, microstructures of JIS SCH21 cast steel added with W in as-cast state and creep test of heat resistant were investigated using scanning transmission electron microscopy, energy dispersive X-ray spectrometry, X-ray diffractometry and X-ray photoelectron spectroscopy. As a result, tungsten dissolves in matrix as solid solution and promotes microstructural refinement of primary carbides. Additionally, presence of tungsten in primary chromium carbides improves thermal stabilization, resulting that primary carbides decompose difficultly at elevated temperature. As seen in Fig.1, crack propagation due to creep is suppressed by the primary carbides. Such microstructures which provide both of solid solution strengthening and dispersion strengthening are effective for improving creep property of austenitic heat resistant cast steel.

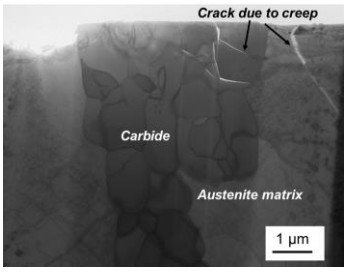

Fig. 1. STEM image of SCH21-1.4mass% when creep tested at 1223K

PM-11 **doi: 10.1093/jmicro/dfz105**

Atom Location Analysis on Atomic-resolution STEM Images of Metal Nanoparticles by Convolutional Neural Network Approach

Tomokazu Yamamoto [1], Kohei Aso[1] and Syo Matsumura[2]

[1]Department of Applied Quantum Physics and Nuclear Engineering, Kyushu University, Fukuoka, Japan,
[2]The Ultramicroscopy Research Center, Kyushu University, Fukuoka, Japan

Metallic nanoparticles have attracted much attention as catalysts for various chemical reactions. Recently, aberration-corrected STEM imaging was often used for atomistic characterization of the metallic nanoparticles because their catalytic properties depends on their sizes, shapes, crystal structure and presence of lattice defects such as staking faults and twins. The manual analyses for many atomic-resolution STEM images of nanoparticles are sometimes necessary for statistics and it is very time-consuming. Automation of image analysis is desirable in this purpose. Recently, successful object recognition and classification for complex natural images have been achieved for using convolutional neural network (CNN) framework [1]. In this study, we tried automated detection of nanoparticles in STEM images using trained CNNs implemented in deep-learning toolbox of MATLAB software. The CNNs were trained using a simulated images set of a few-nm sized nanoparticles generated with the Gaussian atom model [2]. After nanoparticle detection process using CNNs, we also fitted Gaussian functions for atomic columns of each nanoparticle to identify the atom positions. The established CNNs were able to distinguish nanoparticle regions from background region in simulated and experimental STEM images with small number of errors and initial atom column positions were generated successfully for further analyses.

1. J. Redmon, et al., Proc. IEEE Conf. Comput. Vis. Pattern Recognit. (CVPR 2016) 779.
2. B.C Curley, et al., J. Phys. Chem. C 111 (2007) 17846-17851.

PM-12 **doi: 10.1093/jmicro/dfz104**

3D-structural distributions of silica aggregates in styrene-butadiene rubber obtained by FIB-SEM

Ryota Yamamoto[1], Katsumi Hagita[2], Kazuya Morishita[1], Hirofumi Senga[1], Tetsuo Tominaga[1], Hiroshi Jinnai[3]
[1] JSR Corporation, Yokkaichi Research Center, Yokkaichi, Japan,
[2] Department of Applied Physics, National Defense Academy, Yokosuka, Japan,
[3] Institute of Multidisciplinary Research for Advanced Materials, Tohoku University, Sendai, Japan.

Filler aggregates in rubber play important role to their physical property of filler-filled styrene-butadiene rubber (SBR) that is used as tire rubber. FIB-SEM is a powerful tool to observe 3D-structure of aggregates directly in wide region (micrometer cubic) with single nanometer resolution [1]. In this study, we extracted individual 3D-structures of aggregates from FIB-SEM images of filler-filled SBRs. Here, we evaluated the characteristics of 3D watershed segmentation to these images. In commercial tire rubbers, polymer-filler interactions due to chain end modifications in SBR were used to improve 3D-structural distributions of silica aggregates. As the first test, we compared size distributions of silica aggregates in modified and non-modified SBR vulcanizates. Figure 1 shows cumulative frequency of number and volume of silica aggregates. In modified-SBR, the number distribution of small aggregates ($<10^5$ nm^2) reaches 50%, but only 20% in non-modified SBR. Contrary, large aggregates ($>10^6$ nm^2) exist in non-modified SBR, although its probability in modified SBR was very small. These results suggest that the polymer-filler interactions may affect size distribution of silica aggregates in wide volume range (10^4-10^6 nm^2).

[1] K. Hagita, T. Higuchi and H. Jinnai, Scientific Reports 8 (2018) 5877.

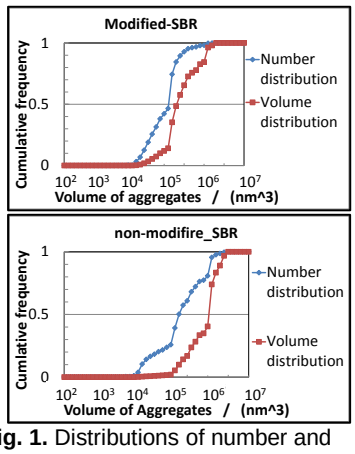

Fig. 1. Distributions of number and volume of aggregates in modified SBR (upper) and non-modified SBR (lower)

PM-13 **doi: 10.1093/jmicro/dfz098**

Three-dimensional analysis of porous material by FIB/SEM and correlation with physical property measurement

Kazumi Takahashi[1], Shigeru Yoshimoto[2], and Yuji Otsuka[1].

[1]Morphological Research Laboratory, Toray Research Center, Inc., Otsu, Japan, [2]Materials Characterization Research Laboratory, Toray Research Center, Inc., Otsu, Japan.

Porous materials having an structure that is indeterminate form are used in various fields. Since the pore structure is the key character that affects the function of devices, it is important to understand the structure quantitatively and feed it back to material research and development. As a method for quantifying the pore structure, there are image analysis and actual analysis by physical property measurement, etc. However, when comparing values between methods, there is a concern that the values do not match or simply cannot be compared. In this study, we tried to confirm the correlation between two metal filters with different filtration properties by using FIB/SEM for three-dimensional analysis and mercury intrusion porosimetry as a physical property measurement. Although the porosity calculated from each method has some difference, the correlation of values between samples is good, and the structure captured by each method is judged to be the same. The area-weighted average of the diameter of the throat calculated by PNM (Pore Network Modeling) was found to be in good agreement with the peak value of the mercury intrusion porosimetry.

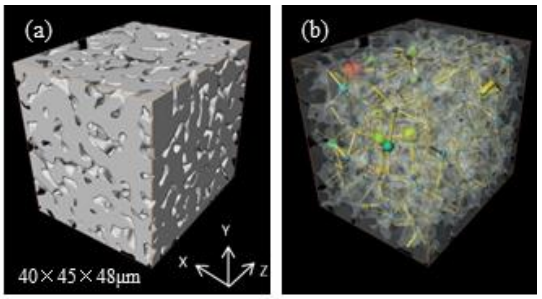

Fig. 1. (a)Volume rendering and (b)Pore network modelling of Metal filiter.

PM-14 **doi: 10.1093/jmicro/dfz103**

Three Dimensional Observations and Quantitative Analysis of Functional Polymer Materials.

Fumiya Uehara[1], Masayoshi Muraoka[1], Naoto Kaneko[1] and Yuji Otsuka[1]

[1] Morphological Research Laboratory, Toray Research Center, Inc., Otsu, Japan

3D printer has been used for several industrial products because of their high-designable processability. However, voids occur depending on processing conditions and might cause adverse influence such as degradation of mechanical properties. Thus, it is important to specify the characteristics of inner voids and reduce voids occurrence.

In this study, the resin samples processed by 3D printer are observed by X-ray computed tomography (see figure 1 (a)). Then, we investigate the morphological features such as the volume fraction, distribution, orientational order parameter and shapes of voids (see figure 1 (b)). The result is that voids are flat shape and parallel to in-plane direction. In addition, voids are aligned vertically at regular intervals. Furthermore, the surface shapes are also investigated (see figure 1 (c)), which reveals that the roughness of surface is different depending on polishing method. Based on the result of this study, we discuss the relationships between the morphological features and processing conditions.

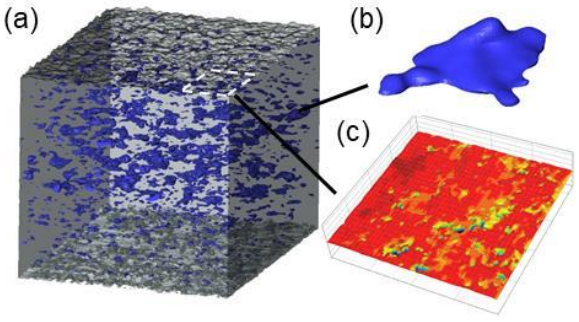

Fig. 1. 3D image of resin sample obtained by X-ray computed tomography; (a) overall; (b) void; (c) surface.

PM-15 **doi: 10.1093/jmicro/dfz096**

ZnO nanoparticles with fluorescent properties suitable for modification on protein surfaces.

Tetsuya Okuyama[1], Akinori Nakamura[2], Keisuke Ohta[3], Kiyoshi Matsuyama[4] and Hiroyuki Muto[5]

[1]Department of Materials System Engineering, National Institute of Technology, Kurume College, Fukuoka, Japan
[2]Advanced Engineering School, National Institute of Technology, Kurume College, Fukuoka, Japan
[3]Advanced Imaging Research Center, Kurume University. School of Medicine, Fukuoka, Japan
[4]Department of Life, Environment and Applied Chemistry, Fukuoka Institute of Technology, Fukuoka, Japan
[5]Department of Electrical and Electronic Information Engineering, Toyohashi University of Technology, Aichi, Japan

It has been clarified that ZnO nanoparticles having oxygen deficiency exhibit fluorescence emission with low energy, and application to fluorescent staining markers of living cells is expected, but there are no survey examples yet. We investigated ZnO nanoparticles with a fluorescence, which can be applied as a fine biomarker. It was found that the fluorescence wavelength of approximately 500 nm were ascribed to the oxygen deficiency in the nanoparticles. In addition, the fluorescence properties were related to the synthesis temperature and time, suggesting a strong correlation between the fluorescence intensity and the oxygen deficiency concentration in the particles. We tried the nanoparticle modification to the protein surface using ZnO nanoparticle with such oxygen defect. In present study, we selected a protein called streptavidin, which has a higher affinity with biotin, and tried to modify ZnO nanoparticles to such streptavidin and the immunogold method was applied to the modification of nanoparticles. ZnO nanoparticles suitable for surface modification were determined using TEM and XPS evaluation results as well as fluorescence properties. Modification to streptavidin was attempted using optimized ZnO nanoparticles. In the present study, the size of ZnO nanoparticles was too small to detect the fluorescence properties of the modified nanoparticles. Since highly visible fluorescence properties were confirmed in another experiment in which nanoparticles were dispersed in a resin with high biocompatibility, it is considered necessary to investigate the concentration of particles modified with streptavidin.

PM-16 **doi: 10.1093/jmicro/dfz095**

Fast Scanning Method Applicable as a Standard Acquisition Mode for SEM

Eisaku Oho[1], Kazuhiko Suzuki[2] and Sadao Yamazaki[1]

[1]Department of Electrical and Electronic Engineering, Faculty of Engineering, Kogakuin University, Tokyo, Japan
[2]Research & Development Center, Nohmi Bosai Ltd., Saitama, Japan

A fast scanning method, which drastically improves some serious disadvantages of SEM, is proposed for the SEM field. This method is developed to replace the conventional slow scan mode, which is used as a standard acquisition mode of SEM. Fast scan (e.g., TV scan) is generally coupled with frame-averaging (image integration), which is performed to reduce noise in SEM images. However, it is commonly believed that SEM images with a greater or lesser degree of blurring will probably be produced. This blur is mainly related to specimen deformation (drift) as well as the adverse effects of charging. In this kind of operation, a frame-averaging technique with position alignment is sometimes used to reduce image degradation (blur). This is fairly effective, but the obtained results are not as sharp as SEM images acquired in slow scan mode. Furthermore, the blurring of SEM images obtained from TV scan should be expected, even when the frame-averaging technique is not used, because the detector system has a serious problem with the frequency characteristics. Thus, to solve the problems and take advantage of the obvious merits of fast scanning, the frequency characteristics of TV scan have to be measured first and accurately compensated for. A properly designed inverse filter can be used for this purpose [1], which can preserve the structural details composed of one or a few pixels with an acceptable amount of image contrast in an SEM image acquired by TV scan. It is then necessary to estimate the appropriate number of images to accumulate for averaging, which probably depends on the properties of the specimen, SEM operating condition and performance of the position alignment. Hence, the quality of the desired signal (covariance) of the SEM signal is measured as frequently as necessary [2]. In this presentation, the final result from the TV scan mode will be sufficiently compared with the slow scan image.

1. E Oho and K Suzuki, SCANNING 31 (2009) 229‐235. 2. E Oho and K Suzuki, SCANNING 34 (2012) 43-50.

PM-17 **doi: 10.1093/jmicro/dfz097**

Noise removal for SEM images using a convolutional neural network

Kazuhiko Suzuki[1], Sadao Yamazaki[2] and Eisaku Oho[2]

[1]Research & Development Center, Nohmi Bosai Ltd., Saitama, Japan
[2]Department of Electrical and Electronic Engineering, Faculty of Engineering, Kogakuin University, Tokyo, Japan

A Convolutional Neural Network (CNN) is a powerful technique in the field of deep learning that has rapidly progressed. It is now effectively applied in many fields. In the field of microscopy, it has quite a few applications, mainly related to image recognition. Furthermore, a study on noise removal using a CNN has been successful in the field of image processing [1], demonstrating that it is not difficult to use a pre-trained network called a DnCNN (denoising CNN) in such applications. In the present study, to suppress white Gaussian noise in scanning electron microscope (SEM) images, the performance and properties of the noise removal method were evaluated based on the characteristics of the SEM images and instrument (e.g., blur, noise, charging phenomena, scanning speed, resolution.). A DnCNN-B used in the present study is equivalent to a DnCNN but has the advantage of being easy to use as a noise removal device. This is because noise can be removed even when the amplitude of the SEM image is unknown. However, to pre-train the DnCNN, a dataset was used that included widely varied natural images (e.g., sports, actions, people, animals, cities, landscapes), with most of the images showing clear details. However, the statistical properties of the images used for pre-training were not very similar to general SEM images; this pre-trained DnCNN would work best if the statistical properties of SEM images were similar to those in the training dataset. Thus, the important evaluation points to be discussed are as follows. 1) The influences of sharpness and the signal-to-noise ratio in an unprocessed SEM image on the noise removal. 2) The objective quality evaluation of the noise removed SEM images. 3) A comparison with other current noise reduction methods. 4) The use of transfer learning in this deep learning application, for which we will prepare a smaller number of suitable training SEM images.

1. K Zhang et al, IEEE Tran Image Proc 26 (2017) 3142-3155

PM-18 **doi: 10.1093/jmicro/dfz106**

Technology for fundamentally improving an extremely low-quality video signal used for fine focusing and astigmatism correction in scanning electron microscopy

Sadao Yamazaki[1], Kazuhiko Suzuki[2] and Eisaku Oho[1]

[1]Department of Electrical and Electronic Engineering, Faculty of Engineering, Kogakuin University, Tokyo, Japan
[2]Research & Development Center, Nohmi Bosai Ltd., Saitama, Japan

The current study describes important techniques for producing a series of video signals that can be used in fine focusing operation and near-perfect astigmatism correction in the field of scanning electron microscopy (SEM). These techniques can greatly enhance the stability of the signal used for focusing. As two especially important fundamental techniques, SEM image acquisition with greater importance given to the signal-to-noise ratio and signal reinforcement based on the concept of active image processing were fully utilized. It is expected that the proposed method can reduce the required operation time for fine focusing and enhance the stability of the signal. Moreover, the method is nearly completely robust against noise, allowing focus and astigmatism correction even for extremely noisy SEM images. The results of the study may be useful not only in the field of SEM but also all fields using weak signals.

Image processing techniques actually used in the present study were several types of conventional lowpass and highpass filters (the linear system). Although they may be considered obsolete technology, it was crucial for this research, which is conducted under a variety of SEM conditions, to make full use of their capabilities. In other words, these conventional techniques were suitable for this research, because it allowed for easy estimating of the degree of improvements those techniques provided, unlike the latest specific technologies. In this study, the performance of our method will be sufficiently tested as a support system for fine focusing and astigmatism correction using an auditory signal [1].

1. E Oho et al, Microscopy 66 (2017) 187–197.

PM-19 **doi: 10.1093/jmicro/dfz102**

Deep learning analysis of Si(111)-7x7 surface in atomic force microscopy

Keiichi Ueda[1,2] and Masayuki Abe[2]

[1]Dept. of Information Technology, Tokyo Metropolitan Industrial Technology Research Institute, Tokyo Japan, and [2]Dept. of Advanced Electronics and Optical Science, Graduate School of Engineering Science, Osaka University, Osaka Japan

Recent advances in deep neural networks recognize the detection of all objects in an image while also segmenting each instance[1]. Therefore instance segmentation is very important tool in image recognition.

The goal of our study is automation of atomic resolution measurement by using Atomic Force Microscopy (AFM), for that purpose, it is necessary to recognize individual atoms from the measurement image. In this report, we execute Mask-Rcnn that is one of the instance segmentation in AFM topographic image [Fig.1]. In Fig.1. circled prediction points as an atom and our neural networks got correct detection. In AFM measurement, even on the same surface, different images can be obtained depending on the tip and thermal drift, but our neural networks predict correct object. In our study, it is over 90% accuracy at Si (111)7x7 to predict Si atom. Furthermore, we discuss how to decide the atom position.

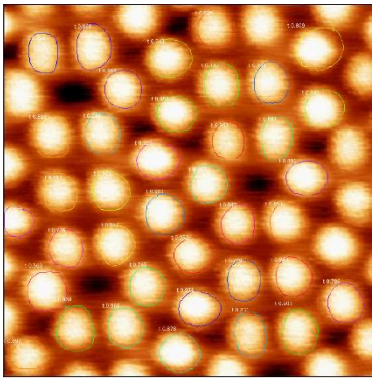

Fig. 1. Topography of Si (111)7x7 surface. Recognize Si atom by using Mask-Rcnn.

1. Kaiming He, Georgia Gkioxari, Piotr Dollar, Ross Girshick; The IEEE International Conference on Computer Vision (ICCV), 2017, pp. 2961-2969

PM-20 **doi: 10.1093/jmicro/dfz091**

Development of Software to Assist Contour Extraction of Objects from Electron Microscope Images Using Image Classification with Machine Learning

Gen Maeda[1], Misuzu Baba[2] and Norio Baba[1,2]

[1]Major of Informatics, Kogakuin University, Graduate School, Tokyo, Japan, [2]Research Institute for Science and Technology, Kogakuin University, Hachioji, Japan

Contour extraction of objects from electron microscope images is a theme that have been studied for a long time to eliminate complications of work in analyzing fine objects with transmission electron microscope. Recently this theme is regarded as an important method for segmentation of cross-sectional images obtained by electron CT, FIB-SEM and SEM array tomography method. We previously reported two methods about this theme. One is automatic classification of objects in electron microscope images with a machine learning method using 'Bag-of-Features' [1]. The other is contour extractions of them with a unique Gabor Wavelet analysis with the aid of a rough segmentation obtained from a result of the image classification, which estimates positions of their objects in the images [2].

We have further improved the above methods to more precisely extract contours effortlessly. Particularly, the training data was refined in the Bag-of-Features analysis, some preprocessings were applied to the original images, and the methods of searching for contour points and of tracing its line were improved sophisticatedly optimizing the needed parameters, where the parameters were changed according to differences of the characteristics regarding the contour of each object and structure. In the present stage, our software can extract contours in 2D (in an image) only. In the future, it will be expanded to 3D contour extraction.

1. Gen Maeda et al, Microscopy Vol.64 No.S1 (2015) p.i142.
2. Gen Maeda et al, Microscopy and Microanalysis Vol.23 No.S1 (2017) pp.138-139.

PM-21 **doi: 10.1093/jmicro/dfz086**

Optimization of hyperparameters in dictionary learning algorithm for peak detection of atom-resolved scanning transmission electron microscope images

Sosuke Hattori[1], Yuki Nomura[2] and Koh Saitoh[1]

[1] Department of Applied Physics, Nagoya University, Nagoya, Japan, [2] Panasonic Corporation, Kadoma, Japan

Recently, compressed sensing techniques that obtain true signals from a small amount of information has attracted much attention [1]. We propose a method to optimize hyperparameters of dictionary learning algorithm for denoising high-resolution scanning transmission electron microscopy (STEM) images with atom displacements.

In order to evaluate atom displacements from STEM images by dictionary learning, we simulated atom-resolved STEM images from crystal structures with atom displacements. Poisson noise and Gaussian noise were added to the simulated image. For determining hyperparameters such as the size of the dictionary patches and the number of dictionaries, cross-validation based on minimizing the residual sum of squares of atom positions was used instead of the residual sum of squares of the image intensity. In addition, the standard was weighted so that the number of displaced atoms can be considered at the same ratio to the number of atoms in the basic structure. Dictionary learning is performed using parameters obtained based on this standard. Fig. 1(a) and 1(b) are a noise image and a reconstructed image. In the presentation, we will show the limit of reproducibility of the atom displacements with respect to noise based on this standard.

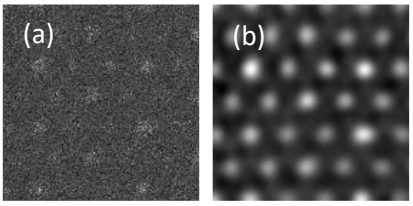

Fig. 1(a)Original image, (b)Reconstructed image.

1. A. Stevens et al, Microscopy (2014) 41.

PM-22 **doi: 10.1093/jmicro/dfz089**

Surveillance study on the SI-traceable nanometrology by transmission electron microscopy (TEM) and trial fabrication of reference materials for TEM

Keita Kobayashi

National Metrology Institute of Japan, National Institute of Advanced Industrial Science and Technology (AIST), Tsukuba, Japan

Recent miniaturization of nanodevices makes us expect that nanometrology for accurate machining and control at the sub-nanometer scale must be required in the next decade [1]. Transmission electron microscopy (TEM) is a powerful method for observation of sub-nanometer scale structure, and is, therefore, considered to be integral to the nanometrology. Therefore, considerable efforts to establish traceability to the SI for dimensional nanometrology by TEM have been being dedicated [2]. Since lattice parameters of bulk Si have been measured by x-ray interferometry traceable to SI [3], the lattice spacings have been considered as SI-traceable references [1]. These previous researches, therefore, applied the lattice spacings of Si processed to thin film for TEM observation as SI-traceable references [1]. In the previous studies, the lattice spacings of processed Si thin film were considered to be same as those of bulk Si. However, since the lattice parameter can be varied due to the sample processing, the lattice spacings should be measured by other method traceable to SI. Based on the above, the author proposes TEM calibration using atomic-layered materials measured their lattice spacing by metrology atomic force microscope [4].

1. A. Yacoot, U. Kuetgens and E. Massa, CCL-GD-MeP-1, version 1.0 (2019).
2. R. Dixson and H. Bosse, CCL-GD-MeP-2, version 1.0 (2019).
3. E. Massa, et al., New J. Phys., **11** (2009) 053013.
4. S. Gonda, et al., Rev. Sci. Instrum., **70** (1999) 3362.

PB-01 **doi: 10.1093/jmicro/dfz084**

Comparison of the fundamental cell morphological properties examined with whole-mount ice-embedded cryo-TEM between 5 genera in family *Mycobacteriacea*.

Hiroyuki Yamada[1], Kinuyo Chikamatsu[1], Akio Aono[1], Kazuyoshi Murata[2], Naoyuki Miyazaki[2], Yoko Kayama[3], Nagatoshi Fujiwara[4], Shinji Maeda[5], Satoshi Mitarai[1, 6]

[1] Department of Mycobacterium Reference and Research, the Research Institute of Tuberculosis, Japan Anti-Tuberculosis Association, Tokyo, Japan, [2] National Institute for Physiological Sciences, National Institutes of Natural Sciences, Aichi, Japan, [3] Terabase, Inc, Aichi, Japan, [4] Department of Food and Nutrition, Faculty of Contemporary Human Life Science, Tezukayama University, Nara, Japan, [5] Department of Life Science, Faculty of Pharmaceutical Sciences, Hokkaido University of Science, Hokkaido, Japan, [6] Department of Basic Mycobacteriology, Graduate School of Biomedical Science, Nagasaki University, Nagasaki, Japan.

Genus *Mycobacterium* belonging to the family *Mycobacteriaceae* has been divided into an emended genus *Mycobacterium* and four novel genera, *Mycolicibacterium*, *Mycolicibacter*, *Mycolicibacillus*, and *Mycobacteroides* [1]. Bacilli in 22 species containing 25 strains in these genera were cultured with a liquid medium, and the bacterial cells were fixed with 2.5 % glutaraldehyde and rinsed with phosphate buffer. Bacterial cells were quickly frozen and examined. TEM Images of more than 1,000 cells were analyzed with Fiji/ImageJ. Diameter, length, perimeter, circularity and aspect ratio of the single cells were measured and the differences between the genera were compared. The average diameters of the cells were similar, ranging from 0.51 to 0.65 μm. However, the average diameter of the cells in genus *Mycolicibacterium* was significantly larger than those of the other 4 genera ($p<0.001$). There were significant differences in the average cell length between the genera, ranging from 1.43 to 3.46 μm, where the shortest and the longest length of all cells were 0.77 μm and 8.58 μm, respectively. *Mycolicibacterium* and *Mycobacterium* contain species with varied morphological properties, further subdivision into novel genera may be done in the future.

[1]. H Yamada *et al*., Front. Microbiol. 9 (2018) 1992. doi: 10.3389/fmicb.2018.01992

PB-02 **doi: 10.1093/jmicro/dfz079**

Observation of influenza virus particles by ultra-high resolution scanning electron microscope

Tomoki Nishida[1], Eri Nakajima[1], Yasuo Imoto[1], Satoshi Seino[2]

[1] Microbial Testing Laboratory, Japan Textile Products Quality and Technology Center, Hyogo, Japan
[2] Management of Industry and Technology Graduate School of Engineering, Osaka University, Osaka, Japan

Electron microscopy is one of the powerful tool for direct visualization of influenza viruses at nanometer resolution. In research and diagnosis, transmission electron microscopy (TEM) is widely used to study of virus structure. On the other hand, observation of influenza virus by scanning electron microscope (SEM) is far less frequently than TEM. In this study, we aimed to three-dimensional observation of the influenza virus surface by ultra-high resolution SEM. Madin-Darby Canine Kidney (MDCK) cells (ATCC, CCL-34) that were cultured on glass coverslips were inoculated with 0.1 mL of influenza A/Hong Kong/8/68 (H3N2) (ATCC, VR-1678) diluted with serum-free medium to $1–5 \times 10^4$ pfu/ mL. After 24 and 48 hours post-infection, infected cells were fixed with 2.5% glutaraldehyde in phosphate buffer, and post-fixed in 1% osmium tetroxide. After dehydration with a series of ethanol, samples were dried by critical point drying (JCPD-5, JEOL, Japan) and then coated with osmium. The surface of H3N2 virus particles were examined using field-emission SEM (S-5200, Hitachi, Japan). After 24 hour post-infection, the particles of budding H3N2 virus on the cell surface mainly showed the spherical, filamentous and the rod-shaped structures. Moreover, the villous or ridge shaped patterns with many fine protrusions was found on the surface of these H3N2 virus. In addition, after 48 hours post-infection, virus particles were found on the cell-free vacant areas on the substrate. These single virus particles obtained without a purification step such as ultracentrifugation may be help the visualization for the surface structure of viruses by chemical disinfection or physical sterilization.

PB-03 **doi: 10.1093/jmicro/dfz070**

Visualization of Compacted DNA of *Synechococcus elongatus* PCC7942 by DRAQ5 Labelling with DAB Photooxidation.

Ilika Ghosh[1], Kimie Atsuzawa[2], Aoi Arai[3], Ryuzo Ohmukai[3] and Yasuko Kaneko[1,3]

[1]Graduate School of Science and Engineering, Saitama University, Saitama, Japan, [2]Comprehensive Analysis Center for Science, Saitama University, Saitama Japan, and [3]Faculty of Education, Saitama University, Saitama, Japan

Transient DNA compaction occurs during cell division cycles of *S. elongatus* culture under light/dark cycles (Fig. 1a). The 3D bulk ultrastructure of the compacted DNA has been visualized by high-voltage cryo-electron tomography [1]. In order to further investigate the detailed structure of DNA during compaction, we used DNA binding DRAQ5, which is a membrane permeable, torsional elasticity dependent, minor groove binding and far red emitting anthraquinone dye [2]. The presence of compacted DNA was confirmed by fluorescence microscopy after staining of live cells with DRAQ5 for 1h (Fig 1b). This was followed by fixation in glutaraldehyde (1 h) and laser excitation (633 nm) in a petri dish (1 h) of the DRAQ5-labelled cells to release singlet oxygen in the presence of DAB. Light microscopic observation revealed dark DAB stained portions within the DRAQ5-labelled cells (Fig 1c), possibly indicating the presence of the compacted DNA. The samples were further treated with osmium tetroxide to form osmium black and processed for TEM observation.

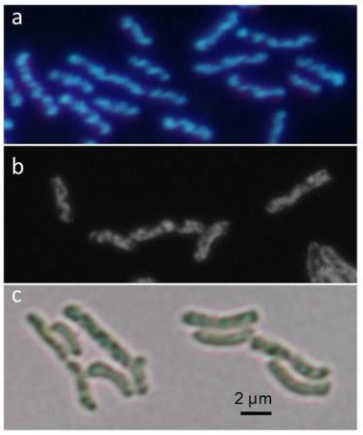

Fig. 1. *S. elongatus* DNA stained with Hoechst 33342(a), DRAQ5(b) and DAB(c).

1. K Murata et al, Scientific Reports 6:34934 (2016) DOI: 10.1038/srep34934.
2. HD Ou et al, Science 357: 6349 (2017) DOI: 10.1126/science.aag0025.

PB-04 **doi: 10.1093/jmicro/dfz077**

Electron micrographic analyses of the fine structure and properties of biodegradable plastics granules produced by microbes.

Hazuki Minami, Chihiro Fujiwara, Nozomi Seto, Michio Sato, and Michihisa Maeda

School of Agriculture, Meiji University, Kawasaki, Japan

Bacteria store carbon sources down the road as polyesters under the condition of unsuitable for growth. The polyesters are referred to as polyhydroxyalkanoates (PHAs) and known as “biodegradable” plastics. In our laboratory, the system producing environment-friendly PHAs from the environmental pollutants such as PCBs by a single-step process, is going on constructing. To provide higher efficiency (for production) and greater value (for products) to the system, we have characterized fundamental mechanisms. We have investigated in detail individual functions and the capacity of metabolic pathways provided by the cells because the balance among polymerizing enzymes, granule stabilized proteins and depolymerizing enzyme is important. We report here electron microscopic analyses of the PHA granules produced by the mutants of 3 each factor.

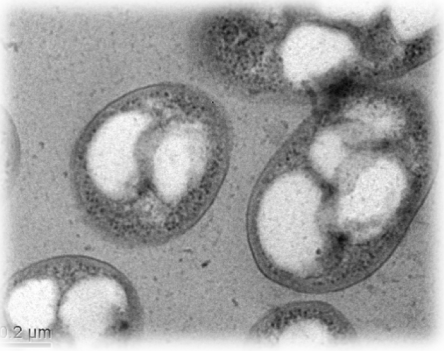

Fig. 1. PHA granules accumulated in the microbial cells

PB-05

doi: 10.1093/jmicro/dfz082

Recycling of Uranyl acetate solution.

Hiroshi Takase [1,2], Makoto Sugiura-Nakazato [3]

[1] Core Laboratory, Nagoya City University Graduate School of Medical Sciences, Nagoya, Japan, [2] Department of Pathology and Molecular Diagnostics, Nagoya City University Graduate School of Medical Sciences, Nagoya, Japan and [3] Section of Biostructural Science, Graduate School of Medical and Dental Sciences, Tokyo Medical and Dental University, Tokyo, Japan

Uranyl acetate has been widely used for electric staining of ultrathin section and negative staining. Because of radioactivity of the wasted reagents, discarding of Uranyl acetate is commonly prohibited. Furthermore, it is difficult to obtain this reagent these days. In this study, we prepared wasted reagent containing impurities made by mixing Uranyl acetate solution and supernatant of culture medium assuming the presence of protein. The wasted reagent was filtered through membrane filter followed by precipitation with ammonia. Then the precipitate was dissolved by adding acetic acid. The performance of negative staining was compared with the presence or absence of impurities.

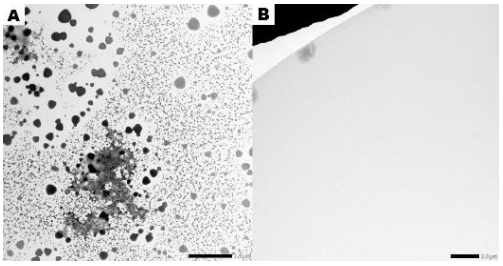

Fig. 1. Comparison between the presence and absence of impurities in Uranyl acetate solution (A) Uranyl acetate solution mixed with used medium for cell culture before purification. (B) Uranyl acetate solution after purification.

PB-06

doi: 10.1093/jmicro/dfz075

Advanced microbeam irradiation system for single cell analysis of defensive cellular response against radiation

Teruaki Konishi[1], Daisuke Ohsawa[1], Alisa Kobayashi[1], Masakazu Oikawa[1]

[1]Single Cell Radiation Biology Group, Institute for Quantum Life Science, National Institutes for Quantum and Radiological Science and Technology, Chiba, Japan

Advanced microbeam irradiation system made possible to deliver a defined amount of radiation on a single cell with a few micrometer resolution. Our microbeam, the Single-Particle Irradiation system to CEll (SPICE) provides a 3.4 MeV proton microbeam focused with a quadrupole magnetic lens on an upward vertical beam line (1,2). SPICE is the only proton microbeam in Japan that can target nucleus, cytoplasm, or both with high throughput, high targeting accuracy along with promising stability. In this presentation, the state of the art features of SPICE will be introduced along with our recent results from single cell analysis of microbeam targeted cells on defensive signalling through intra- and inter-cellular response against radiation, such as cytoplasmic damage response (3,4), and cell-to-cell communication between human normal and carcinoma cells (5-7).

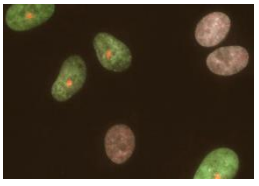

Fig. 1. Only the nucleus of A549 carcinoma cells (green) that were co-cultured with WI-38 normal cells (white) were microbeam irradiated with 500 protons. Red spots indicate the DNA double strand break region immuno-stained against γ-H2AX.

1. T. Konishi, et al., J Radiat Res 54(2013) 736-747.
2. D. Ohsawa, et al., Nucl Instrum Methods Phys. Res B 453 (2019) 9-14.
3. J. Wang and T. Konishi, Cancer Sci, 110 (2019) 686-696.
4. T. Konishi, et al., J. Radiat Cancer Res 9 (2018)183-189.
5. A. Kobayashi, et al., Radiat Prot Dosim 183 (2019) 142-146.
6. N. Autsavapromporn, et al., Radiat Res 191 (2019) 211-216.
7. A. Kobayashi, et al., Mutat Res-Fund Mol M 803-805 (2017) 1-8.

PB-07 **doi: 10.1093/jmicro/dfz074**

Organelle detection from electron microscopic images by deep learning

Kei Kato[1], Yoshiaki Shinohara[2], Takatoshi Ueki[1], and Nobuhiko Ohno[2]

[1] Department of Integrative Anatomy, Graduate School of Medicine, Nagoya City University, Nagoya Japan
[2] Division of Histology and Cell Biology, Department of Anatomy, Jichi Medical University, Shimotsuke, Japan

The recent advancement in electron microscopic volume imaging has enabled rapid collection of many serial electron microscopic images in a short period of time. However, analyses of the huge datasets frequently require heavy burden of manual image segmentation, and it is obvious that we need new approaches for the efficient analyses. To overcome the problem, we tested automated method for organelles detection from electron microscopic images, and evaluated the usefulness as follows. 1) First, serial image data of mouse corpus callosum acquired by serial block-face scanning electron microscopy were separated into 900 learning and 450 test data sets. 2) The original imaging data were binned into 128 x 128 pixels data, and nuclei were chosen as the target organelle of detection. To improve detection accuracy, some part of nuclei was included in each image of the learning data set. 3) We used CNNs of repeated convolution and max-pooling layers, followed by deconvolution and dropout layers. After automated segmentation, we evaluated the error rates of the CNNs from data sets unused for learning. Evaluations of multiple CNN models were performed by changing i) numbers of convolution layers of the CNN (4-5 layers), ii) width of convolution windows (3x3 to 5x5 pixels) iii) feature numbers (16 or 32). Our preliminary data suggested that in the most cases, the error rates were 0.02-0.03, and widths of the convolution layers are likely to be the most important factor for correct segmentaion, although there were not so much differences between the models. The low error rates indicate that this method is promising for automated organelle detection, and we are planning to optimize the method to 3D volume data and detection of other kinds of organelles.

PB-08 **doi: 10.1093/jmicro/dfz083**

SEM analysis of long-term coenzyme Q10 deficient cell model

Tsukika Tanaka[1], Michio Sato[2], Mizuho Okamoto[1], Akari Nakamura[1], Akio Fujisawa[1], Yorihiro Yamamoto[1], Misato Kashiba[1].

[1]Tokyo University of Technology, [2] Meiji University, JAPAN.

Coenzyme Q10 (CoQ10) is a key component of the mitochondrial electron transfer chain and is one of the most important antioxidants. Cellular CoQ10 level has been reported to decrease in aging. Several diseases are associated with low CoQ10 levels. To elucidate the physiological relevance of CoQ10, we established long-term CoQ10 deficient cell model by the administration of CoQ10 biosynthesis inhibitor, 4-nitrobenzoate (4-NB). We cultured HepG2 cell line more than two years in the medium with 4-NB (Chronic 4-NB cell). We also produced a cell model with administration of 4-NB only for 3-day (Acute 4-NB cell).

SEM analysis revealed that cell surface conditions with Chronic 4-NB cell is different from that with control HepG2 cell. Acute 4-NB cell exhibited more pseudopod.

These results show that cellular CoQ10 is important to maintain normal cell surface condition.

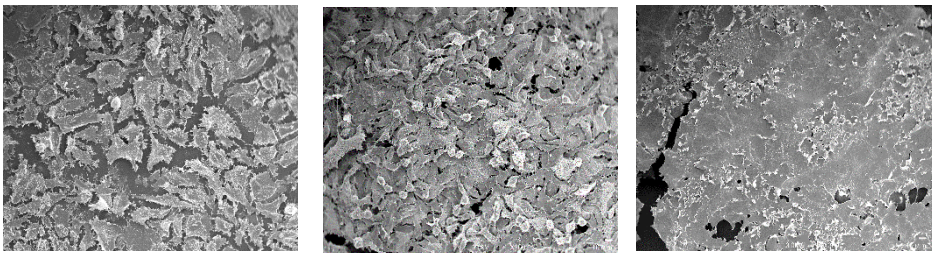

Control Acute Chronic

Fig1.SEM analysis of 4-NB treatedcell lines

PB-09 **doi: 10.1093/jmicro/dfz073**

Visualization of F-Actin with Fascin in Filopodia by Cryo-Electron Tomography

Naoko Kajimura[1], Shota Inagaki[2], Takuo Yasunaga[3] and Kaoru Mitsuoka[1],

[1]Research Center for Ultra-High Voltage Electron Microscopy, Osaka University, Ibaraki, Japan, [2]Graduate School of Engineering, Osaka University, Suita, Japan, [3]Graduate School of Computer Science and Systems Engineering, Kyushu Institute of Technology, Iizuka, Japan

Fascin is an F-actin-bundling protein that stabilizes cell protrusions, such as filopodia, in migrating and metastatic cells. In the process of neural circuit formation, the growth cone functions as an antenna for detecting axonal guidance factors present around cells. Thus, understanding the interaction mechanism between F-actin and fascin is important.

Cryo-electron tomography (cryo-ET) and subtomogram averaging allow visualizing macromolecular complexes in the physiological conditions at a resolution which enables a docking of the atomic model to the structure. Previously, the structure of the F-Actin with fascin in filopodia was visualized[1], but recent improvement of this technique could improve the resolution of structural analysis. Here we applied this technique to visualize *in situ* structure of F-actin with fascin using a neuronal model cell (NG108-15) and report the improved structure of F-actin and fascin complex by subtomogram averaging using RELION[2] (**Fig. 1**).

Fig. 1. Structure of F-actin with Facin in NG108-15 cell

1. S. Aramaki et al., Cytoskeleton 73 (2016). 365-374...
2. T. A. Bharat and S. H. Scheres, Nature Protocols 11 (2016) 2054-2065.

PB-10 **doi: 10.1093/jmicro/dfz085**

High-pressure freezing method can be replaced by sandwich freezing method !?: electron microscopy of human tissues and cultured cells.

Masashi Yamaguchi[1], Seiichiro Wakabayashi[2], Yuumi Nakamura[2], Hiroyuki Matsue[2], Takuya Hirao[3, 4], Shigeki Aoki[3], Hiroyuki Yamada[5], Nobuya Mamizu[6], Hiromitsu Furukawa[6], Hiroji Chibana[1]

[1]Medical Mycology Research Center, Chiba University, 1-8-1 Inohana, Chuo-ku, Chiba 260-8673, Japan, [2] Department of Dermatology, Chiba University Graduate School of Medicine, Chiba, Japan, [3] Laboratory of Biopharmaceutics, Graduate School of Pharmaceutical Sciences, Chiba University, Chiba, Japan, [4] Department of Pharmaceutical Sciences, International University of Health and Welfare, Ohtawara, Tochigi, Japan, [5] The Research Institute of Tuberculosis, JATA (Japan Anti-Tuberculosis Association), Tokyo, Japan, [6] System in Frontier Inc., Tachikawa-shi, Tokyo, Japan

Rapid freeze-freeze substitution of living yeast cells by sandwich freezing has been used for observing clear and natural ultrastructure of cells [1]. Rapid freeze-freeze substitution of glutaraldehyde-fixed cells of bacteria and other microorganisms by sandwich freezing also yielded clear and natural ultrastructure [2]. Here, we have applied sandwich freezing followed by freeze substitution to observe human cells and tissues. We found that clear and natural cell images were obtained by sandwich freezing and freeze-substitution of glutaraldehyde-fixed tissues sliced to 0.2 mm thickness. This is a remarkable result because, in the past, tissues as thick as 0.2 mm could only be frozen by high-pressure freezing. The present study has made it possible to observe clear and natural cell structures in animal and human tissues anytime because glutaraldehyde-fixed tissues can be stored at 4 °C for several months before rapid freezing. Also, natural ultrastructure of cultured cells in suspension was found to be observed more clearly by sandwich freezing and freeze substitution of glutaraldehyde-fixed cells than rapid freezing and freeze substitution of living cells. The present method should be used as a standard method to observe clear and natural ultrastructure of animal and human tissues.

[1] M Yamaguchi et al, J Electron Microscopy 58 (2009) 261-266 . [2] M Yamaguchi et al, J Electron Microscopy 60 (2011) 283-287
.

PB-11 **doi: 10.1093/jmicro/dfz076**

3D-Modeling of Arabidopsis Root System Architecture by X-ray Micro-CT at SPring-8: Observation at Different Experimental Hutches

Tomofumi Kurogane[1], Daisuke Tamaoki[2], Sachiko Yano[3], Fumiaki Tanigaki[3], Toru Shimazu[4], Haruo Kasahara[3], Daisuke Yamauchi[5], Kentaro Uesugi[6], Masato Hoshino[6], Seiichiro Kamisaka[2], Yoshinobu Mineyuki[5], Ichirou Karahara[2]

[1]Graduate School of Science and Engineering for Education, University of Toyama, Toyama, Japan, [2]Graduate School of Science and Engineering, University of Toyama, Toyama, Japan, [3]Japan Aerospace Exploration Agency, Tsukuba, Japan, [4]Japan Space Forum, Tokyo, Japan, [5]Graduate School of Life Science, University of Hyogo, Himeji, Japan, [6]Japan Synchrotron Radiation Research Institute, Sayo, Japan

To reveal effects of environmental changes on the development of plant root systems, we have attempted 3D visualization of roots of *Arabidopsis thaliana* (L.) Heynh. grown and dried in rockwool using X-ray refraction-contrast micro-CT at the beamline BL20B2 (25 keV) of SPring-8[1]. Roots were modeled in 3D using IMOD software (http://bio3d.colorado.edu/imod/) from reconstructed volumes. Offset scanning at Hutch 3 (25.5 μm / pix) enabled reconstruction of almost the entire region of a rockwool slab (60 × 60 × 20 mm) and provided an overview of the distribution of root systems. Observation at Hutch 1 (2.75 μm / pix) and reconstruction of regions of 5 × 5 × 10 mm enabled discrimination of finer roots and rockwool fibers.

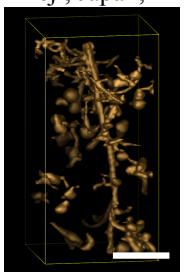

Fig. 1. 3D surface model of an Arabidopsis root constructed by using a software IMOD (Hutch1 data). Bar = 200 μm.

1. T Kurogane et al., Microscopy 67 (2018) i34.
The synchrotron radiation experiments were performed at the BL20B2 of SPring-8, with the approval of the JASRI (Proposal Nos. 2014B1225, 2015B1556 and 2017B1225, 2018B1182 and 2019A1130).

PB-12 **doi: 10.1093/jmicro/dfz078**

In Vivo Time-lapse Imaging of Changes in Air Space Distribution during Seed Imbibition in *Lotus miyakojimae* using X-ray Micro-CT

Yoshinobu Mineyuki[1], Daisuke Yamauchi[1], Tomonori Nakai[1], Daisuke Tamaoki [2], Kentaro Uesugi[3], Makoto Hoshino[3] and Ichirou Karahara[2]

[1]Graduate School of Life Science, University of Hyogo, Himeji, Japan, [2]Graduate School of Science and Engineering, University of Toyama, Toyama, Japan, [3]Japan Synchrotron Radiation Research Institute, Sayo, Japan

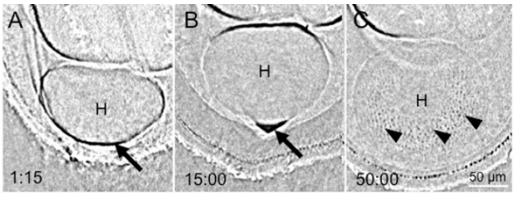

Fig. 1. Changes in the void space in and around the hypocotyl (H) of a *Lotus .miyakojimae* seed during early imbibition. CT images were obtained at 1 min 15 sec (A), 15 min (B), and 50 min (C) after the start of image acquisition. Arrows, void spaces; arrowheads, intercellular spaces.

Although 3D distribution of air spaces inside seeds can be detected *in vivo* using X-ray micro-computed tomography (CT) [1,2], where the source of the air that gets trapped in those intercellular spaces during imbibition remains unknown. To resolve this question, we observed seed imbibition processes continually using the BL20B2 beamline at the SPring-8 facility. A seed of *Lotus miyakojimae* in a filtered-pipette tip containing distilled water was set on the sample stage and was rotated (0.4 rpm) continually for 90-min. A series of 21,600 images with an effective pixel size of approximately 2.75 μm was acquired and 72 time-lapse tomograms were reconstructed. Results showed the appearance of intercellular spaces in the embryo after the disappearance of the void spaces around the embryo in the imbibed seed suggesting that the air was taken up from outside to the embryo during imbibition.

1. Y Mineyuki, Microscopy 63 (2014) Suppl 1: i8-i9.2., 2. D Yamauchi et al, Microscopy 62 (2013) 353-361. The synchrotron radiation experiments were performed at the BL20B2 of SPring-8, with the approval of the the JASRI (Proposal Nos. 2017B1225, 2018B1182and 2019A1130).

PB-13 **doi: 10.1093/jmicro/dfz071**

Three-dimensional ultrastructural analysis of bone-resorbing osteoclasts by Correlative Light Electron Microscopy (CLEM) and Focused Ion Beam Scanning Electron Microscope (FIB-SEM) suggested novel functions of osteoclasts

Masahiro Hosonuma[1,2,3], Nobuhiro Sakai[1], Takashi Takaki[4], Hideki Matsushima[5], Akira Takebe[6], Yuji Kiuchi[2] and Masamichi Takami[1]

Departments of [1]Pharmacology at School of Dentistry and [2]Pharmacology at School of Medicine in Showa University, [3]Division of Rheumatology at Department of Medicine in Showa University School of Medicine, [4]Section of Electron Microscopy in Showa University, [5]JEOL Ltd. and [6]JEOL-Nikon CLEM Solution Center.

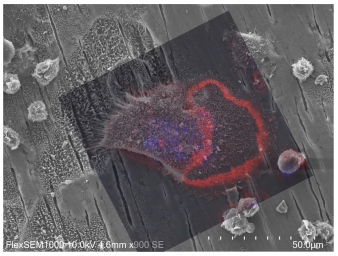

Fig. 1. Detection of actin ring in osteoclasts by CLEM.

Osteoclasts are highly polarized cells that form ring-like structure of actin (called "actin ring") inside cells and ruffled borders (RB) toward the bone surface during bone resorption. However, the precise functions of these structures are unknown. Using CLEM (Nikon: A1, NIS-Elements, HITACHI: FlexSEM 1000) and FIB-SEM (JEOL: JIB-4700F), we analyzed three-dimensional structure of actin ring and ruffled borders of bone-resorbing osteoclasts cultured on dentin slices. Analysis by CLEM revealed that most of actin-ring localized at cell portion of the direction of movement (actin-ring area), which is attached on the undecalcified area and edge of decalcified area (lacunae) (Fig. 1). On the other hand, analysis by FIB-SEM (pitch: 150 nm or 10 nm) indicated that non-actin ring area consists of much more amounts of ruffled boarders and cytosol that contains nuclei, mitochondria and vacuoles compared to the actin ring area. These results suggest a novel concept of the roles of actin ring such as sensing of unmineralized area of bone and towing the whole cell body toward there.

PB-14 **doi: 10.1093/jmicro/dfz081**

Effect of smoking inflammatory response to smoking cessation on human gingival fibroblast and periodontal ligaments cells.

Toshiaki Tachibana[1], Hiroko Igarashi-Takeuchi[1,2], Yukihiro Numabe[2]

1 Core Research Facilities for Basic Science, Research Center for Medical Science, The Jikei University School of Medicine
2 Department of Periodontology, School of life Dentistry at Tokyo, The Nippon Dental University

The purpose of this study was to evaluate that human gingival fibroblast and periodontal ligaments cells's smoking inflammatory response and changes in repair period during smoking cessations.

Both cells were obtained from healthy periodontal tissue. When cells were cultured until confluence, medium was replaced 1μg/ml nicotine contained medium for 24 hours. Then cells were washed by medium replaced non-nicotine fresh medium until 48 hours.

After stimulation of nicotine and replaced medium, level of IL-6 was significantly increased in both cells ($p<0.001$). Smoking group were significantly decreased comparing with control group and smoking cessation group ($p<0.001$). The surface of cell membrane was crumpled by SEM.

Our study demonstrated the cells damaging effect of smoking. On the other hands, actually damage of smoking was still remained in cells. We also indicated ability of the cell repairing effect of smoking cessation.

This work was supported by Grant-in –Aid for Young Scientists (B) Grant number 16k20681 from the Japan Society for the promotion of Science.

PB-15 **doi: 10.1093/jmicro/dfz072**

Morphological Analysis of Reticular Dermis of Human Keloid Tissue

Shizuko Ichinose, Chiemi Kaku, Rei Ogawa

Department of Plastic, Reconstructive and Aesthetic Surgery, Nippon Medical School Hospital, Tokyo, Japan

Keloid is a fibroproliferative disorder of the skin caused by abnormalities in the wound healing process of the damaged or stimulated dermis. As inflammation continues in the dermal reticulated layer, blood vessels increase and proliferate, collagen fibers accumulate, and the corresponding region become red and swelled [1]. To elucidate the etiology of this fibroproliferative disease, many studies have been conducted, including gene expression and biochemical analysis. But the onset mechanism is not clear, and treatment has not been established yet. In this study we have investigated keloidal collagen (KC) area (hyalization area) of the dermal reticular layer from the morphological point of view by light and transmission electron microscopy and immunohistochemical examination. The KC was actually different from ordinary collagen produced by normal fibroblasts: the particle varies in both size and shape in each interval and they are crushed and fused. There were myofibroblasts around the KC, rich in actin fibers and characterized by a dense body at the cell edge and αSMA-positive. Myofibroblasts around the KC produced KC-specific collagenous fibers. Many blood vessels around the KC were present too. The presence of the myofibroblasts and blood vessels around the KC to contribute development of KC and hyalization.

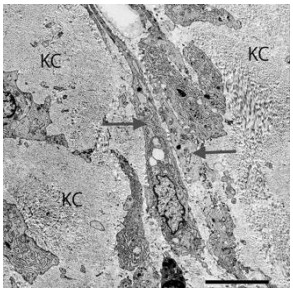

Fig. 1. TEM image of myofibroblasts (arrows) around the KC. Scale bar=5 μ m.

1. Ogawa R. Int J Mol Sci. 2017,18,606-615.

PB-16 **doi: 10.1093/jmicro/dfz080**

Detection of Diatoms from the Viscera for the Diagnosis of Drowning by Using SEM.

Tsubasa Sakamoto[1], Hiroshi Takase[2], Mimiko Fukuta[1], Yasuhiro Aoki[1],

[1]Department of Forensic Medicine, Nagoya City University Graduate School of Medical Sciences, Nagoya, Japan.[2]Department of Pathology and Molecular Diagnostics, Nagoya City University Graduate School of Medical Sciences, Nagoya, Japan.

Diatom test is known as a method that forensic scientists often used for examining diatoms, under the optical microscope, contained in major organs to determine whether the cause of death of immersion remains is drowning. The aim of this study was to examine whether SEM is useful for observing diatoms in cadaveric liver, which appears to be drowned. The pig liver was immersed with seawater, left at room temperature for three days. Ten gram of the liver was digested by three different methods; fuming nitric acid and sulfuric acid, fuming nitric acid and hydrogen peroxide, and proteinase K. After the digestive step, sample was diluted with pure water and passed through a cellulose filter. The filter was observed and compared under the optical microscope and SEM. As a result, SEM enabled detailed morphological observation of diatoms, some of which were difficult to observe by the optical microscope. In SEM observation, it is possible to discern even broken diatoms attached to organic materials, although manual SEM operation may take longer. As a future prospect, by developing auto-scan and image recognition by deep learning, it can be expected to increase its viability.

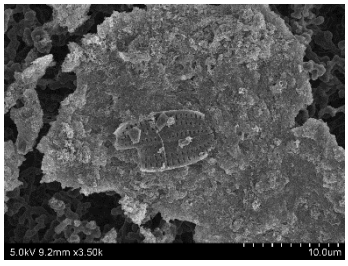

Fig. Diatom buried in residue, which was considered difficult to observe with an optical microscope.

Author Index

Abe, M.	PM–19
Adachi, Y.	SM–6
Ajioka, F.	SM–6
Amino, N.	SM–2
Anada, S.	SM–4
Aoki, S.	PB–10
Aoki, Y.	PB–16
Aono, A.	PB–01
Aono, M.	PM–06
Arai, A.	PB–03
Asari, Y.	SM–3
Aso, K.	PM–11
Atarashi, A.	PM–01
Atsuzawa, K.	PB–03
Baba, M.	PM–20
Baba, N.	PM–20
Chen, C.	SS1–4
Chibana, H.	PB–10
Chikamatsu, K.	PB–01
Cretu, O.	K–4
Elewa, Y.H.A.	KA–1
Enya, K.	SM–6
Fujisawa, A.	PB–08
Fujiwara, C.	PB–04
Fujiwara, N.	PB–01
Fukushima, K.	K–1
Fukuta, M.	PB–16
Furukawa, H.	PB–10
Ghosh, I.	PB–03
Hagita, K.	PM–12, SM–5
Haruta, M.	LS–1
Hasegawa, K.	SS2–4
Hashimoto, S.	PM–06
Hattori, S.	PM–21
Hayashi, A.	PM–01
Higaki, T.	SB–4
Hiramoto, H.	SS2–4
Hirao, T.	PB–10
Hirayama, H.	SS1–4
Hirayama, T.	SM–4
Hirayama, Y.	PM–07
Honda, A.	SS2–4
Horide, T.	PM–07
Hoshino, M.	PB–11, PB–12
Hosonuma, M.	PB–13
Ichii, O.	KA–1
Ichinose, S.	PB–15
Igaki, E.	SM–4
Igarashi-Takeuchi, H.	PB–14
Ikuhara, Y.	PM–03
Imoto, Y.	PB–02
Inagaki, S.	PB–09
Ishida, K.	SS2–4
Ishikawa, S.	SB–5
Ishimaru, M.	PM–07
Ishimura, T.	SC–1
Ishizuka, K.	K–4
Itoh, H.	SS2–4
Ito, T.	PM–05
Iwaya, K.	SS2–3
Jinnai, H.	PM–12
Kajimura, N.	PB–09
Kaku, C.	PB–15
Kamimura, I.	SC–1
Kamisaka, S.	PB–11
Kaneko, N.	PM–14
Kaneko, Y.	PB–03
Karahara, I.	PB–11, PB–12
Kasahara, H.	PB–11
Kashiba, M.	PB–08
Kato, K.	PB–07
Kato, Takashi	PM–02
Kato, Takayuki	SS1–3
Kayama, Y.	PB–01
Kikkawa, J.	K–4
Kimoto, K.	K–4
Kinoshita, A.	PM–03
Kiuchi, Y.	PB–13
Kobayashi, A.	PB–06
Kobayashi, Kei	SS2–2
Kobayashi, Keita	PM–22
Kobayashi, S.	KA–2
Koizumi, K.	PM–10
Kondo, K.	PM–04
Konishi, K.	SC–2
Konishi, T.	PB–06
Kon, Y.	KA–1
Kowada, H.	PM–01
Kubota, Y.	SB–2
Kudo, M.	PM–10
Kurogane, T.	PB–11
Maeda, G.	PM–20
Maeda, M.	PB–04
Maeda, S.	PB–01
Mamizu, N.	PB–10
Marsh, M.	SC–1
Masum, M.A.	KA–1
Matsue, H.	PB–10
Matsumoto, K.	PM–07
Matsumura, S.	PM–11
Matsushima, H.	PB–13
Matsuura, K.	PM–06
Matsuyama, K.	PM–15
Mimura, M.	SC–2
Minami, H.	PB–04
Mineyuki, Y.	PB–11, PB–12
Mitarai, S.	PB–01
Mitsuoka, K.	PB–09
Miyamoto, T.	PM–08
Miyata, M.	SS1–3
Miyata, T.	SS1–3
Miyazaki, N.	PB–01
Mori, S.	PM–01
Morishita, K.	PM–12
Murakami, Y.	SPL–1
Murakami, Y.O.	PM–03
Muraoka, M.	PM–14
Murata, K.	PB–01
Muto, H.	PM–15
Muto, S.	SM–1
Nagashima, K.	PM–09
Nakai, T.	PB–12
Nakajima, E.	PB–02
Nakamura, Akari	PB–08
Nakamura, Akinori	PM–15
Nakamura, Y.	PB–10
Namba, K.	SS1–3
Ngo-Huynh, K.-L.	PM–10
Nishida, T.	PB–02
Nishioka, H.	SC–2
Nomura, N.	SS1–1
Nomura, Y.	PM–21, SM–4
Nonaka, T.	SC–2
Numabe, Y.	PB–14
Obukuro, Y.	PM–09
Ogawa, R.	PB–15
Ogawa, S.	PM–06
Ogawa, T.	SM–6
Ohmukai, R.	PB–03
Ohno, N.	PB–07
Oho, E.	PM–16, PM–17, PM–18
Ohsawa, D.	PB–06
Ohta, K.	PM–15, SC–2
Ohyama, J.	SM–1
Oikawa, M.	PB–06
Okamoto, M.	PB–08
Okuyama, T.	PM–09, PM–10, PM–15
Otoyama, M.	PM–01
Otsuka, Y.	PM–13, PM–14
Saitoh, K.	PM–21
Sakai, N.	PB–13
Sakamoto, T.	PB–16
Sasajima, Y.	SS1–3
Sase, I.	SC–2
Sato, K.	PM–04
Sato, M.	PB–04, PB–08
Sato, Y.	PM–05, PM–06
Satsuma, A.	SM–1
Seino, S.	PB–02
Seki, T.	PM–03

Senga, H. PM–12
Seto, N. PB–04
Shibata, N. PM–03
Shiga, M. PM–02
Shimazu, T. PB–11
Shinohara, Y. PB–07
Shiroguchi, K. SB–3
Shoji, T. PM–03
Suga, M. SC–2
Sugiura-Nakazato, M. PB–05
Suzuki, K. PM–16, PM–17, PM–18
Tachibana, T. PB–14
Takabe, K. SS1–1
Takagi, K. SS2–4
Takahashi, K. PM–13
Takaki, T. PB–13
Takakuwa, Y. PM–06
Takami, M. PB–13
Takase, H. PB–05, PB–16
Takebe, A. PB–13
Tamaoki, D. PB–11, PB–12
Tanaka, H. PM–02
Tanaka, N. SM–1
Tanaka, T. PB–08
Tanigaki, F. PB–11
Tatsumisago, M. PM–01
Terauchi, M. PM–05, PM–06
Toh, S. PM–08
Tominaga, T. PM–12
Toyota, M. SB–1
Tsubouchi, T. PM–02
Tsukasaki, H. PM–01
Uchimoto, Y. PM–01
Uchiyama, T. PM–01
Ueda, K. PM–19
Ueda, M. SPL–2
Uehara, F. PM–14
Ueki, T. PB–07
Uematsu, K. SS1–4
Uesugi, K. PB–11, PB–12
Ushiki, T. K–3, SS2–1
Wakabayashi, S. PB–10
Wang, Z.-L. SM–6
Watanabe, M. K–2
Watari, T. PM–02
Yamada, Hirofumi SS2–2
Yamada, Hiroyuki PB–01, PB–10,
Yamaguchi, M. PB–10
Yamamoto, Kazuo SM–4
Yamamoto, Kentaro PM–01
Yamamoto, R. PM–12
Yamamoto, T. PM–11
Yamamoto, Yorihiro PB–08
Yamamoto, Yuta SM–1
Yamashige, H. PM–02
Yamashita, H. SS1–2
Yamauchi, D. PB–11, PB–12
Yamazaki, N. SS2–4
Yamazaki, S. PM–16, PM–17, PM–18
Yanagisawa, K. K–4
Yanagida, T. PM–09
Yano, S. PB–11
Yasuda, H. PM–04
Yasunaga, T. PB–09
Yawata, Y. SS1–1
Yokoo, T. PM–09
Yoneyama, S. SC–1
Yoshimoto, S. PM–13